2019-01-01

Scratching The Surface Of The Isotope Landscape Of An Ore Deposit Molybdenum-Sulfur Isotope Relationships In A Porphyry Copper-Molybdenum Deposit (Santa Rita / Chino Mine, NM)

Joshua Roger Peterson
University of Texas at El Paso

SCRATCHING THE SURFACE OF THE ISOTOPE LANDSCAPE OF AN ORE DEPOSIT

MOLYBDENUM-SULFUR ISOTOPE RELATIONSHIPS IN A PORPHYRY COPPER-MOLYBDENUM DEPOSIT

(SANTA RITA / CHINO MINE, NM)

JOSHUA ROGER PETERSON

Master's Program in Geological Sciences

APPROVED:

Gail Lee Arnold, Ph.D., Chair

Benjamin Brunner, Ph.D., Co-Chair

Philip Goodell, Ph.D.

Joshua Villalobos, M.S.

Stephen L. Crites, Jr., Ph.D.
Dean of the Graduate School

Dedication

This thesis is dedicated to my wife Deena, who saw potential in me when many didn't, and my daughter Charlotte, who I know will go on to do greater things.

SCRATCHING THE SURFACE OF THE ISOTOPE LANDSCAPE OF AN ORE DEPOSIT

MOLYBDENUM-SULFUR ISOTOPE RELATIONSHIPS IN A PORPHYRY COPPER-MOLYBDENUM DEPOSIT

(SANTA RITA / CHINO MINE, NM)

by

JOSHUA ROGER PETERSON, B.S

THESIS

Presented to the Faculty of the Graduate School of

The University of Texas at El Paso

in Partial Fulfillment

of the Requirements

for the Degree of

MASTER OF SCIENCE

Department of Geological Sciences

THE UNIVERSITY OF TEXAS AT EL PASO

December 2019

Acknowledgements

I would like to thank my wife for supporting me through my education. All my mentors through Community College and UTEP, Josh Villalobos, for continuing mentorship and encouragement. Dr. Phil Goodell, and his mineral pop-quizzes, Na-Al-Si_3-O_8, the chemical formula of albite.

My very first class at UTEP was Light-Stable Isotopes, with the geology department's new faculty member Dr. Ben Brunner, I had no clue that would lead me here. I would like to thank Dr. Arnold, for her patience and mentorship, I don't know if I would have entered, let alone completed, this program without her.

I would also like to thank Ralph Stegen from Freeport-MacMoRan who granted us access to his mines and the opportunity to collect samples. My thanks also go to Dr. Frank Ramos at NMSU for allowing us to use his MC-ICPMS facilities to make our molybdenum isotope measurements, when no-one nearby would.

Lastly, I would like to thank my Mother-in-law Letty, for taking care of my daughter without question and affording me the time to complete my studies.

Abstract

More than 95% of the world's molybdenum (Mo) is mined from porphyry deposits (Sinclair, 2007). Molybdenum is an important component for the metal industry, as a key ingredient in stainless steel alloys and high-speed heat resistant tools. Despite the importance of porphyry deposits for the supply of this industrially important metal, major questions about Mo mineral precipitation remain unresolved and the process of ore body emplacement and formation remains poorly investigated (Cooke et al., 2014a).

Recent observations have revealed a wide range of Mo isotope compositions in porphyry deposits, both globally and locally (Greber et al., 2014a; Shafiei et al., 2014; Li et al., 2019), demonstrating that Mo isotope signatures may represent an excellent record of processes during formation of molybdenite (MoS_2) ores. It has been hypothesized that Rayleigh isotope fractionation accounts for the large variation in MoS_2 ore isotope compositions (Hannah et al., 2007). Also agreed upon is that sulfide (H_2S, HS^-, S^{2-}) is key in the formation of MoS_2 deposits and that sulfide availability is a driver for ore mineral precipitation. A Rayleigh isotope fractionation process not only places a major control on the Mo isotope variability, it should also exert a similar control on sulfur (S) isotopes. To date, it has not been tested if there is a systematic relationship between Mo and S isotope compositions, despite the fact that the combined Mo and S isotope compositions of MoS_2 offers a window into the reconstructing ore formation processes.

I present Mo and S isotope data obtained from drill-core samples from the Santa Rita / Chino Mine. The coupled Mo-S isotope systematics of MoS_2 mineralization in this deposit demonstrate that Rayleigh isotope fractionation processes may not always be the sole ‘answer’, and that different mineralization events and processes can be identified and characterized through a combination of petrography, chemical inventory and coupled isotope studies.

Table of Contents

List of Figures

Chapter 1: Background & Motivation

Copper-molybdenum porphyry deposits account for the majority of the world's economically accessible metals, producing more than 50% of copper (Cu) and 95% of molybdenum (Mo). While molybdenum only ore deposits like Climax and Urad-Henderson are remarkably unique deposit types, and gross large amounts molybdenum these types of deposits are also notably few in number. Mixed Cu-Mo deposits far outnumber unique deposits (Fig. 1).

Many studies have been conducted classifying porphyry deposit alteration types and mineralization zones, recognizing geometries that have been reproduced time and time again. The generally distinguishing characteristics of porphyry deposits are low grade accumulations of copper, gold, and/or molybdenum in halos surrounding a porphyritic core. The ore body and alterations surrounding the porphyritic core can be classified by the composition of the intruding stocks, ranging from calcic, calc-alkalic, high K-calc-alkalic, alkalic-calc, and alkalic. Most deposits show a potassic core, surrounded by a quartz-sericite-pyrite (Qtz-Ser-Pyr) zone, an argillic (clay rich) zone, and a propylitic (epidote, chlorite) zone (Wester, 1981). Most high-grade molybdenite (MoS_2) is found in and around the Qtz-Ser-Pyr zone but can also be found from the outer edge of the stock to the argillic zone. Vein and breccia structures can carry mineralization further and in higher concentrations, but the focus exploration and production of Mo ore remains focused on the Mo hosted in the Qtz-Ser-Pyr plays.

The Mo isotope composition of MoS_2 from ore deposits around the world has been primarily analyzed to assess the homogeneity and value of the molybdenum isotope composition of the crust (Barling et al., 2001; Siebert et al., 2003; Arnold et al., 2004; Hannah et al., 2007; Malinovsky et al., 2007; Poulson Brucker et al., 2009; Mathur et al., 2010; Naegler et al., 2011; Greber et al., 2011, 2014b; Shafiei et al., 2014), a key value to determine paleoredox conditions

throughout Earth's history (Barling et al., 2001; Arnold et al., 2004). Breillat et al. (2016) recently compiled 391 MoS_2 Mo isotope measurements from around the world (Fig. 2). Of those 391 data points, approximately one-third (n=133) are from Cu-Mo porphyry deposits. The Mo isotope composition of MoS_2 has only recently been studied with focus on the interpretation of the genesis of the Mo ores themselves. Consequently, the number of analyzed samples from any specific deposit is low, and often the lithological, structural, and geochemical context of the analyzed sample with the ore deposit remains uncertain. Pivotal studies that propelled the use of Mo isotope systems to elucidate MoS_2 formation include the work of Hannah et al. (2007), Mathur et al. (2010), Greber et al. (2014), Shafiei et al. (2015), Breillat et al. (2016), and Li et al. (2019). My thesis research builds on the findings of these studies.

A central finding of these studies is that there is a considerable range in the Mo isotope composition of MoS_2 in general (Fig. 2), and for individual ore deposits (Greber et al., 2014b; Shafiei et al., 2015; Breillat et al., 2016). Molybdenite can precipitate from different hydrothermal phases including vapor phases and high or low salinity brines, at high (400-800 °C) to low (<200 °C) temperatures (West and Aiken, 1982; Ulrich and Mavrogenes, 2008; Zhang et al., 2012; Cooke et al., 2014b). Isotope fractionation can occur during the initial evolution of fluids from the source magma body, during the separation of vapor and fluid phases, and during the precipitation of the ores at any mineralization stage.

Observations by Greber et al. (2014) for the Questa Mo porphyry deposit showed that the Mo isotope composition of MoS_2 became progressively heavier over a sequence of mineralization stages (Fig. 3). The average early phase MoS_2 had a lighter isotope composition than MoS_2 deposited at a later stage. These observations were used to hypothesize that the MoS_2 evolution of the Questa deposit resulted from fluid exsolution that led to a source magma with an increasingly

heavier Mo isotope composition. The Mo isotope variability within each of the three mineralization stages was attributed to mineral precipitation or vapor-brine separation. Molybdenum isotope fractionation at all steps was attributed to Rayleigh fractionation.

More recently, contrasting data has been presented by Shafiei et al. (2015). In a study of the Kerman Cu-Mo porphyry deposits of Iran (Fig. 3), the isotope evolution of Mo in MoS_2 goes from heavy at the earliest stage of MoS_2 precipitation to light values during late stage deposition (Shafiei et al., 2015). In this study, it is suggested that during the early to transitional stages, the separation of ore-forming fluids exerts a major control on the Mo isotope fractionation, while later Mo isotope fractionation is the result of fluid boiling.

Most recently, Li and co-authors (2019) proposed environmental controls on fractionations, boiling, progressive cooling, and low mineralization. Still limited by a small sample set of 12 molybdenite vein samples, the interpretation invokes 3 mineralization 'pulses' to drive the molybdenite-molybdenum light, then heavy, then flat line with no further isotopic evolution. First, when the super critical fluid cools and separates into a liquid and vapor phase, heavier molybdenum preferentially partitions into the vapor phase. So successive boiling events will lead to a fluid with an increasingly lighter molybdenum isotope composition. In the second pulse, Rayleigh distillation with progressive crystallization of molybdenite from a fluid is invoked to drive the fluid and subsequent molybdenite heavier. Finally, they invoke a "low mineralization efficiency" phase to describe the lack of molybdenum isotope variation in the youngest / latest ore forming event. The sum take-away from that Li et al. (2019) propose is that after boiling, the liquid-phase is the dominant source of Mo, and this Mo reservoir would be isotopically light – hence, trends to molybdenite-molybdenum isotope compositions should point towards zones of higher Mo content.

These pioneering studies all suffer from similar limitations, that they have small data sets, and a focus on a single isotope system (Mo), still with little petrographic or broader geochemical assessment. In the case of Greber et al. (2014), there are only three to five samples per mineralization stage. In Shafiei et al. (2015) a maximum of three of the same vein type from any individual deposit. And in Li et al. (2019) a total of 12 unique samples are analyzed. Nonetheless, the total spread of MoS_2-Mo isotope variation of up to 1.9‰ ($\delta^{98}Mo$) is intriguing and demands further attention.

RAYLEIGH ISOTOPE DISTILLATION RELATED TO DEPOSITION OF MoS_2

One theme is unifying – regardless of the timing/temperature/phase/stage of the fractionation of Mo isotopes, there is a consensus that Rayleigh isotope distillation should govern the Mo isotope composition of MoS_2 (Hannah et al., 2007; Greber et al., 2014b; Shafiei et al., 2015; Li et al., 2019).

The reason for the general agreement that Rayleigh isotope fractionation is responsible for the observed Mo isotope composition range is that Mo isotope fractionation is expected to be small due to the small mass differences between isotopes relative to the overall mass of the element. Rayleigh isotope distillation provides a means by which these small isotope fractionations can still result in a large range of isotope compositions. If one consistently removes isotopically light material from a pool (e.g. isotopically light MoS_2), the residue becomes progressively heavier, which is then also reflected in an increase in the isotope composition of the removed material (Fig. 3). The opposite trend is observed if the removed material is isotopically heavier than the pool from which it originates. For example, using a moderate Mo isotope fractionation enrichment factor (ε) of 0.2‰, Rayleigh isotope distillation could potentially explain the observed Mo isotope range for individual mineralization stages in the Questa molybdenite deposit (Fig. 3). It can be

speculated that the overall trend to heavier values from igneous to hydrothermal magmatic-hydrothermal breccia to stockwork veins also correspond to a Rayleigh-type fractionation process (Fig. 3).

In the case of the Questa MoS_2 deposit, it was assumed that the precipitated MoS_2 is isotopically lighter than Mo in the brine (Hannah et al., 2007; Greber et al., 2014b) as demonstrated by the tendency towards heavier Mo isotope compositions in later stage MoS_2 (Greber et al., 2014b). This is in contrast to the data of Shafiei et al. (2015) which demonstrated that the latest stage, D-type veining, has the lightest Mo isotope composition of the deposit, which requires that MoS_2 that is formed at an early stage is isotopically heavier than MoS_2 that is formed at a later stage (Fig. 3).

In a Rayleigh isotope distillation process, more than sixty percent of the MoS_2 data fall in the range between the isotope composition of the original Mo pool and the isotope composition of the original Mo pool offset by the isotope enrichment factor, ε (in our example within a range of 0.2‰, Fig. 4). Less than forty percent of the data fall outside of this range, and it is these data that are responsible for the large spread in isotope compositions. This leads to the conclusion one should observe a non-normal distribution of the Mo isotope data if the data population size is large enough (Fig. 4). For any of the specific mineralization stages, the existing data sets do not show such a distribution (Fig. 3, black bars indicate average values, see also Breillat et al., 2016). This could be due to the small number of samples in each study or may challenge the concept that the observed isotopic scatter is due to Rayleigh isotope distillation. Another consequence of this process is that to obtain the observed range of isotope values for particular mineralization stages, essentially all Mo would need to be consumed, which means that each of these stages starts with an entirely 'new' Mo pool.

In conclusion, Rayleigh isotope distillation is a compelling explanation for the large Mo isotope variability observed in ore systems, but this concept has not been tested. This calls 1) for an assessment of alternative or complimentary explanations to the pure Rayleigh isotope distillation scenario, 2) for additional data that informs about the processes involved in the ore formation, and 3) for an effort to collect a large data set from a single deposit with well-defined mineralization stages, to test if Rayleigh isotope distillation is indeed the cause for the observed large Mo isotope variation in MoS_2. In this study, I addressed the first two aims, and started to build the data set required to address the third task.

RELATIONSHIP BETWEEN MO AND S ISOTOPES OF MoS_2

Sulfur is a key ingredient in porphyry deposits, acting as a complexation agent, and as an ore-former for chalcophile elements, and impacting the redox potential and pH of the system. Enormous amounts of S are contained within an ore deposit as sulfide, but also in adjacent hydrothermally altered rocks (e.g. as anhydrite, alunite). Elucidating the multitude of roles of sulfur in an ore deposit and assessing the sources of the S is key for the understanding of the genesis of the deposit. Sulfur isotopes of S phases and oxygen isotopes of sulfate are powerful tools to explore S transformations and the origin of S in hydrothermal systems. In particular, the S isotope offset between different coexisting S bearing minerals (e.g. pyrite vs. anhydrite) can be used to estimate formation temperatures, and the intersect of where the regression for the respective isotope compositions meet (i.e. there would be no isotope offset between the different minerals) has been used to estimate the S isotope composition of the S supplied to the hydrothermal system (e.g. (Field and Gustafson, 1976; Lang et al., 1989). The appearance of two elements in a mineral, such as Mo and S in MoS_2, does not necessarily mean that both elements underwent the same geochemical pathway that finally led to the formation of the mineral. This can be the case,

when a mineral precipitates from a solution saturated with respect to its constituents during cooling of the fluid, but there are also plenty situations where the opposite is the case, for example in the case of pyrite formation in a sediment, where ferrous iron that has been transported by diffusion to the location where pyrite forms, precipitates with sulfide that is formed *in situ* by microbial sulfate reduction. This example shows that combining the information from different isotope systems, such as iron and sulfur isotope systems in the formation of iron sulfide deposits, provides complimentary rather than redundant information (e.g.(Rouxel et al., 2008).

It is accepted that in the ore forming fluids, most S is in an oxidized state, allowing Cu and Mo to be mobile. The precipitation of MoS_2 then requires the presence or *in situ* production of Mo^{+IV} and sulfide (Fig. 5). Molybdenite can precipitate upon cooling from dissolved sulfide and Mo, or when new sulfide is formed, either through disproportionation of sulfur dioxide into sulfide and sulfate, a reaction that strongly increases the amount of sulfate (sulfuric acid) according to

$$4SO_2 + 4H_2O = H_2S + 3H_2SO_4,$$

or from sulfate reduction coupled to the oxidation of ferrous iron (e.g. (Sun et al., 2013), following

$$12Fe^{2+} + SO_4^{2-} + 12H_2O = 4Fe_3O_4 + HS^- + 23H^+.$$

The above reactions are associated with considerable S isotope fractionation. Moreover, in the temperature range from 450°C to 300°C – a temperature range representative for many porphyry deposits – S isotope exchange between reduced and oxidized S phases transitions from rapid to sluggish (Ohmoto and Lasaga, 1982). Depending on the relative speed of the sequestration of S phases into separate pools, such as brine-vapor phase segregation or precipitation as solids like MoS_2 or anhydrite, one might be confronted with a mixture of equilibrium and disequilibrium/kinetic isotope fractionations (Ohmoto and Lasaga, 1982). Also, the relative size of the various S pools, such as sulfide, sulfur dioxide, and sulfate pools plays a critical role. The

questions become if sulfur isotope variations in MoS_2 have been observed, and if different processes may lead to diagnostic Mo-S isotope relationships. The limited existing data for MoS_2 indicate that the absolute range of S isotope compositions is from 0‰ to 7‰, and that the isotope range within a single ore deposit is from less than 1‰ to 3.6‰ (Field and Gustafson, 1976; Stein and Hannah, 1985; Hellingwerf et al., 1987; Lang et al., 1989; Gallagher et al., 1992; Raith and Stein, 2000; Xu et al., 2016). This range is resolvable with routine sulfur isotope measurements (error less than 0.2‰). To explore if there is a potential for diagnostic Mo-S isotope relationships we calculated four different model scenarios (see Appendix A for details), that consider MoS_2 formation with different processes affecting the S isotope composition of sulfide (scenario 1 – isotope equilibrium between reduced and oxidized S species; scenario 2 – sulfur dioxide disproportion; scenario 3 – sulfate reduction, and scenario 4 – precipitation of MoS_2 from a limited sulfide pool) while maintaining the same Mo Rayleigh isotope distillation pattern (Fig. 6).

The different scenarios for S isotope fractionation related to the formation of MoS_2 show distinct S isotope trends. Alone, a single S isotope trend, such as to heavier or lighter compositions, is not diagnostic – particularly, because information about the S inventory at the time of the mineral formation may be absent.

If one combines the S isotope trends with the scenario chosen for the evolution of the Mo isotope composition of MoS_2, diagnostic patterns can be observed (Fig. 6). It follows that the combined analysis of S and Mo isotope signatures of MoS_2 will result in a better understanding of MoS_2 formation, an approach that "is an obvious next test" (Hannah et al., 2007).

WHY STUDY A CU-MO PORPHYRY DEPOSIT AND NOT A MO-ONLY PORPHYRY DEPOSIT?

Porphyry deposits, in general, account for 95% of the world's Mo production (Sinclair, 2007). Molybdenum-only porphyry deposits, although large producers of MoS_2 ore, represent an

end-member case for porphyry deposits, where the Cu was not only separated from the Mo, but fully lost from the system, along with a large part of the S budget (Cooke et al., 2014b). The high fluorine content of the initial magma chemistry required to generate large Climax-type Mo deposits like Questa makes these deposits rather chemically unique (Westra and Keith, 1981). We know there are Mo isotope variations in MoS_2 at both Questa (Mo-only) and the Kerman Cu-Mo porphyry deposit and that the Mo isotope trends for each deposit move in opposite directions (Fig. 3). From the literature, we cannot determine whether these differences are due to the nature of the deposit, or merely reflect differences in fractionation between fluid evolution or mineral precipitation as the two existing studies do not sample the same types of mineralization events.

The process of MoS_2 precipitation should be similar for both deposit types. However, we expect that the porphyry Cu-Mo deposits allow for a more complete Mo and S inventory (no S lost together with the Cu), which is of benefit for our studies and for future investigations, such as Mo content and isotope composition of Cu-S ores. I chose to focus my investigation on the Santa Rita / Chino Mine porphyry deposit in southern New Mexico because this site has 1) good outcrops, 2) an outstanding core repository & documentation, 3) well-defined and identified mineralization stages, and because 4) items 2 & 3 allow for the quantification of Mo reservoir sizes, 5) it is not an 'exotic' ore deposit type.

Chapter 2: Hypothesis & Objectives

The goal of my thesis research is to 1) assess if there are alternative or complimentary explanations to the pure Rayleigh isotope distillation scenario and to 2) obtain additional data that informs about the processes involved in molybdenite ore formation. I hypothesize that 1) Mo equilibrium isotope fractionation may present such an alternative, and 2) that a detailed spatial-temporal, combined Mo, S, and oxygen (O) isotope analysis of MoS_2 and anhydrite ($CaSO_4$) will provide critical information of the processes that lead to molybdenite precipitation. To achieve these goals and test my hypotheses, I formulate the following objectives for my thesis research. I will 1) explore how Mo isotope equilibrium fractionation impacts Mo isotope distribution in molybdenite by using numerical modeling to test if there is an alternative explanation to Rayleigh isotope distillation for the observed Mo isotope data range, and 2) create a comprehensive data set of Mo, S, and O isotope composition of minerals (molybdenite, pyrite, anhydrite) present in the Santa Rita / Chino Mine copper-molybdenum porphyry deposit to test if there are systematic relationships between the Mo and S isotope composition of MoS_2 from porphyry deposits that are diagnostic for the processes that are responsible for MoS_2 precipitation.

Chapter 3: Methodology

A prerequisite to achieving my objectives was to ensure that the MoS_2, Mo and S isotope data obtained can be interpreted in a meaningful way. My first approach was to assess whether MoS_2 would serve as an adequate 'archive' mineral phase, determining whether the Mo and S isotope composition of this mineral can faithfully record the geochemical history of the ore formation event, or if instead the isotopic signatures could have repeatedly overprinted during the evolution of the ore deposit. To achieve this a pilot study was conducted on a limited sample set from the Sierrita-Esperanza Deposit of Central-Southern New Mexico. This pilot-study was then followed by a more comprehensive data set obtained from the Santa Rita / Chino mine in Eastern New Mexico.

NUMERICAL MODELING

All of my modeling results were obtained by using Excel® spreadsheets. The calculations used (e.g. Rayleigh isotope distillation, equilibrium isotope fractionation, and calculation and extrapolation of temperature-dependent magnitudes of equilibrium isotope fractionation) are standard (i.e., textbook) approaches in stable isotope geochemistry. The novelty of my approach is the integration of equilibrium isotope fractionation with Rayleigh isotope distillation, and the combination of the model output the Mo and S isotope systems.

ANALYTICAL TECHNIQUES

Picking minerals for analysis

In each study, mineral samples were collocated along veins and fracture surfaces from roughly hand-sized samples. Individual grains were collected using forceps and dental tools at a macro scale. Minerals were separated and identified based on luster, morphology, and other

physical properties. If necessary, grains were washed with 30% hydrogen peroxide or dilute (5%) hydrochloric acid to remove surface oxidation.

Molybdenum isotope analysis of molybdenite

To prepare the samples for analysis, 0.1 to 0.2 mg of MoS_2 were dissolved in 1 ml of concentrated nitric acid following the protocol of (Anbar et al., 2001). Because of the extremely high proportion of Mo in MoS2 (~60%), no further sample purification was necessary. After dissolution, the samples were diluted to a final concentration of 200 pbb Mo in 0.32 M nitric acid for Mo isotope analysis. Because of the extremely high proportion of Mo in MoS_2 (~60%), no further sample purification was necessary.

Molybdenum isotope analysis was performed in the laboratory of Dr. Frank Ramos at New Mexico State University using a Thermo Scientific Neptune multi-collector inductively coupled plasma-source mass spectrometer. Samples were introduced via a standard peri-pump set-up with desolvation. A 200 ppb Mo solution yields a signal of approximately 0.5 V on ^{95}Mo under standard conditions. All samples were measured relative to the international reference solution SRM NIST3134 (Greber et al., 2012; Goldberg et al., 2013)where $\delta^{98}Mo_{NIST}$ equals 0‰. A standard-sample bracketing technique was used with no external or double spike to correct for mass bias. Signals on molybdenum isotopes ^{92}Mo, ^{95}Mo, ^{97}Mo, ^{98}Mo, and ^{100}Mo were collected simultaneously and the $^{92}Mo/^{95}Mo$, $^{97}Mo/^{95}Mo$, $^{98}Mo/^{95}Mo$, and $^{100}Mo/^{95}Mo$ ratios reported. The per amu fractionation was calculated for all isotope ratios free of isobaric interference and quality control defined as being in agreement with each other generally better than ±0.01‰ per amu. Instrument drift was monitored closely through all runs, and reproducibility $\delta^{98}Mo$ analysis based on repeated measurements of the NIST 3134 standard was calculated to be ±0.2‰. The

molybdenum isotope composition data are reported using conventional δ notation relative to the NIST 3134 standard, where

$$\delta^{98}Mo = [(^{98}Mo_{sample}/^{95}Mo_{sample}) / (^{98}Mo_{NIST3134}/^{95}Mo_{NIST3134})] -1 * 1{,}000\ ‰$$

External reproducibility was monitored using a common Mo isotope standard NIST RM8599, the Henderson molybdenite standard, which was prepared and processed identically to the unknown samples. The results for this standard is an average value of $\delta^{98}Mo_{NIST}$ = -0.11‰, in good agreement with other published values (Goldberg et al., 2013).

Sulfur isotope analysis of molybdenite and pyrite

For sulfur isotope analysis, ~0.16 mg of molybdenite (MoS_2), ~0.25 mg of pyrite (FeS_2) and ~0.60 mg associated silver sulfide standards (IAEA-S-1, $\delta^{34}S$ = -0.30‰; IAEA-S-2, $\delta^{34}S$ = +22.7‰; and IAEA-S-3, $\delta^{34}S$ = -32.3‰.) were weighed into tin capsules with an approximately equal amount of vanadium pentoxide (V_2O_5). The samples were analyzed using an Elementar® Pyrocube, connected to a GEOVisION® isotope ratio mass spectrometer in the EASI laboratory of Dr. Benjamin Brunner in the Department of Geological Sciences at The University of Texas at El Paso. The standard deviation (1σ) for replicate measurements of standards was 0.3‰ for sulfur isotope values. Sulfur isotope values are reported in per mil relative to VCDT, following the equation:

$$\delta^{34}S = [(^{34}S_{sample}/^{32}S_{sample}) / (^{34}S_{standard}/^{32}S_{standard})] -1 * 1{,}000\ ‰$$

Sulfur & oxygen isotope analysis of anhydrite

For sulfur and oxygen isotope analysis, the anhydrite ($CaSO_4$) samples were converted into barium sulfate ($BaSO_4$). This conversion is performed for three reasons: First, calcium interferes with oxygen isotope analyses by reacting with sample-oxygen to calcium oxide (CaO) during the carbothermic conversion of the solid sample at 1450 ºC into carbon monoxide that can by analyzed

by isotope ratio mass spectrometry. Such an interference does not occur with barium. Secondly, the standards used for the oxygen isotope analyses are all barium sulfate standards. Thus, converting samples into the same compound is advantageous because it allows for a direct comparison and eliminates potential complications by using different materials. Third, the conversion also eliminates potential contaminants in the anhydrite samples, such as traces of sulfide, silicates or fluid inclusions, which could hamper sulfur or oxygen isotope analyses.

For sulfur isotope analysis of anhydrite, ~0.45 mg of $BaSO_4$ and associated standards (NBS-127, $\delta^{34}S$ = +21.1‰, IAEA-SO-5, $\delta^{34}S$ = +0.49‰, and IAEA-SO-6, $\delta^{34}S$ = −34.1‰) were weighed into tin capsules with an approximately equal amount of vanadium pentoxide (V2O5). For oxygen isotope analysis, ~0.45 mg of $BaSO_4$ and associated standards (NBS-127, $\delta^{18}O$ = +8.7‰, IAEA-SO-5, $\delta^{18}O$ = +12.0‰, and IAEA-SO-6, $\delta^{18}O$ = −11.3‰) were weighed into silver capsules. The samples were analyzed using an Elementar® Pyrocube, connected to a GEOVisION® isotope ratio mass spectrometer. The standard deviation (1σ) for replicate measurements of standards was 0.1‰ and 0.4‰ for sulfur and oxygen isotope values, respectively. Sulfur isotope values, and oxygen isotope values are reported in per mil relative to VCDT and VSMOW, respectively.

PROOF OF CONCEPT STUDY AT SIERRITA-ESPERANZA DEPOSIT

The Sierrita-Esperanza deposit comprises two originally separate, side-by-side pits within a single mineralized system that is tilted to the south by ~60° by normal faulting (Stavast et al., 2008). Brought into production in the late 1950s and 1960s, the combined Esperanza and Sierrita pits make up one of the largest Cu-Mo operations in the world (West and Aiken, 1982). The site has been in continuous production since initial operations began and the pits

merged between 1996 and 2002 and is now known simply as the Sierrita deposit, owned by owned by Freeport-McMoran Inc.

The geology and mineralization of the Sierrita deposit is described in detail in West and Aiken (1982) and is only briefly summarized here. Molybdenite veins can be found in all rock types present in the deposit, from the Triassic Ox Frame Rhyolite, over the Harris Ranch quartz monzonite, to and including the Ruby Star granodiorite, considered to be the source magma for the quartz monzonite porphyry and mineralization (West and Aiken, 1982). Multiple ore grades and mineralization zones have been identified at the mine site. There are two main zones of alteration, the Sierrita and the Amargosa, that are parallel to each other trending northwest to southwest. The other zones are the Cross, which connects between the Sierrita and the Amargosa zones within what was known as the Sierrita Pit and the northeast trending Esperanza zone.

Fluid inclusion studies on the older intrusive rocks at the Sierrita-Esperanza deposit indicate that the mineralization of this deposit resulted from two distinct hydrothermal events that differed in both temperature and salinity (Preece and Beane, 1982). The first event was associated with high salinity and high temperatures (410-440 °C). This event precipitated MoS_2 in association with albite and orthoclase veins in the Ruby Star Granite and with orthoclase veining in the Harris Ranch Quartz Monzonite. A lower temperature, lower salinity stage (middle-hydrothermal) at 370-320 °C accounted for most of the mineralization of the Harris Ranch Quartz Monzonite (Preece, 1979). Latest stage hydrothermal alteration also resulted in molybdenite 'paint' of indeterminate age partially filling small cracks and fractures (West and Aiken, 1982).

Five hand samples were collected during a pit tour of the Sierrita-Esperanza deposit. The samples collected can best be described as 'float', where exact sample locations within the original deposit cannot be determined or known. Each sample included molybdenite, pyrite, and

chalcopyrite, as sulfide minerals. Sample 1, called BDQ (Biotite Diorite Quartz), consisted of altered granite, and disseminated mineralization. Sample 2, called RS (Ruby Star), shows cross-cutting mineralization, molybdenite in altered veins cut by pyrite along a similarly altered vein. Sample 3, called R2, is a quartz-orthoclase vein type showing varied mineralization for molybdenum, pyrite, & chalcopyrite. Quartz and purple anhydrite are present. Sample 4, called R3, is a quartz-orthoclase vein type showing vein mineralization, molybdenite and pyrite along the orthoclase and biotite alteration zone, with some purple anhydrite. Sample 5, called R3.2, is a quartz-orthoclase flood type showing disseminated mineralization of completely altered rock. It contains molybdenite, pyrite, & chalcopyrite within a matrix of orthoclase and quartz.

The mineral assemblage present in the samples for this part of my study allows for an analysis of equilibrium fractionation of sulfur between sulfide species. Sulfur species, in particular sulfide (H_2S, HS^-, S^{2-}), are fundamental in the formation of porphyry deposits, and it can be speculated that sulfur partitioning coincides with molybdenum sequestration. The test here was to see if a) the sulfide mineral, molybdenite, is appropriately stable with regards to its isotopic composition or if it is reset/overprinted during later alteration events and b) if the isotope fractionation system operates in equilibrium with regards to S mineral speciation, or if the system appears to be in disequilibrium, might this support the concept of Rayleigh isotope distillation being the controlling process for the observed isotopic differences.

Results of pilot study

The sulfur isotopic offset between molybdenite and pyrite ($\Delta^{34}S = \delta^{34}S_{MoS2} - \delta^{34}S_{FeS2}$) for 4 out of 5 samples was on average ~ +1‰ (Fig. 7), which is larger than would be expected for equilibrium isotope fractionation, and more typical for chalcopyrite (Fig. 8). Sample R2 had highly variable pyrite-sulfur isotope compositions, likely due to chalcopyrite contamination in the

samples. This data can either be interpreted as misidentification of pyrite as chalcopyrite, as evidence of mineralization under isotope disequilibrium conditions (e.g. rapid cooling), or presence of two separate mineralization stages or pulses with differing chemistry and temperatures. Furthermore, the tight reproducibility of the molybdenite sulfur isotope data indicates that later overprinting of the isotope signature of molybdenite is negligible and that it is thus an appropriate target mineral for further research efforts.

MAIN STUDY SITE OVERVIEW

History of Santa Rita

The Santa Rita / Chino Deposit lies some distance South East of Silver City New Mexico and is comprised of Cretaceous laccoliths and dykes intruded into a thin, 1.2 km, of Paleozoic and Mesozoic sedimentary beds. The deposit has a long and colorful history of profit and loss, production and destruction. This deposit was first used by Native Americans, who while traveling through the valley would occasionally find samples of native copper (samples, chunks, specimens) on the ground/surface. The first recorded diggings and production in the valley were by Spanish Lieutenant Colonel Jose Manuel Carrasco. Carrasco understood the importance of the amount of copper available in the Santa Rita valley and he set up a small production and that was reportedly very profitable. Due to his position in the military Carrasco could not keep up with production at the mine and sold it to Francisco Manuel de Elguea who set up a small stone fort and with permission from the Spanish government also began to operate a prison camp at the site. The mine was then operated intermittently between Indian attacks and supply convoys. In 1825 some relief was found when Sylvester Pattie and his party of American trappers came upon the valley. Elguea offered free trapping in the surrounding wilderness if they would help protect against the attacking Apache. Pattie threatened the might of the U.S. Army if the attacks didn't stop. The Apache agreed

so long as the mine was only worked by Americans. The mine was sub-leased to Pattie but he then lost his entire savings to a clerk that embezzled the supply money. The misfortune left Pattie financially ruined and so he turned the mine back over to the owners. Shortly after the mine was operated by Stephen Coursier, a Frenchman who was able to monopolize the copper trade in the state of Chihuahua, Mexico. In 1837, a barbarous law was passed in Mexico to solve its Indian Problem, bounties for the scalps of the Mimbreno Apache, resulting in the Santa Rita del Cobre Massacre. Instead of instilling fear it bolstered anger and retaliation by cutting off supplies and communication. The mine was abandoned, and the miners ambushed in their retreat. In 1849 the United States Boundary Commission temporarily camped at the settlement and played an important role in the Conte-Bartlett Compromise. The site was occupied on and off until the beginning of the civil war. During the beginning of the civil war the mine was operated but abandoned when supplies were confiscated. Through the end of the Civil War there was a legal dispute over ownership of the mine and minerals. M.B. Hayes had previously purchased the land from the Elguea Estate, and ultimately claim to the mine and mineral rights to the ore below.

Around 1910 open pit mining commenced, by 1920 the last remaining tower of the fort was removed. In 1950-60, after mining production was proceeding in earnest, the small (but entire) population of the town of Santa Rita was relocated to accommodate expansion and combination of the Santa Rita and neighboring Chino mine. Today, the mine is owned and operated by Freeport-McMoRan.

Geological setting of the Santa Rita / Chino deposit

The geologic context begins with basement Cambrian granites, in an unconformable contact with the Bliss sandstone, a gap in the geologic record representative of more time than what is recorded in overlying layers. The Bliss grades into the limes of the El Paso group which

show grading from cherty beds to sandy shales. Shallow near-shore environment persisted in the region through the beginning of the Carboniferous. The Mississippian is marked by a period of continuous near shore deposition of the Lake Valley Limestone. The Pennsylvanian is marked by the Oswaldo Formation, thick shales overlaying a bed of chert. Following is a break in deposition in the silver city area. This marks the end of the Paleozoic seas in the region and the emergence of the Mesozoic continent. No dramatic structural features are noted in the older beds, but the contact between the Cretaceous beds spans Pennsylvanian beds through Cambrian, at sharp contacts, suggesting gentile uplift and tilting. The absence of Triassic and Jurassic beds indicates a long period of denudation or the presence of a continent during those periods. Subsidence led to the deposition of thousands of feet of sands muds and limes. Followed closely by volcanic intrusion of dykes and sills emanating from a center thought to be near Piños Altos to the north. Following begins the injection of quartz diorite as porphyritic laccoliths, dykes and sills. Followed by anticlinal warping and uplift, and the invasion of the granodiorite stocks of Santa Rita and Hanover and the formation of the ore bearing rock in the region. The compressional period is followed by extension and normal faulting, followed by a long period of erosion, stripping strata from the granodiorite, and enriching the zinc and copper ores. The Tertiary is marked by widespread volcanism, depositing rhyolitic sands and gravels, and capping the region in thick rhyolitic lava flows that covered hills and valleys. The extrusion of the lavas was followed by faulting and the eventual erosion of the underlying sands and gravels.

Core description and sample selection

Samples were collected at regular intervals from five cores offered by Freeport-McMoRan's Santa-Rita / Chino mine Core shack. Samples were targeted at 1-2 ft intervals where mineralization zones permitted, in barren zones samples were collected when seen.

Core D2414 is a quartz-monzonite stock with signs of hydrothermal alteration halos around veins along fractures. Quartz, altered feldspars, and hornblende. Veins show quartz, molybdenite, pyrite, chalcopyrite, and sericite. 27 samples collected from 515ft to 579 ft molybdenite rich samples taken about every 2.5 ft, more in rich zones.

Core D2406, a quartzite breccia, voids infilled with minerals, quartz, molybdenite, pyrite, chalcopyrite, sericite and a zone of purple anhydrite. 23 samples collected from 2114.5 ft to 2180.5 ft, molybdenite rich samples collected about every 3 ft, more in rich zones.

Core D2314, a breccia of grey-green clasts, showing disseminated pyrite and chalcopyrite. Voids infilled with quartz, molybdenite pyrite, chalcopyrite, sericite, and occasional anhydrite. 8 samples collected from 1346ft to 1379ft, molybdenite rich samples taken about every 4 ft, more in rich zones.

Core D2199 section represents a highly altered granodiorite stock, quartz and micas persisting, all feldspars mostly decomposed to clays or replaced by secondary minerals, some visible disseminated sulfide minerals. Fractures hosting veins of quartz sericite and molybdenite, with notable slicken textures, some small grains of pyrite and chalcopyrite. 12 samples collected from 910 ft to 926.5 ft, molybdenite rich samples taken about every 1.5 ft.

D1878B, (box may be backwards) Granodiorite with quartz rich veins and molybdenite along fracture surfaces. Quartz alteration halos seen. 4 samples collected from 1556.5 ft to 1578 ft, molybdenite rich samples taken about every 7 ft, more in rich zones.

Molybdenite samples from all five cores were analyzed for sulfur isotopes. Two cores, D2406 and D2314 were fully analyzed for molybdenum (molybdenite) and sulfur (molybdenite and anhydrite) isotope compositions.

Chapter 4: Discussion and Results

ROLE OF EQUILIBRIUM MOLYBDENUM ISOTOPE FRACTIONATION

Size of equilibrium molybdenum isotope fractionation

Information on the molybdenum isotope fractionation during molybdenite precipitation is not available. Molybdenite – a sulfide mineral where molybdenum is in a +IV oxidation state may be formed from thiomolybdate, a molybdenum anion that consists of molybdenum in +VI oxidation state that is coupled to four sulfide ions. Thiomolybdate is produced by the sequential replacement of oxygen ions of molybdate with sulfide ions. The equilibrium isotope effect between these two compounds has been calculated for low temperatures between the freezing point and 200 ºC (Tossell, 2005). Extrapolation to higher temperatures provides an estimate for the isotope fractionation between molybdate and thiomolybdate at hydrothermal temperatures (Fig. 9). The obtained depletion in ^{98}Mo of thiomolybdate relative to molybdate of approximately –1‰ may provide at least a rough approximation for the isotope fractionation that may be involved in the precipitation of molybdenite during ore formation processes, however, it is uncertain whether the reduction from Mo^{+VI} to Mo^{+IV} may also involve further isotope fractionation, and if the precipitation of molybdenite is a unidirectional (kinetic isotope fractionation) or equilibrium process.

An alternative approach is to estimate the molybdenum isotope fractionation in the conversion of Mo^{+VI} to Mo^{+IV} based on a comparison to a similar process. Sulfur isotope fractionation may be considered an analogue because of the chemical similarities between S and Mo (same group in periodic table). There is considerable fractionation between different redox states of S, for example sulfate (S^{+VI}) is enriched in ^{34}S by ~+10.9‰ and ~+3.2‰ relative to sulfite (S^{+VI}) at 25 ºC and 450 ºC, respectively (Sakai, 1968). Accounting for relative smaller mass

difference for molybdenum isotope fractionation (i.e. (^{98}Mo-^{95}Mo)/^{95}Mo=0.031 relative to (^{34}S-^{32}S)/^{32}S=0.063), one would expect that such a reduction for Mo would correspond to approximately 3.7‰ and 1.1‰ at 25 ºC and 450 ºC, respectively. Based on these considerations, and acknowledging the many caveats associated with such comparisons, it is not unreasonable to assume that Mo isotope fractionation may be approximately +1‰ at temperatures around 450 ºC, which is five times larger than the +0.2‰ estimate used in the previous examples (Fig. 4). Using this estimate in an equilibrium isotope fractionation scenario, it becomes evident that by simple change in speciation (e.g. molybdate vs. thiomolybdate), a considerable range of Mo isotope values can be obtained for MoS_2 (Fig. 10). This change would not necessitate a large change in the inventory of total molybdenum and would also not result in a specific isotopic clustering of values, as one would expect for Rayleigh isotope distillation. As such, equilibrium Mo isotope fractionation must also be considered a potential cause for the observed large ranges of Mo isotope values for ore deposits. However, it must be acknowledged that 1) the maximum equilibrium isotope fractionation is only expressed if the species that serves as reactant for MoS_2 precipitation (assumed to be similar to thiomolybdate) is of very low abundance relative to its counterpart (assumed to be similar to molybdate), and 2) that equilibrium isotope fractionation cannot 'magnify' itself to obtain a greater range. To achieve the latter, an underlying equilibrium isotope fractionation must be combined with a Rayleigh isotope distillation-type process.

Rayleigh isotope distillation and equilibrium isotope fractionation in concert

Such a combination of equilibrium isotope fractionation and Rayleigh isotope distillation can be expected for the formation of MoS_2 in ore deposits, as equilibrium isotope fractionation between different Mo species in vapor and liquid phases is likely to be rapid at elevated temperatures, whereas the precipitation of the MoS_2 mineral may be a rapid, unidirectional process, which effectively removes a Mo compound that is isotopically depleted or enriched in ^{98}Mo relative to the total Mo pool. Depending on the type of removal process, and distribution of species, this will strongly impact the observed Mo isotope patterns in MoS_2. I illustrate this by presenting three different scenarios.

Scenario 1: Depending on speciation (dominance of compound that is reactant for molybdenite formation vs. dominance of compound that is not reactant), on will observe dramatically different Mo isotope fractionation relative to the total Mo pool (Fig. 11). As a consequence, one also would observe dramatically different Rayleigh isotope distillation patterns (Fig. 12).

Scenario 1 considered two different, but fixed ratios between compound that serves as reactant for molybdenite formation and compound that is not. Scenario 2 and 3 explore situations in which speciation shifts:

Scenario 2 considers a case where the Mo pool that does not serve as a direct source of Mo for MoS_2 formation (e.g. molybdate) stays constant, whereas the pool that is the source (e.g. thiomolybdate) is depleted over time. Overall, this results in a change of the isotope composition of the total Mo pool (e.g. becomes isotopically enriched in ^{98}Mo because isotopically depleted ^{98}Mo is removed as molybdenite). However, due to the change in speciation, the isotope offset between the source (e.g. thiomolybdate) and the total Mo becomes larger, resulting in no change

of the isotope composition of the produced molybdenite. This example demonstrates that the combined effects of equilibrium isotope fractionation and shift in Mo speciation can eradicate any evidence for a unidirectional removal of a fractionated molybdenite product, which would commonly be expected to yield a typical Rayleigh isotope distillation pattern (Fig. 13).

Scenario 3 illustrates an even more extreme case, in which the pool of one species grows at the expense of the pool that serves as source for the formation of MoS_2. Such a scenario is not uncommon in geochemical processes. For example, the disproportionation of sulfur dioxide produces sulfate and sulfide, and sulfide can be sequestered as pyrite. In such a case, the pool of sulfate grows in size, while the pool of sulfur dioxide diminishes. As similar scenario could be envisioned for Mo compounds. Such a scenario may result in an inverse isotope fractionation, i.e. the produced MoS_2 would become isotopically lighter (Fig. 14).

Lessons learned/insights about equilibrium Mo isotope fractionation

- 1‰ isotope fractionation could already account for much of the observed variability: this means that not only Rayleigh isotope distillation, but also simple speciation shifts could be important
- Flat-line isotope trends may be caused by:
    - Unidirectional process (what comes in must go out)
    - Large Mo reservoir that is not much affected by fractionation
    - Shifts in speciation can counter-act expected Rayleigh trends, or even reverse them
- Looking at Mo isotope trends (and only MoS_2) alone is likely not sufficient to determine what process took place, and may not even be diagnostic for a Rayleigh-type isotope distillation process

SANTA RITA / CHINO DEPOSIT DATA SUMMARY

Core D2406

We start with a review of the Core D2406, which is has a n=13 sample set for coupled Mo-S of molybdenite (MoS_2) and an additional subset of 9 samples with coupled S-O isotope composition of anhydrite ($CaSO_4$). These samples span 66 ft of core section and 3 different zones of metal content (Fig. 15). MoS_2-molybdenum isotope compositions are variable within a range of δ^{98}Mo from 0.13‰ to 1.15‰. All measured values are heavy relative to the NIST 3134 standard and presumed source value of 0‰. Molybdenite-sulfur isotope compositions range from δ^{34}S = -3.5‰ to +8.4‰. This nearly 12‰ spread in molybdenite-sulfur isotope compositions is significantly larger than previously reported data. Even if one disregards the δ^{34}S = +8.4‰ value as an outlier, the sulfur isotope data range still spans 9‰, 3times larger than what is in the literature (Field and Gustafson, 1976; Hellingwerf et al., 1987; Lang et al., 1989; Gallagher et al., 1992; Raith and Stein, 2000; Xu et al., 2016). Anhydrite is only present in the deeper section of the D2406 core sample set. The anhydrite sulfur isotope compositions span a narrower range, of δ^{34}S from +10.3‰ to 15.3‰. The anhydrite oxygen isotope composition ranges from δ^{18}O of +5.5‰ to +7.5‰. Viewed independently, there is appears to be no correlation of Mo, S, or O isotope composition with depth or metal content.

Core D2314

For the samples from this core only molybdenite Mo and S isotope compositions were obtained as there was no macroscopically visible anhydrite in this core section. Molybdenite isotope compositions are contained within a narrow range (< 1‰), with values from -0.4‰ to -1.2‰ and -0.7 to -1.6 for δ^{98}Mo and δ^{34}S, respectively. Notably, in contrast to the D2406 core, the MoS_2-Mo isotope compositions in this core are lighter than the NIST 3134 standard.

Chapter 5. Interpretation

Sulfur isotopes of S phases and oxygen isotopes of sulfate are powerful tools to explore S transformations and the origin of S in hydrothermal systems. For a segment of core D2406 (~2150 to 2180 ft depth), macroscopically visible molybdenite and anhydrite was extractable, which allows for an in-depth interpretation of the data.

MOLYBDENITE-ANHYDRITE SULFUR AND OXYGEN ISOTOPE RELATIONSHIPS

Equilibrium sulfur isotope fractionation between molybdenite and anhydrite

In cases where sulfur isotope equilibrium is established between various S-compounds in a system, the S isotope mass balance can be calculated as

$$S_{total} \cdot \delta^{34}S_{total} = \Sigma(S_i \cdot \delta^{34}S_i) = \Sigma(S_i \cdot (\delta^{34}S_{anhydrite} - \varepsilon^{34}S_{anhydrite\text{-}i}[T])),$$

where the product of the initial amount of sulfur (i.e. sulfur source, S_{total}) with its isotope composition ($\delta^{34}S_{total}$) is equal to the sum of the products of the different S compounds (S_i, e.g. anhydrite, pyrite, chalcopyrite) with their respective isotope composition ($\delta^{34}S_i$). At isotopic equilibrium, the isotope composition of these different compounds can be determined as the difference between the isotope composition of a selected reference compound (here chosen to be anhydrite, $\delta^{34}S_{anhydrite}$) and the temperature dependent equilibrium isotope fractionation between the reference compound and the compound of interest ($\varepsilon^{34}S_{anhydrite\text{-}i}[T]$, Fig. 8). For a system dominated by two components with known isotope composition, here chosen to be anhydrite and molybdenite, it follows that

$$\delta^{34}S_{total} = S_{anhydrite} / S_{total} \cdot \delta^{34}S_{anhydrite}[T] + S_{molybdenite} / S_{total} \cdot (\delta^{34}S_{anhydrite}[T] - \delta^{34}S_{molybdenite}[T]),$$

with

$$\delta^{34}S_{anhydrite}[T] = \delta^{34}S_{total} + S_{anhydrite} / S_{total} \cdot (\delta^{34}S_{anhydrite}[T] - \delta^{34}S_{molybdenite}[T]),$$

and

$$\delta^{34}S_{molybdenite}[T] = \delta^{34}S_{total} - S_{molybdenite} / S_{total} \cdot (\delta^{34}S_{anhydrite}[T] - \delta^{34}S_{molybdenite}[T]),$$

with

$$1 = S_{anhydrite} / S_{total} + S_{molybdenite} / S_{total}.$$

Isotope data can be plotted using these two equations, and application of linear regression reveals the initial S isotope composition of the system, as well as the relative abundance of the involved species (e.g. Field and Gustafson, 1976; Lang et al., 1989). While this treatment of data is extremely powerful, it comes with a major and a minor caveat. The most critical issue is that such a plot can yield correlative linear regression lines also for random data (i.e. non-equilibrium conditions) sets because the values on the y and x axes are dependent on each other (Fig. 16). Thus, correlation cannot be taken as an argument for equilibrium isotope fractionation. A second, typically less critical issue is that even under equilibrium conditions, the presence of other compounds (e.g. pyrite and chalcopyrite) can impact the observed species distribution, and to a lesser degree, the determined S isotope composition of the initial S pool. Compared to randomly generated data that cover the same isotope data range as our measured data, the plot with actual data gives a better R^2 value (0.79 for anhydrite, 0.94 for molybdenite as opposed to 0.41 and 0.80 for the generic data) for the regressions for anhydrite and sulfide data (Fig. 17). This may be taken as indication that the assumption of S isotope equilibrium between anhydrite and molybdenite is valid, and I will carry out the further discussion of this data set under this premise.

Implications of coupled molybdenite and anhydrite sulfur-oxygen isotope data set

1) The S isotope source has a value of 8.3‰. This value is interpreted from the y-intercept of the anhydrite molybdenite regression lines (Fig. 17). Sulfur from magmatic sources falls in a range of $\delta^{34}S$ of -11‰ to +9‰ (Faure, 1986; Hoefs, 2008; Metrich and Mandeville, 2010). Sulfur

that is enriched in ^{34}S relative to this range can be cause by the contribution of S that is recycled from buried with sediments, for example evaporites, but also due to equilibrium isotope fractionation during the formation of a vapor phase from a hypercritical fluid, e.g. the formation of sulfur dioxide (SO_2) from a slightly more reduced S source, which results in SO_2 enriched in ^{34}S in a vapor phase and a brine that contains sulfide depleted in ^{34}S.

2) During equilibrium S isotope fractionation, the sulfate pool is proportionally less shifted to heavier values then the extent at which the sulfide pool is shifted to lighter values, which means that the sulfate pool is consistently larger (~67%) than the sulfide (~33%) pool. The ratio of ratio of SO_2 to H_2S in hydrous magmatic gases (predominantly steam 30–90 mol% H_2O) with varies with redox state, pressure, temperature, and sulfur fugacity (Moretti and Papale, 2004; Burgisser and Scaillet, 2007; Burgisser et al., 2015). The gas released from typical basaltic arc magmas has molar H_2S:SO_2 ratios below 1.5 (Burgisser et al., 2015), with the ratio decreasing with decreasing pressure. Sulfur dioxide disproportion ($4SO_2 + 8H_2O = 3H_2SO_4 + 1H_2S$) results in a 75:25 stoichiometry for these pools, which is not far from the observed relationship. I therefore interpret the data as result of SO_2 disproportionation, whereby the resulting stoichiometry is modified by a) anhydrite precipitation that exceeds sulfide precipitation and b) redox buffering by the host rock, which contributes to the size of the sulfide pool via SO_2 reduction coupled to ferrous iron oxidation.

3) Molybdenite formed under a large range of temperatures, from 640 ºC to 360 ºC. Molybdenite formation in the temperature range of 440 ºC to 360 ºC is commonly observed (Kessel et al., 2005; Landtwing et al., 2005; Driesner and Heinrich, 2007; Klemm et al., 2008; Kouzmanov and Pokrovski, 2012; Cooke et al., 2014b), but formation at higher T has been documented (Zhang

et al., 2012) and temperatures exceeding 600 ºC have been postulated for the pilot study site (Ahmad and Rose, 1980).

4) The oxygen isotope composition of anhydrite does not show strong fluctuations. The reasons for this observation are as follows:

a) At the investigated temperatures equilibrium isotope fractionation between sulfate and water is small (~0‰ at 600 ºC; ~3.1‰ at 360 ºC; (McKenzie and Truesdell, 1977).

b) The oxygen isotope composition of sulfate is more easily altered at lower temperatures than S isotope of sulfate, because O atoms are 'outer part' of molecule, whereas S constitutes center. Consequently, the oxygen isotope composition of anhydrite may have been re-set (and homogenized) at lower temperatures.

c) Additional processes, in particular mixing of meteoric fluids which are isotopically light, and fluid-rock interactions can modify the oxygen isotope composition of water. The latter are responsible for the relatively heavy oxygen isotope signature of the sulfate. Oxygen isotope values of water in ore deposits fall in a range of +5‰ to +10‰ (Fekete et al., 2016) – which agrees well with the observations.

5) There are two data points for a molybdenite-anhydrite couple that are strongly offset from the bulk of the data. Most conspicuously, the S isotope composition of the molybdenite (+8.4‰) matches the composition of the S source (+8.3‰). I interpret this data as representative for the stage at which the SO_2 vapor started to form from a hypercritical fluid, i.e. at a temperature of 640 ºC. In an initial stage, this pool of SO_2 would have been small, and thus offset to heavy values relative to the bulk S that was still part of the fluid from which the molybdenite precipitate. However, already at a temperature of 620 ºC, the fixed ratio between sulfide and sulfate pool was

reached, which may indicate that at that time, the vapor phase was no longer in contact with the fluids it separated from.

6) The here postulated disproportionation of SO_2 into sulfate and sulfide comes with a caveat: at temperatures between 800 ºC and 400 ºC the reaction only becomes favorable if calcium ions (Ca^{2+}) are available that serve to precipitate anhydrite (Mavrogenes and Blundy, 2017). Thus, molybdenite and anhydrite precipitation at these temperatures are likely controlled by the availability of Ca^{2+} from the host lithologies. If no calcium ions are available, no anhydrite is formed, and molybdenite can only be generated via sulfide production from SO_2 reduction, e.g. by coupling to iron oxidation.

7) At temperatures below 400 ºC, SO_2 disproportionation becomes favorable also in the absence of calcium (Hemley and Jones, 1964; Holland, 1965; Gustafson and Hunt, 1975; Giggenbach, 1992; Reed, 1997), and S equilibrium isotope fractionation may no longer be achieved. At this point, rapid sulfide production and subsequent quantitative sequestration as MoS_2 could result in a small isotope fractionation causing MoS_2-S isotope compositions to approach to S isotope composition of the sulfate (sulfuric acid) pool. Because anhydrite may no longer be formed at such conditions, such cannot be observed in the sulfate-sulfide isotope plot.

GROUPING OF DATA BASED ON PETROGRAPHIC AND ISOTOPIC INFORMATION, AND INTERPRETATION OF MOLYBDENITE GENESIS

Based on the petrographic and Mo, S, and O isotope data I can discern four trends in my data set (Fig. 18).

Trend I corresponds to the 0.12% Mo mineralization in core D2406, and is characterized by a strong change in temperature of molybdenite formation, as well as a correlation of $\delta^{34}S_{molybdenite}$ with $\delta^{98}Mo_{molybdenite}$ and $\delta^{18}O_{anhydrite}$, with heaviest (most enriched in heavy isotope

values) isotope values observed at highest temperatures. I interpret the history of this mineralization stage as the result of initial boiling forming a first vapor phase which is enriched in ^{34}S and ^{98}Mo. Calcium ion availability likely maintained SO_2 disproportionation, and $\delta^{34}S$ with $\delta^{98}Mo$ are both controlled by equilibrium isotope fractionation that increases (pushed isotope composition of molybdenite to lighter values). The trend to lighter oxygen isotope compositions is somewhat surprising because lower temperatures should induce a larger equilibrium oxygen isotope fractionation, and thus enrichment of sulfate in ^{18}O relative to the water pool. The fact that this trend is reversed implies mixing of water which is enriched in ^{18}O due to fluid-rock interactions with meteoric water that is depleted in ^{18}O.

Trend II corresponds to the 0.08% mineralization in core D2406 and is also characterized by a strong change in temperature of molybdenite formation. However, there is no relationship or correlation between $\delta^{34}S_{molybdenite}$ with $\delta^{98}Mo_{molybdenite}$ because the Mo isotope composition data essentially remain constant around +0.4‰, and $\delta^{98}Mo_{molybdenite}$ is anticorrelated with $\delta^{18}O_{anhydrite}$. Heaviest S isotope composition values are observed at the highest temperature. I interpret the history of this mineralization stage as the result of a second boiling event that produced another phase enriched in ^{34}S and ^{98}Mo. Calcium ion availability likely limited SO_2 disproportionation (not all samples belonging to this trend have macroscopically visible anhydrite). Reduction of SO_2 could be important source of sulfide, however, as for Trend I, the sulfate-sulfide balance appears to remain redox buffered. The near-constant $\delta^{98}Mo_{molybdenite}$ are either due to a large Mo inventory, or, considering that Mo preferentially partitions into the fluid phase (Zajacz et al., 2017), more likely, caused rapid and quantitative Mo consumption that prevents the expression of isotope fractionation. The expected trend to isotopically heavier $\delta^{18}O_{anhydrite}$ with decreasing temperatures indicates that this pool did not mix with meteoric water.

Trend III, which is also observed in core D2406 is likely a succession of Trend I and/or Trend II. It is associated with the shallowest molybdenite ore, where no information on the content is available. It is marked by generally light S isotope compositions of molybdenite, absence of macroscopic anhydrite, and isotopically heavy, but scattering Mo isotope composition values. I hypothesize that this mineralization took place when SO_2 disproportionation is no longer limited by Ca^{2+} availability, i.e., at temperatures below 400 ºC. Spontaneous production of sulfide and sulfuric acid lead to quantitative Mo consumption, lack of anhydrite precipitation, a rapid shift in Mo and S speciation and the final tapping into the residual isotopically heavy Mo pool, resulting in considerable scattering of the data.

Trend IV, which corresponds to core D2314, originates from the fluid-vapor separation, likely leaving back an isotopically light, Mo-rich brine that also contains isotopically light S. Because sulfide strongly negatively impacts Mo solubility in fluids below 700 ºC and above 400 ºC (Zhang et al., 2012; apparently this effect somewhat opposite at temperatures of 350 ºC where a higher volatility of Mo in presence of H_2S has been observed - (Kokh et al., 2016), it is reasonable to assume that this remaining S predominantly exists as a slightly oxidized compound (e.g. as polysulfides, thiosulfate, etc.). Cooling of the fluid leads to the precipitation of molybdenite that is depleted in ^{98}Mo relative to the Mo from the vapor phase. This process may involve the conversion of intermediate S compounds or shifts in S species that operate in concert with changes in the Mo inventory. The observed isotope patterns are compatible with classical Mo Rayleigh isotope distillation scenario but could also be obtained by coupling to shifts in Mo speciation during molybdenite precipitation.

A TENTATIVE SYNTHESIS

The following interpretation of the processes that led to the formation of the different molybdenite mineralization is predominantly based on the observations made in this study. I emphasize that such an interpretation, without consideration of additional information, such as data from fluid inclusions, microscopic observations, rock porosity, or age dating of the ore is highly speculative. Thus, the value of this interpretation is in its use as a hypothesis generator, i.e. as a guide to predictions that can be tested rather than as a model that reliably describes the genesis of molybdenite at the studied sites.

The molybdenite mineralization has its origin in a hypercritical fluid located above a magma chamber (Fig. 19). This fluid contained significant amounts of sulfur and molybdenum. The overall oxidation state of the sulfur in this fluid was lower than +IV (SO_2) but higher than –II (H_2S). At temperatures higher than 640 ºC (likely higher than 850 ºC, see discussion of Trend II), a vapor or low-density fluid ($\delta^{34}S \sim +8.3‰$; $\delta^{98}Mo \sim +0.9‰$, eventually results in Trend I) started to separate from the hypercritical fluid. The evolution of the vapor/low-density fluid resulted in the formation of SO_2, leaving a now slightly more reduced sulfur pool in the remaining higher density fluid. At a temperature of ~ 640 ºC, two interactions with the host rock became important, 1) the reduction of SO_2 to H_2S coupled to the oxidation of reactive ferrous iron and 2) availability of calcium, allowing for the disproportionation of SO_2 into sulfuric acid and H_2S, followed by the precipitation of anhydrite and molybdenite. At temperatures above ~ 400 ºC the chemical equilibrium for the disproportionation of SO_2 into sulfuric acid and H_2S, falls heavily on the reactant side (i.e., $4SO_2 + 4H_2O >> H_2S + 3H_2SO_4$), however, small amounts of H_2S and H_2SO_4 coexist. The stoichiometry for the disproportionation reaction is such that 75% should be H_2SO_4 and 25% H_2S. Evidently, for Trend I (and subsequently also Trend II), this ratio is different (Figure

17). It is kept at a 67% H_2SO_4 and 33% H_2S ratio, a ratio that is maintained by a balance between anhydrite precipitation (lowers the amount of H_2SO_4), SO_2 reduction (increases amount of H_2S) and sulfide precipitation (decreases amount of H_2S), processes that controlled by host rock chemistry (calcium availability, reactivity towards sulfuric acid, available reducing power). Curiously, for one data point at 640 ºC this pattern does not hold (Figure 17). Here, the molybdenite sulfur isotope composition matches the isotope composition of the total sulfur pool ($\delta^{34}S \sim +8.3‰$), whereas the anhydrite sulfur isotope composition is offset to heavier values by the equilibrium sulfur isotope fractionation, which means that the reduced sulfur pool must have been much larger than the H_2SO_4 and SO_2 pools. An explanation for this observation is that at 640 ºC, a secondary, reduced dense brine separated from the vapor/low density fluid, from which molybdenite and anhydrite precipitated. During the ascent of the vapor/low-density fluid (Temperatures between 640 ºC and 440 ºC, Trend I), calcium supplied from the host rock allowed for sulfur dioxide disproportionation, producing anhydrite, and sulfide (Fig. 19). The latter precipitated as sulfide minerals, including molybdenite. Lower temperatures resulted in larger equilibrium isotope offsets between sulfide and sulfate (Figure 17), but also between molybdenum sequestered into molybdenite and the remaining, more oxidized molybdenum compounds, which explains the co-variation of $\delta^{34}S_{molybdenite}$ and $\delta^{98}Mo_{molybdenite}$ (Figure 18, Trend I). Enhanced equilibrium oxygen isotope fractionation between sulfate and fluid should also have resulted in isotopically heavier anhydrite, which is not the case (Figure 18). This indicates that the fluid became isotopically lighter at shallower depth, which was likely caused by mixing with meteoric water.

During the ascent of the vapor/low density fluids, once the temperatures dropped below 440 ºC, disproportionation of SO_2 into sulfuric acid and H_2S became spontaneous, replacing

Trend I with Trend III (Figure 18, 19). The disproportionation of SO_2 resulted in the near-quantitative sequestration the remaining, isotopically heavy molybdenum as molybdenite, which lead to $\delta^{98}Mo_{molybdenite}$ values scattering from +0.3‰ to +1.2‰. Full sulfur isotope equilibration between sulfuric acid and H_2S may not have persisted any longer, explaining the scatter in that data set ($\delta^{34}S_{molybdenite}$ from –1.9‰ to –3‰). As calcium availability was no longer the prerequisite for SO_2 disproportionation the sulfuric acid could continue to ascend to shallower depths.

At depth, subsequent to the separation of the vapor/low density fluid that resulted in Trends I and III, a second vapor/low density fluid ($\delta^{34}S$ ~ +8.3‰; $\delta^{98}Mo$ ~ +0.4‰, Trend II) separated from the high-density brine at temperatures exceeding 575 ºC. Likely, the temperature was much higher, as the isotopically heaviest $\delta^{34}S_{molybdenite}$ value ($\delta^{34}S$ ~ 5.36‰; Figure 18) is only offset by 1.7‰ from the isotope composition of the total sulfur pool, which is assumed to be dominated by SO_2, corresponding to an equilibrium temperature of approximately 850 ºC. The molybdenum isotope composition of this fluid was isotopically lighter because the separation of the first vapor/low density fluid removed isotopically heavy molybdenum form the original brine. During its ascent, this vapor/low density fluid (Trend II) followed the same pathway as the fluid in Trend I. As for Trend I, the host rock chemistry maintained a 67% H_2SO_4 and 33% H_2S ratio, balanced by anhydrite precipitation, SO_2 reduction and sulfide precipitation, which is evidenced by the sulfur isotope trends for anhydrite and molybdenite (Figure 17). However, there was no longer a covariation between $\delta^{34}S_{molybdenite}$ and $\delta^{98}Mo_{molybdenite}$ (Figure 18, Trend II). Potentially, the increase in the equilibrium isotope offset between molybdenum sequestered into molybdenite and remaining molybdenum at lower temperatures was compensated by the enrichment of residual molybdenum in ^{98}Mo due to the precipitation of molybdenite, leading to an invariant $\delta^{98}Mo_{molybdenite}$ (analogous, but not identical to scenario 2, Figure 13). This points to a limited pool

of molybdenum for Trend II, which agrees with the lower molybdenite mineralization compared to Trend I (0.08% vs. 0.12%). Although Trend II followed the fluid migration pathway of Trend I, there was no longer mixing with meteoric water (which may have been expelled by Trend I): the oxygen isotope composition of anhydrite increases with lower temperatures of formation, which agrees with an enhanced equilibrium isotope fractionation between sulfate and fluid (Figure 18).

Finally, the residual high-density brine, which due to the two vapor/low-density fluid separations became isotopically light ($\delta^{34}S$ = –0.7‰ to –1.7‰; $\delta^{98}Mo$ = –0.3‰ to –1.3‰, resulting in Trend IV) ascended to shallow depths (Fig. 19). The sulfur pool likely was a slightly oxidized compound (e.g. as polysulfides, thiosulfate; sulfide would result in immediate precipitation of molybdenite). Probably, rapid cooling of the fluid upon mixing with meteoric water led to the focused precipitation of molybdenite, explaining the high molybdenite ore content (1.9%). The observed isotope pattern (Trend IV, Figure 18) is compatible with a classical molybdenum Rayleigh isotope distillation scenario but, because the sulfur pool likely was a slightly oxidized – and thus, by proxy also more than one molybdenum compound, could also be obtained by coupling to shifts in the molybdenum speciation during molybdenite precipitation (analogous to Scenarios 1-3, Figures 12-14).

Chapter 6: Outlook/ Open Questions

As title for my thesis I chose "Scratching the surface of the isotope landscape of an ore deposit" and I believe I was successful in doing so. Among many isotopic treasures, I discovered many new questions and tasks that should be performed in the future but go well beyond the scope of this study. Here, I would like to take the opportunity to highlight issues and challenges that I find most pressing. On the most fundamental gaps in knowledge is a reasonable estimate for the Mo isotope fractionation in the formation of molybdenite at hydrothermally relevant temperatures. With modern technology, high-temperature laboratory experiments investigating molybdenite solubility have been performed (Zhang et al., 2012), however, such experiments have not yet been performed with the assessment of the involved isotope fractionation fractionations as a target. Another equally fundamental gap in knowledge – despite many recent studies (e.g. (Williams-Jones and Heinrich, 2005; Pokrovski et al., 2008; Seo et al., 2009; Zhang et al., 2012; Zajacz et al., 2013, 2017; Seward et al., 2014; Yao et al., 2016; Kokh et al., 2016; Louvel et al., 2017) – remains the behavior and speciation of metal and S compounds and their impact on isotope fractionation. Quantum-mechanic-based modeling of equilibrium isotope fractionation coupled to the analysis of Mo-Cu isotope systematics and Mo isotope analysis of anhydrite might provide new insights into these complex mechanisms. Moreover, while I provided with this study a first step in the attempt to collect enough data to perform a full assessment if Rayleigh isotope distillation is truly the driver for the wide range of Mo isotope compositions in ore deposits, more analyses on single deposits are required. Finally, and directly connected to this study, two major open questions remain: are my anhydrite-molybdenite temperature estimates reliable, and how can they be reconciled with fluid inclusion data, and is it possible that I misconstrued chalcopyrite as pyrite in my pilot study?

Chapter 7: Conclusions

This study demonstrates the urgent need for coupled isotope system data that can be combined with petrographic / chemical inventory evaluation to address burning questions in the research of ore deposits. Based on numerical modeling that integrates equilibrium isotope fractionation processes with Rayleigh isotope distillation it is evident that the assessment of Mo isotope data alone is not sufficient, because options other than pure Rayleigh distillation cannot be elucidated by a single isotope system study. In the study of the Sierrita and Santa Rita / Chino molybdenite ores, the coupling of the Mo isotope analysis to sulfur and oxygen isotope analysis of molybdenite and anhydrite did not just yield the "first comprehensive Mo-S isotope data set" and "largest documented S isotope range for molybdenite in a single ore deposit" but has proven to be extremely powerful in its application: Disproportionation of sulfur dioxide at temperatures as high as more than 600 ºC was identified as potential molybdenum-ore forming process, and the combination of oxygen and molybdenum isotope data sets allowed to identify different mineralization trends that otherwise would have gone undetected. These insights provide a next step in the improvement of the understanding of Cu-Mo porphyry ore deposits.

For treasure-hunters, I still owe the answer to one question: is there a direct application of the findings of this study to finding more Mo ores? I would propose two rules of thumb: 1) If you find molybdenite that has isotopically heavy Mo there is cause for optimism, because it is likely there nearby there is a highly mineralized fluid molybdenite trend (Trend IV), and 2) Look out for anhydrite-sulfide couples to determine temperatures: if high temperatures are found, molybdenite mineralization may be present.

Chapter 8: Figures

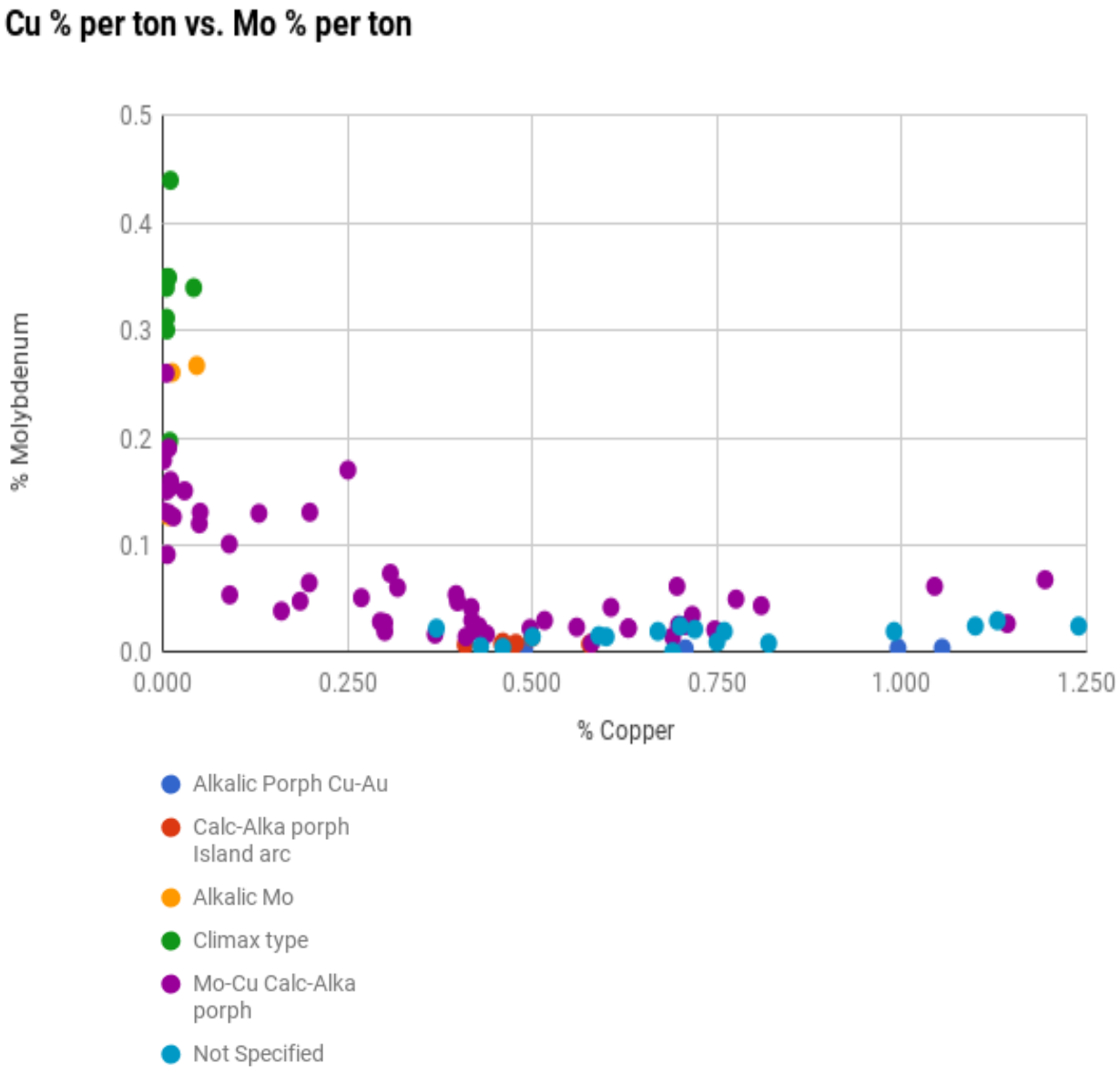

Figure 1: Distribution of porphyry metal deposits.
Scatter plot depicting the grades of Molybdenum versus Copper form porphyry mines. Categorized by deposit types. The majority of mined deposits fall into mixed metal deposits.

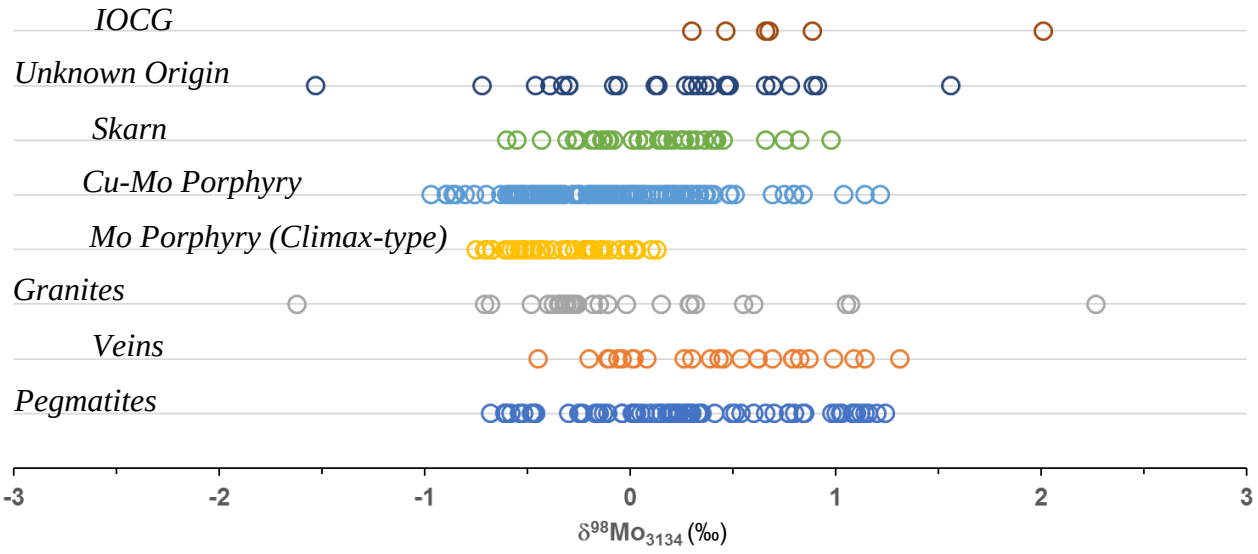

Figure 2: Distribution of Mo isotope compositions of MoS_2.
Data from Breillat et al., (2016).

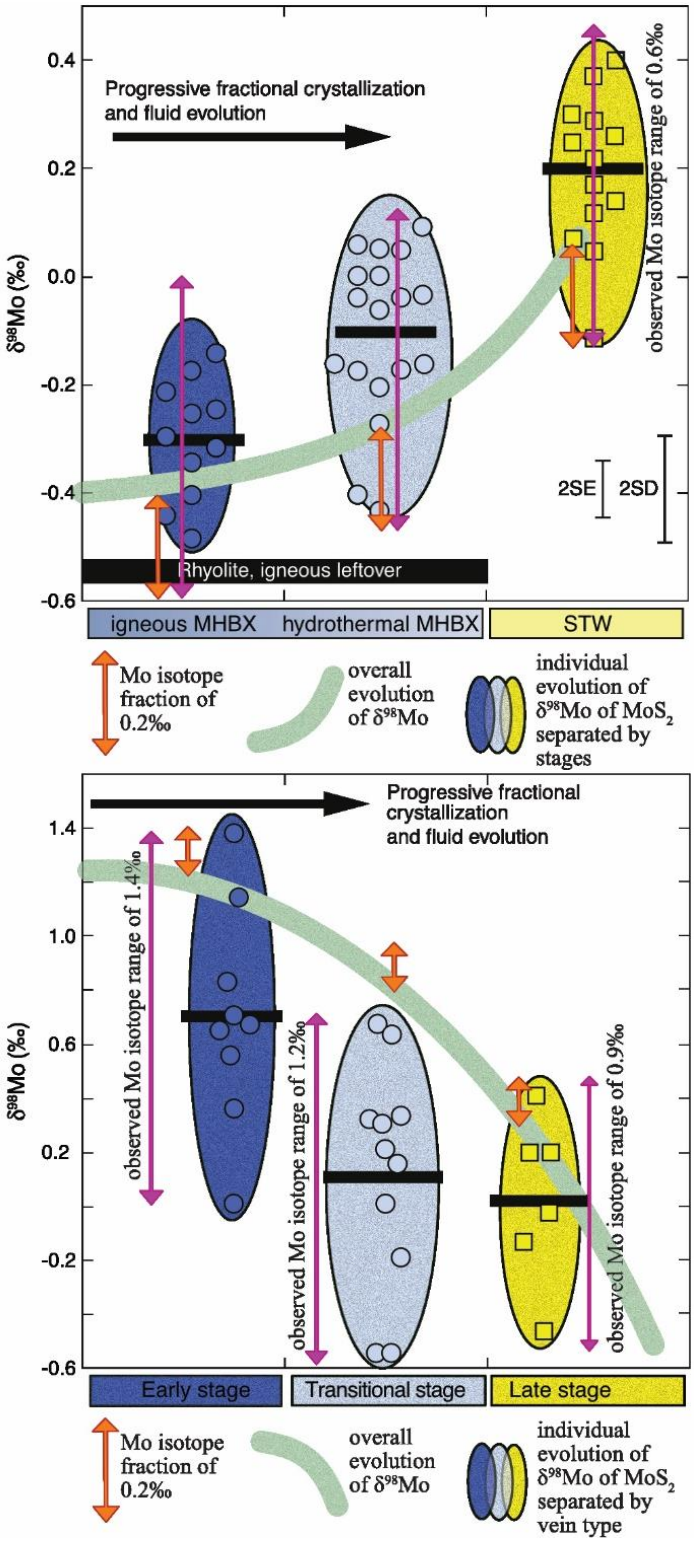

Figure 3: Porphyry trends of Mo isotope compositions of MoS_2.
Mo-only (top) and Cu-Mo (bottom) porphyry deposits. Note different scales, data from Greber et al. (2014) spans a range of 1‰ in δ^{98}Mo (top) and Shafiei et al. (2015) covers a range of 2‰ (δ^{98}Mo, bottom). Design concept from Greber et al. (2014).

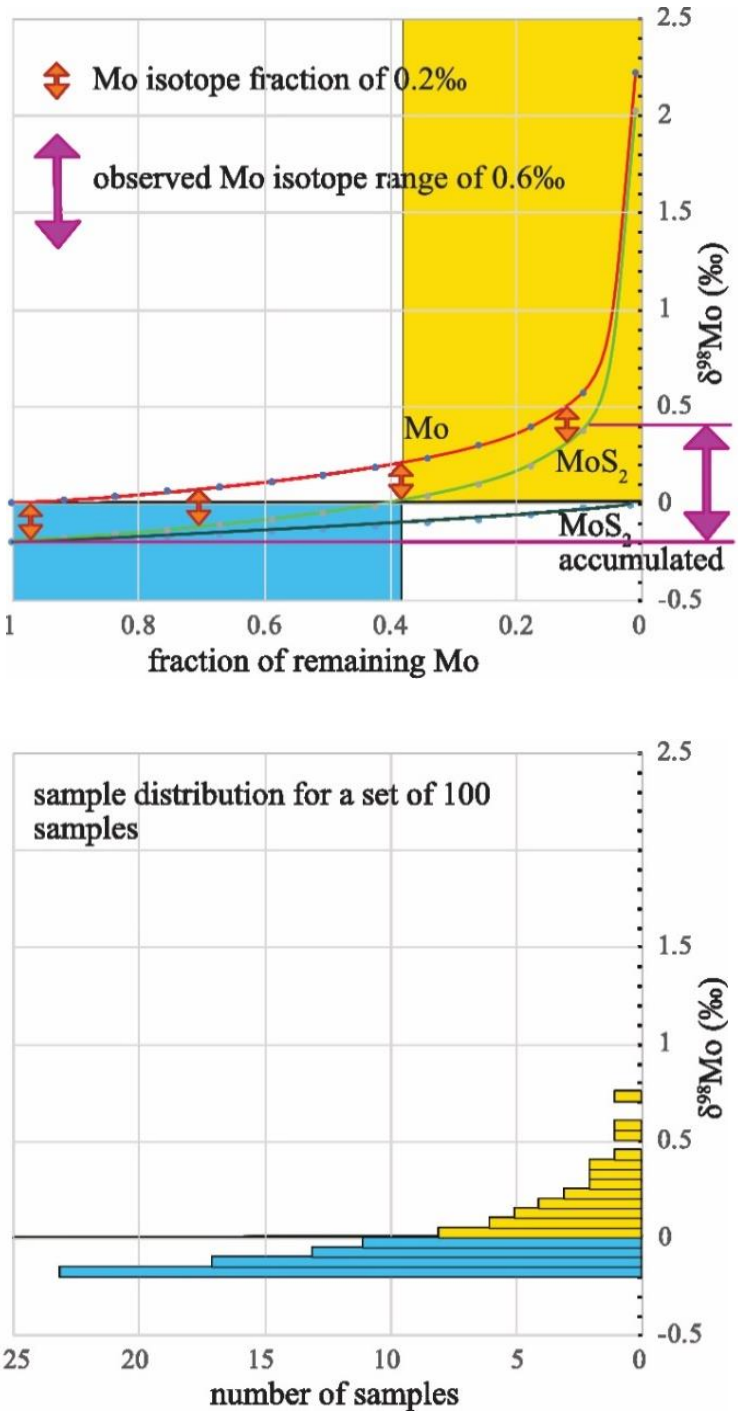

Figure 4: Rayleigh isotope predictions for data distributions.
Rayleigh isotope fractionation could be responsible for the large spread in Mo isotope signatures of ore deposits, and of individual stages in ore deposit evolution (top). Data for a Rayleigh fractionation process should display a non-normal distribution (bottom).

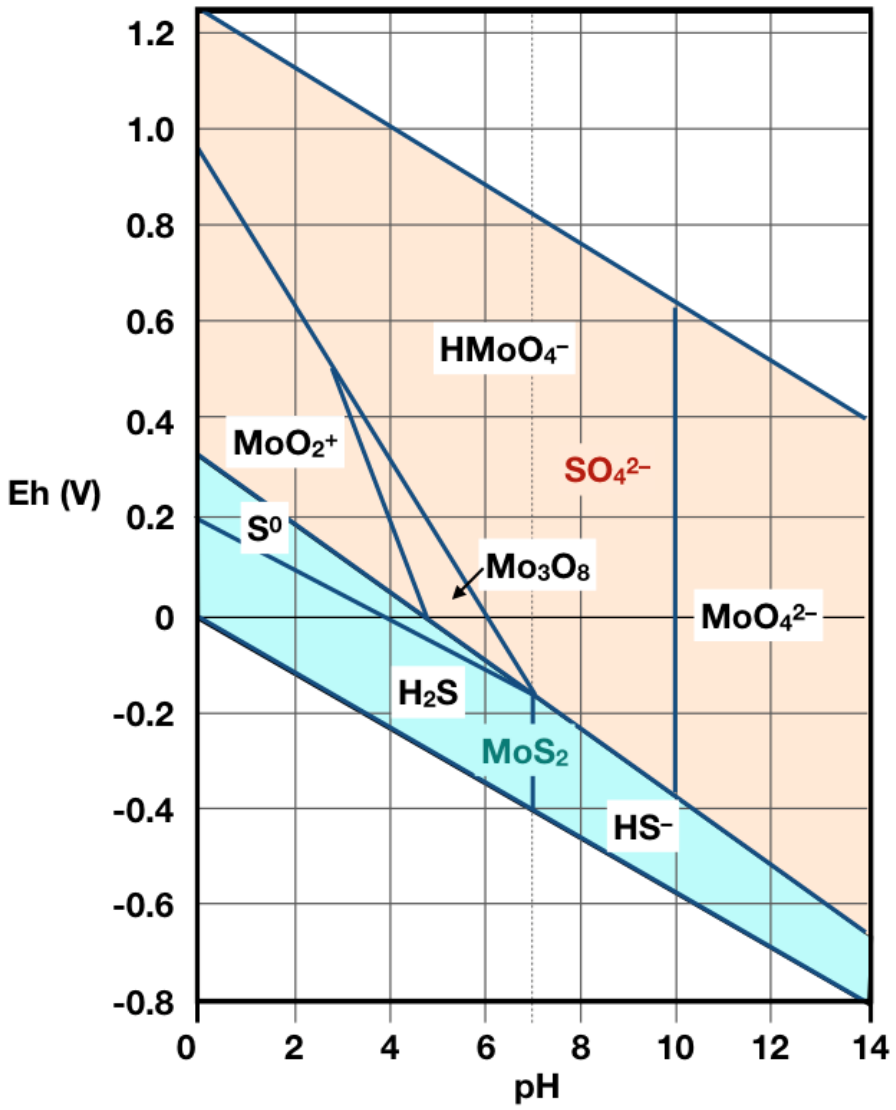

Figure 5: Eh-Ph diagram for molybdenum and sulfur species.
The figure is an overlay of a sulfur speciation diagram (25 ºC, 10 mM S; (Vesper et al., 2008, based on Drever, 1997) and a molybdenum-sulfur speciation diagram (25 ºC, 1 bar, 1 mM S, 10^{-5} mM Mo; Brookins, 1988). The sulfate (SO_4^{2-}) stability field is indicated in orange, the molybdenite (MoS_2) stability field in light blue. This overlay is intended to highlight the interdependency of Mo and S speciation and species richness but does not claim accuracy (to achieve the latter, more sophisticated approaches would be required (Huang, 2016). Much of the Mo-S-O-H speciation relationships is unknown, and alternative diagrams have been proposed (e.g. Wang, 2012; Kendall et al., 2017; Smedley and Kinniburgh, 2017; Neely et al., 2018). However, reliable data for high-temperature and pressure conditions, as well as presence of complexing agents (H^+, Cl^-, HS^-, etc) is currently not available.

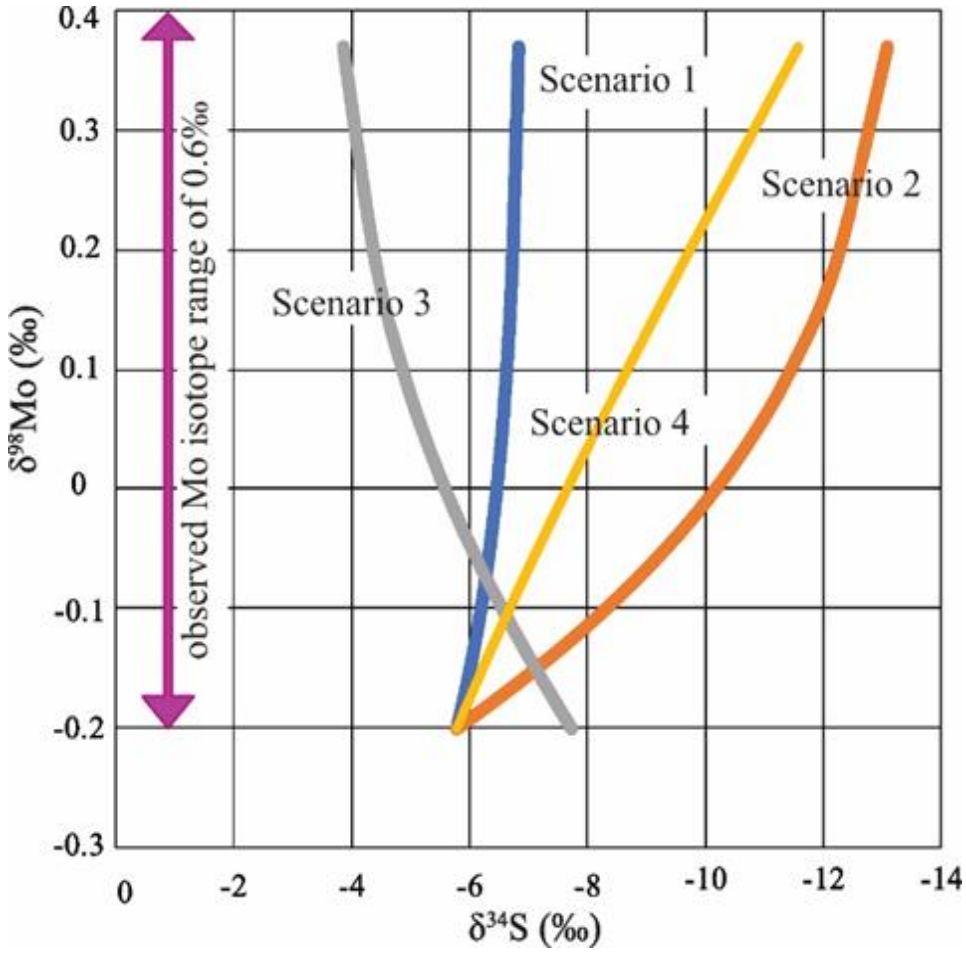

Figure 6: Scenarios for Mo and S co-evolution during MoS_2 formation.
Scenario 1 – isotope equilibrium between reduced and oxidized S species
Scenario 2 – sulfur dioxide disproportion
Scenario 3 – sulfate reduction
Scenario 4 – precipitation of MoS_2 from a limited sulfide pool)

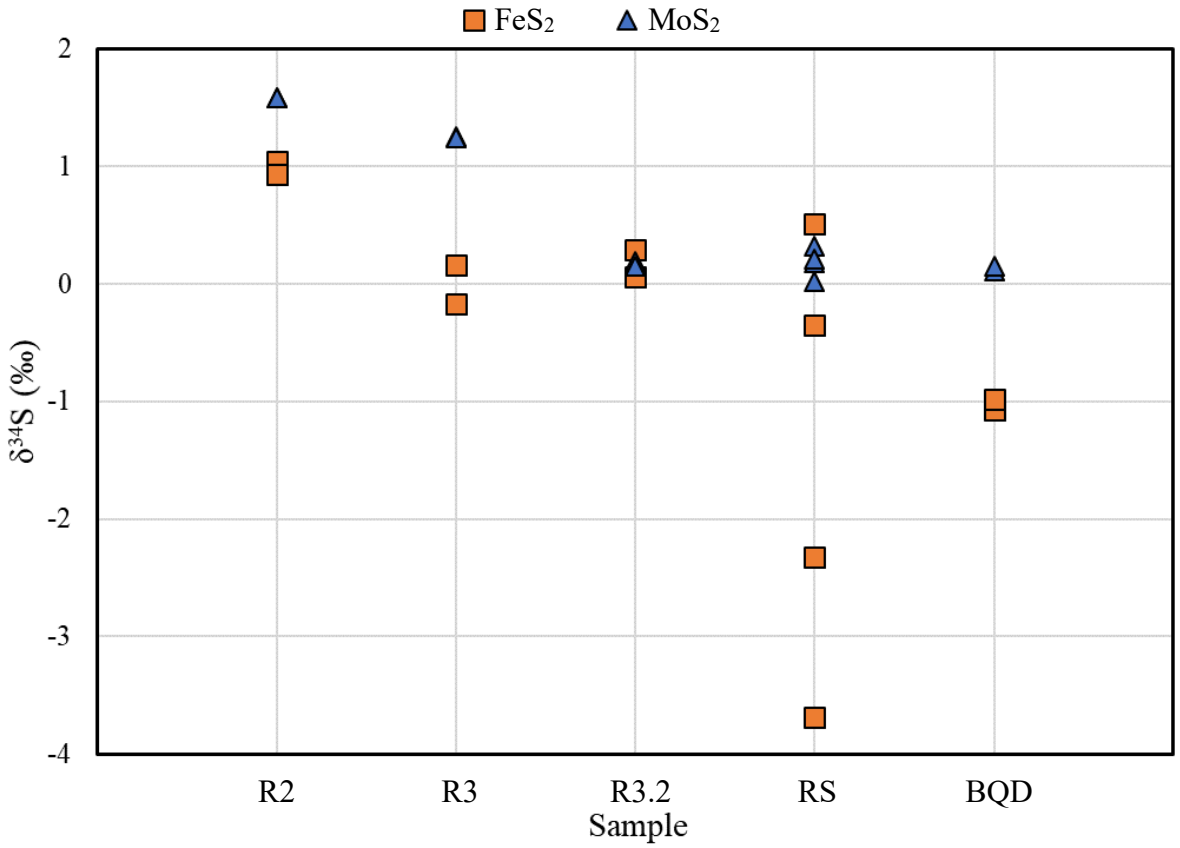

Figure 7: Pilot study data.
Sulfur isotope offset between molybdenite and pyrite is ~ +1‰, which is larger than what would be expected from equilibrium fractionation at the reported formation temperatures for the deposit.

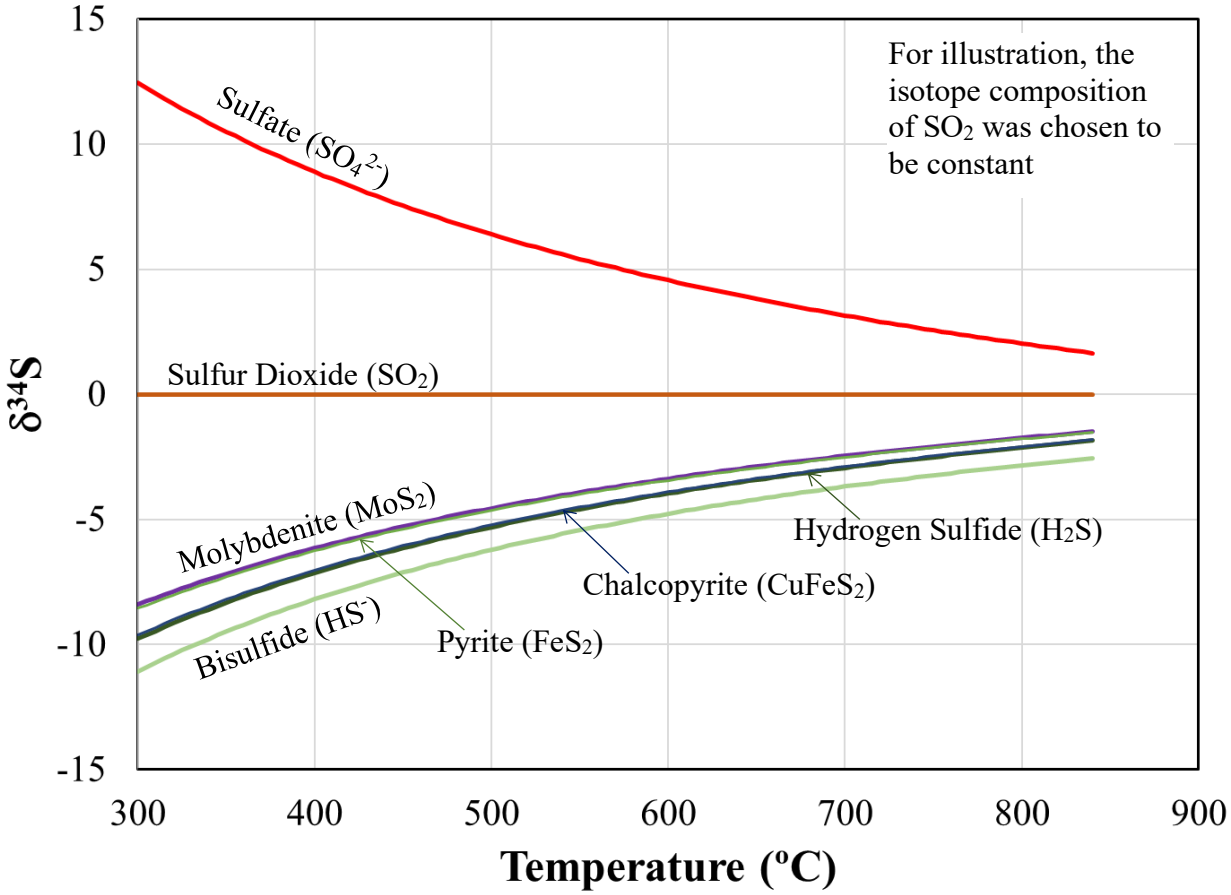

Figure 8: Equilibrium isotope fractionation between S compounds at different temperatures. For illustration, the isotope composition of sulfur dioxide was chosen to be constant.

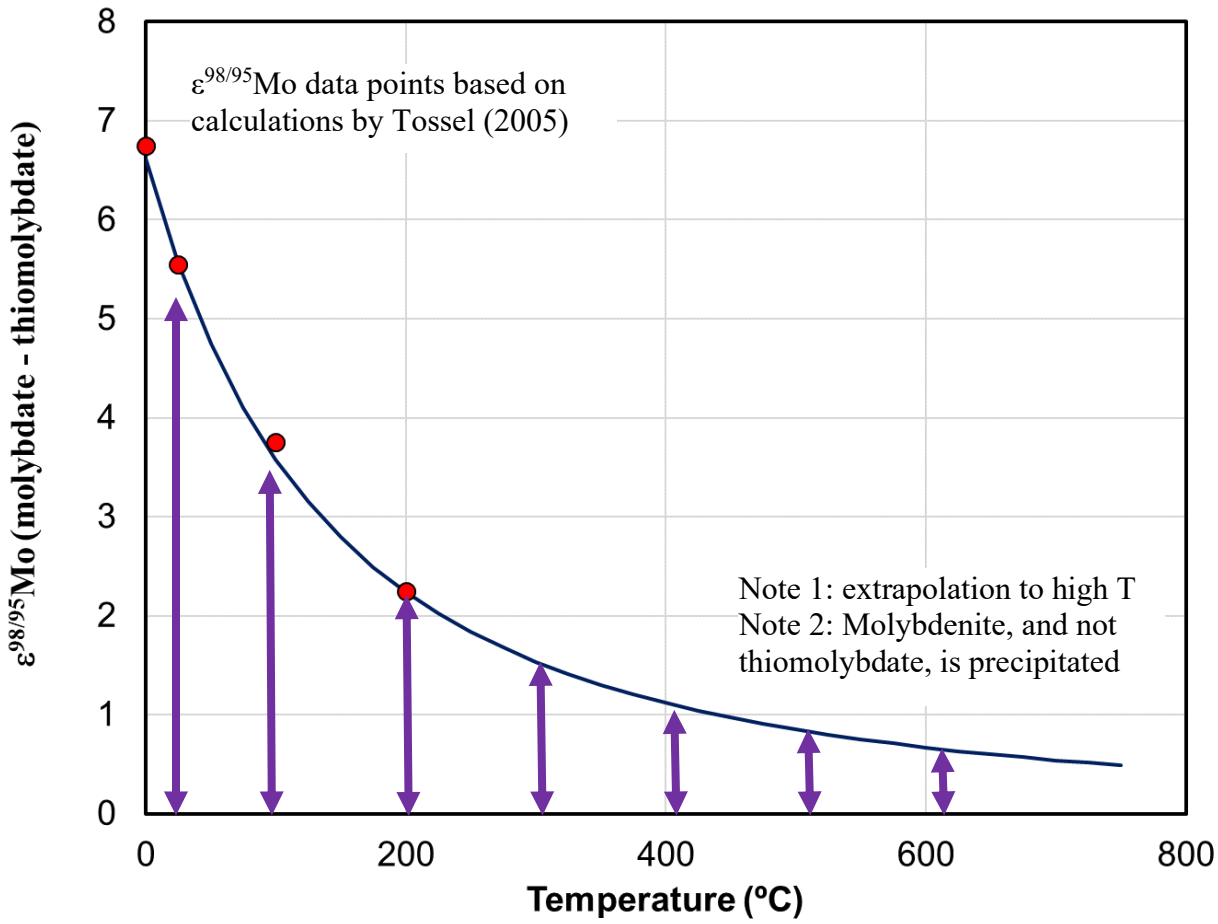

Figure 9: Isotope fractionation between molybdate (MoO_4^{2-}) and thiomolybdate (MoS_4^{2-}). Extrapolated from Tossell, 2005.

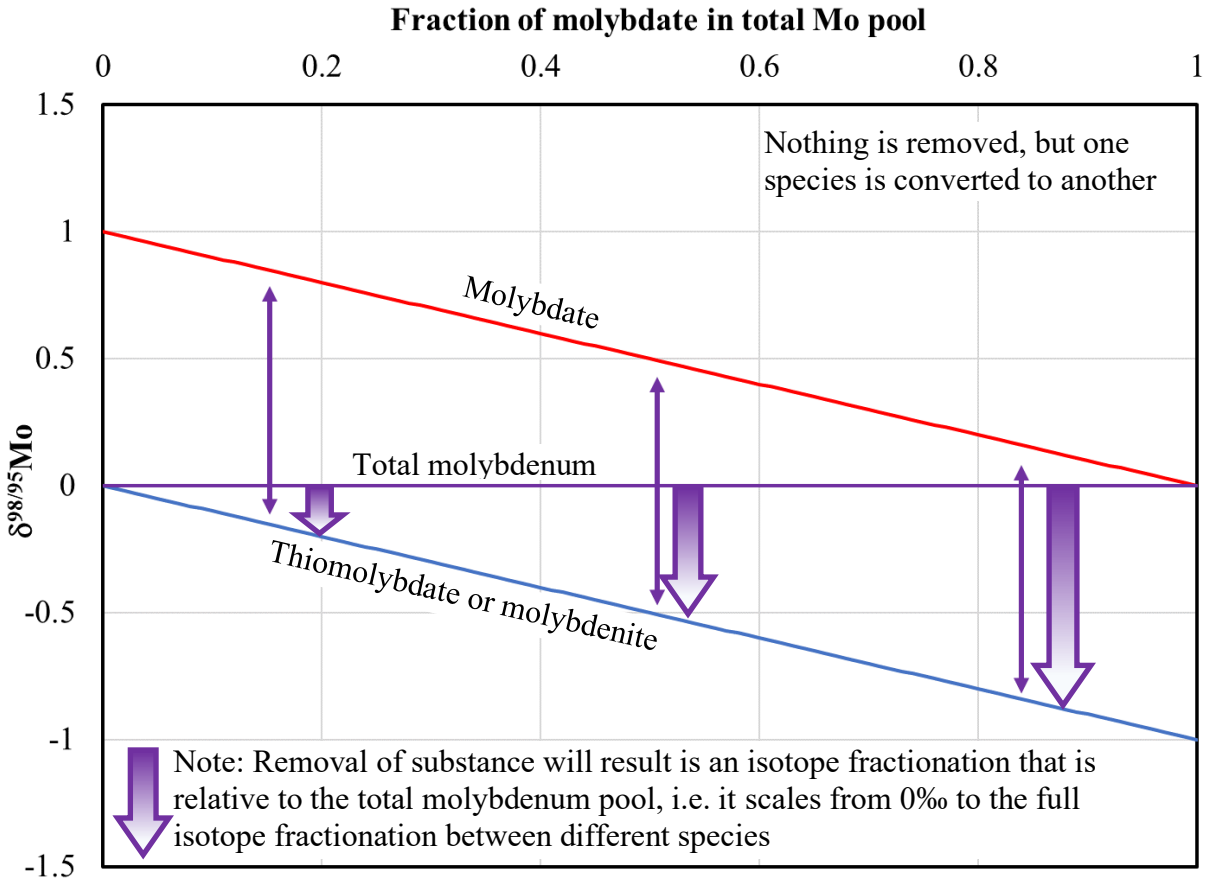

Figure 10: Equilibrium isotope fractionation between Mo species.
Illustration that with only changes in speciation i.e. molybdate to thiomolybdate, a considerable range of isotope values can be obtained.

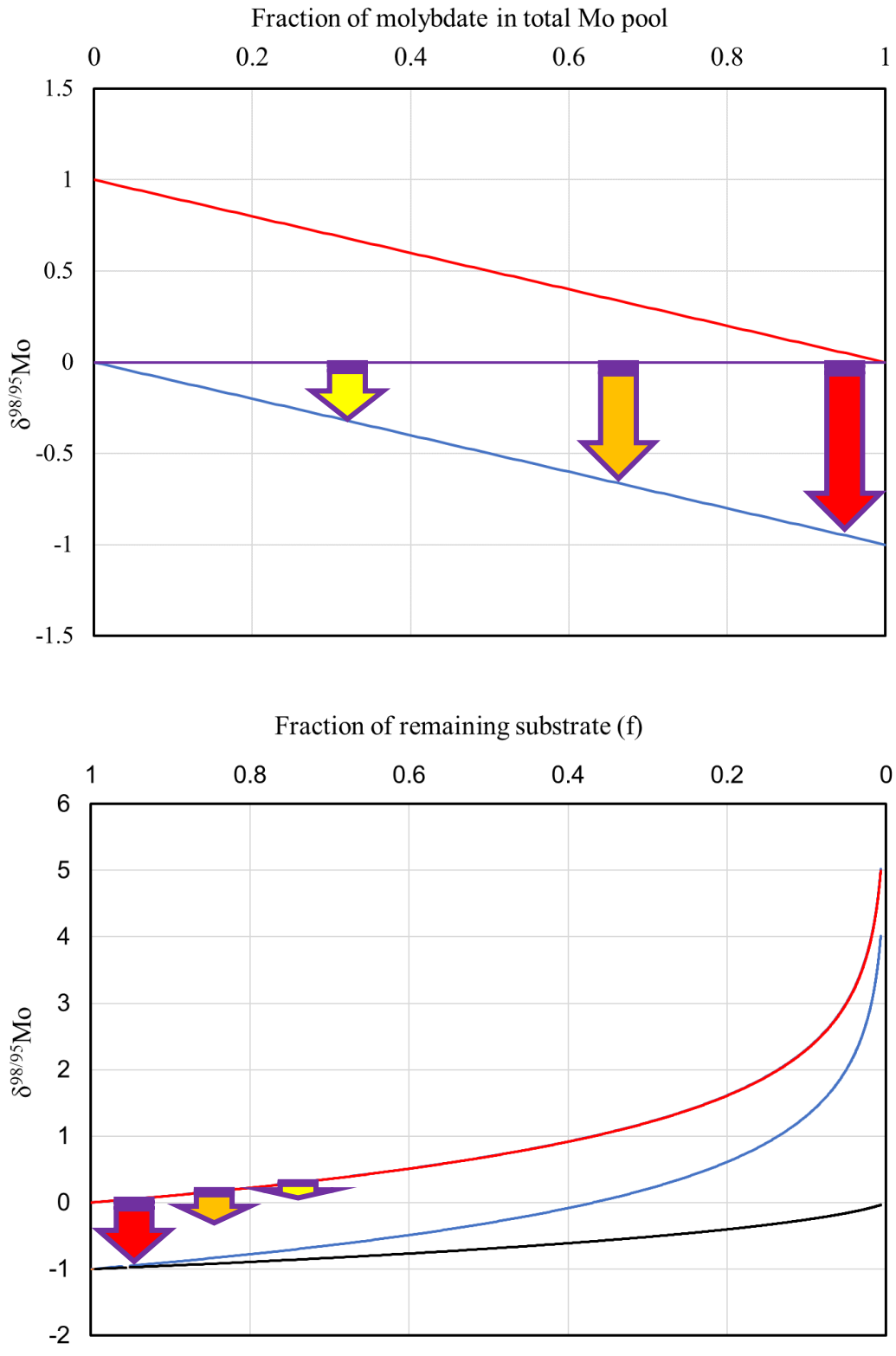

Figure 11: Rayleigh isotope distillation and equilibrium isotope fractionation in concert.
Note: Removal of substance will result in an isotope fractionation that is relative to the total molybdenum pool, and not directly on the molybdate (substrate) pool.

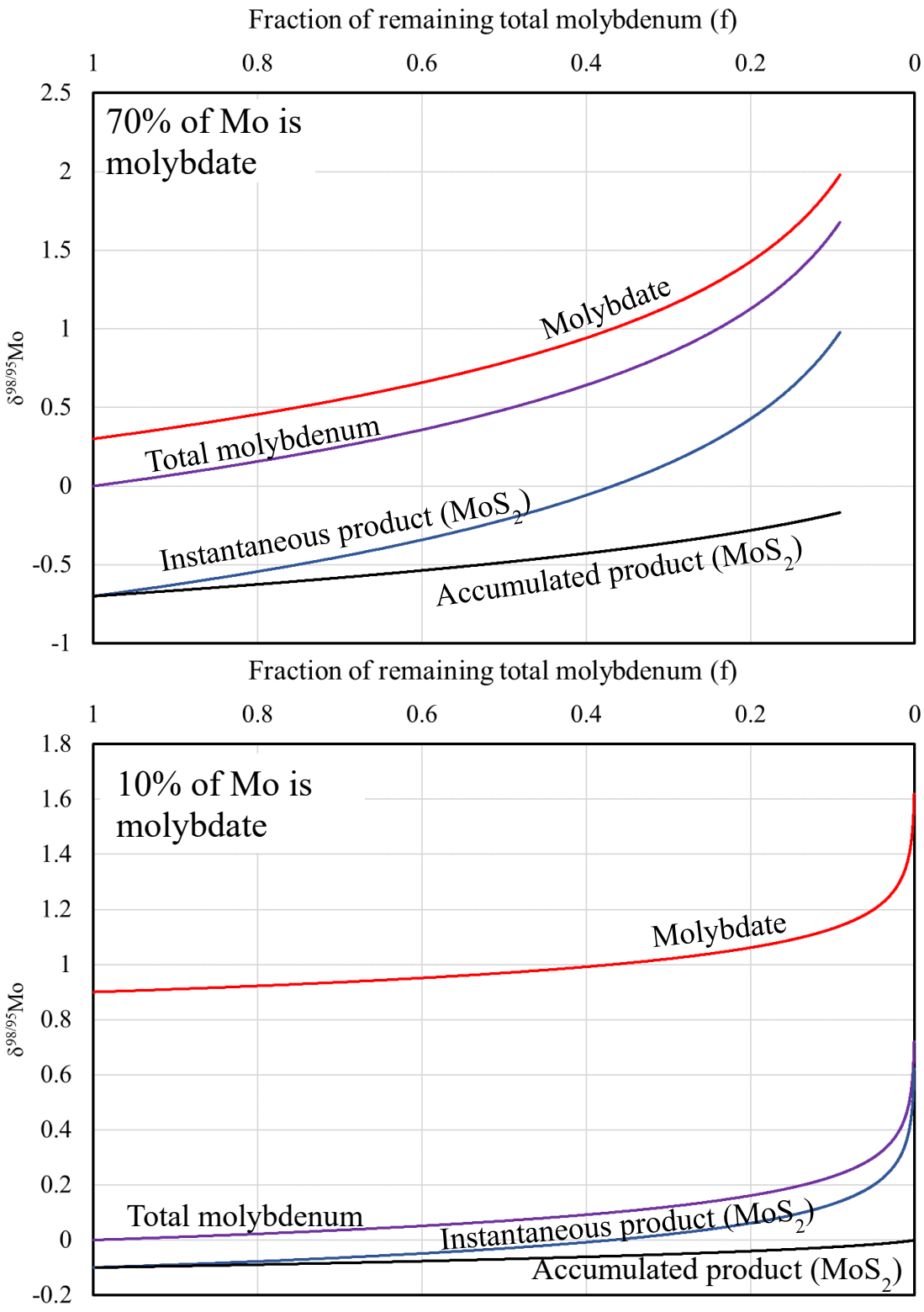

Figure 12: Scenario 1 – Fixed ratio between two Mo species.
During Rayleigh distillation. Given different initial ratios the Rayleigh trends can be exaggerated (top) or suppressed (bottom).

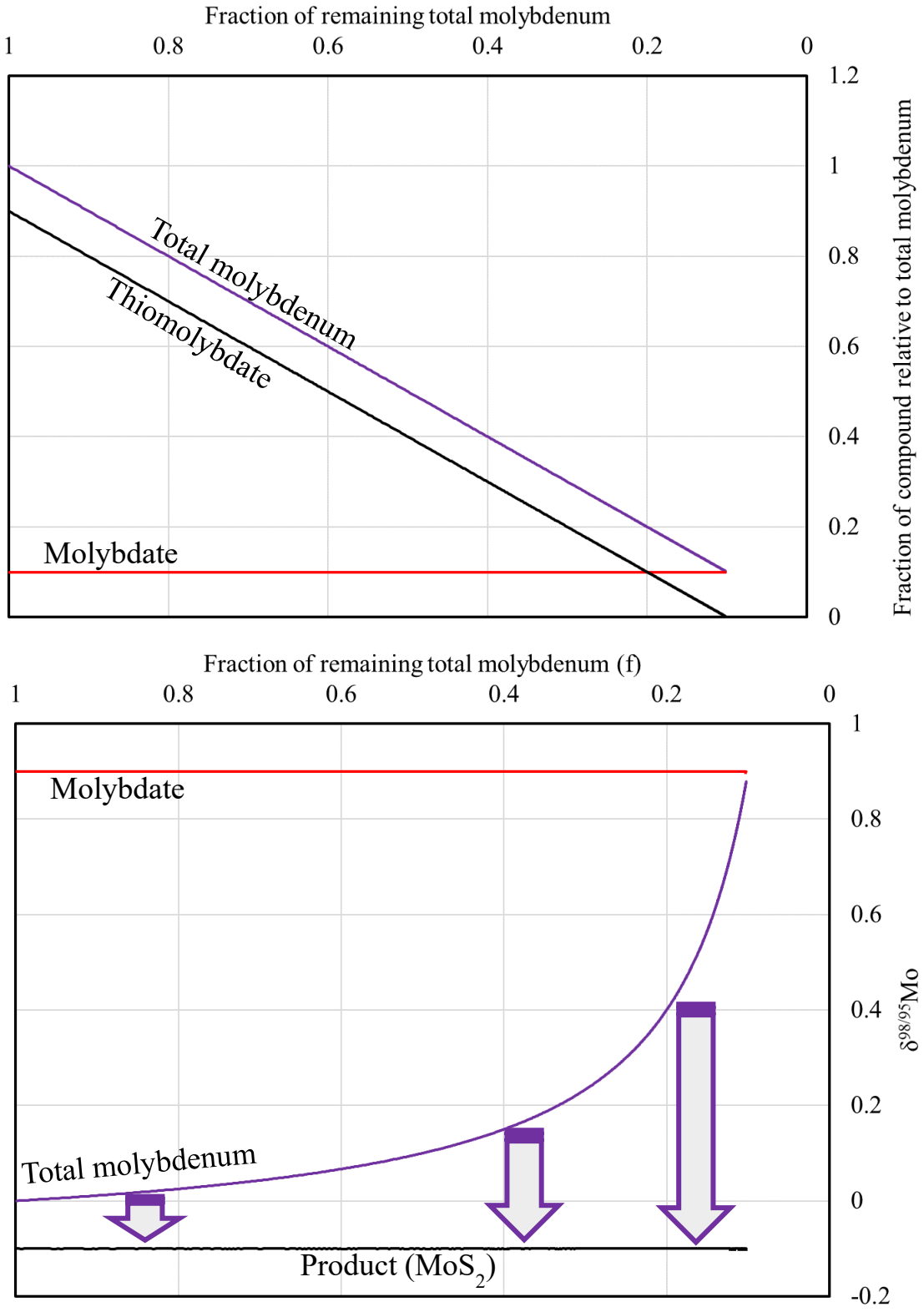

Figure 13: Scenario 2 – One species does not change, the other is consumed.
This ultimately results in no change between the measured isotopic composition.

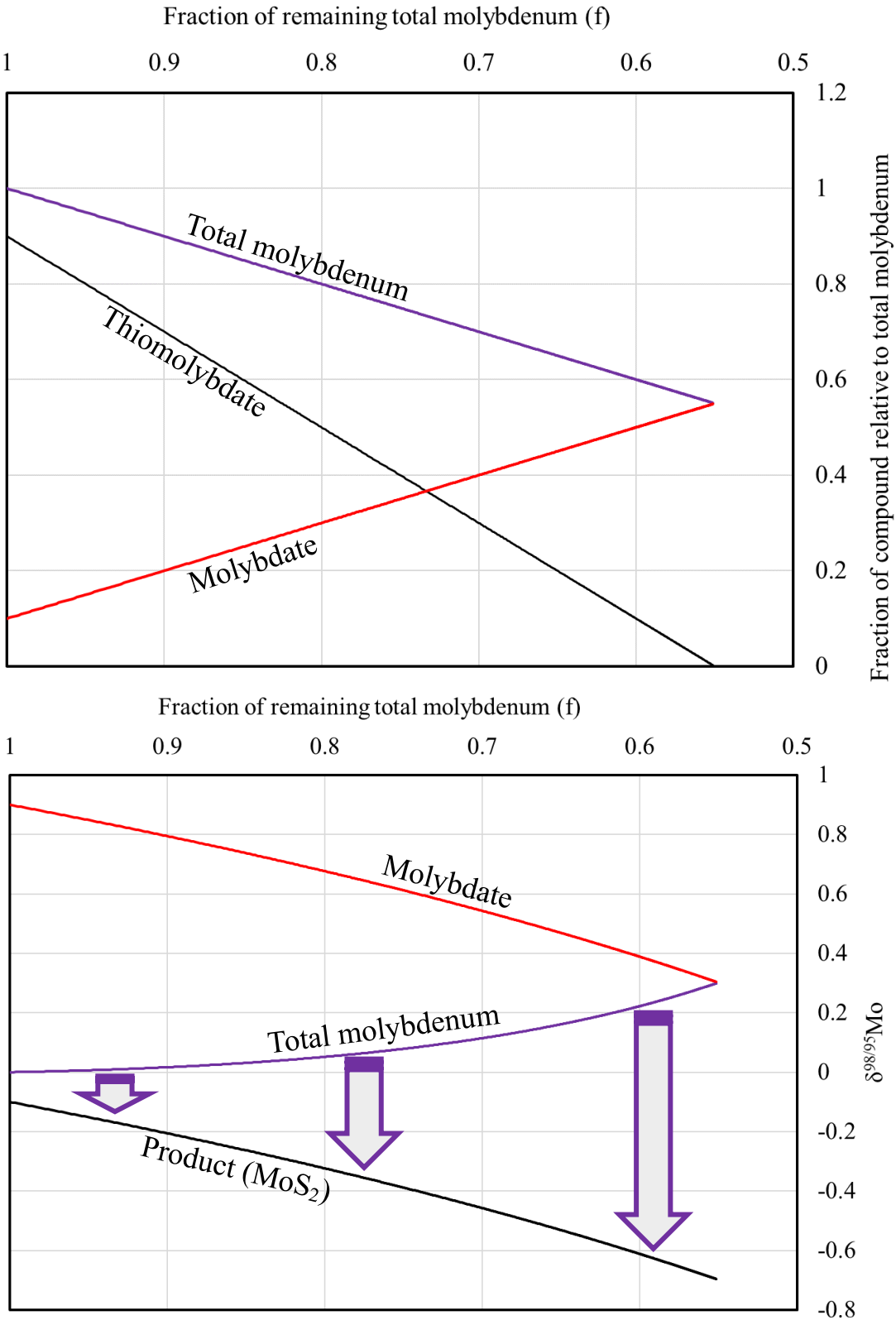

Figure 14: Scenario 3 – One species increases, the other is consumed.
This results in an apparent reverse Rayleigh-like trend.

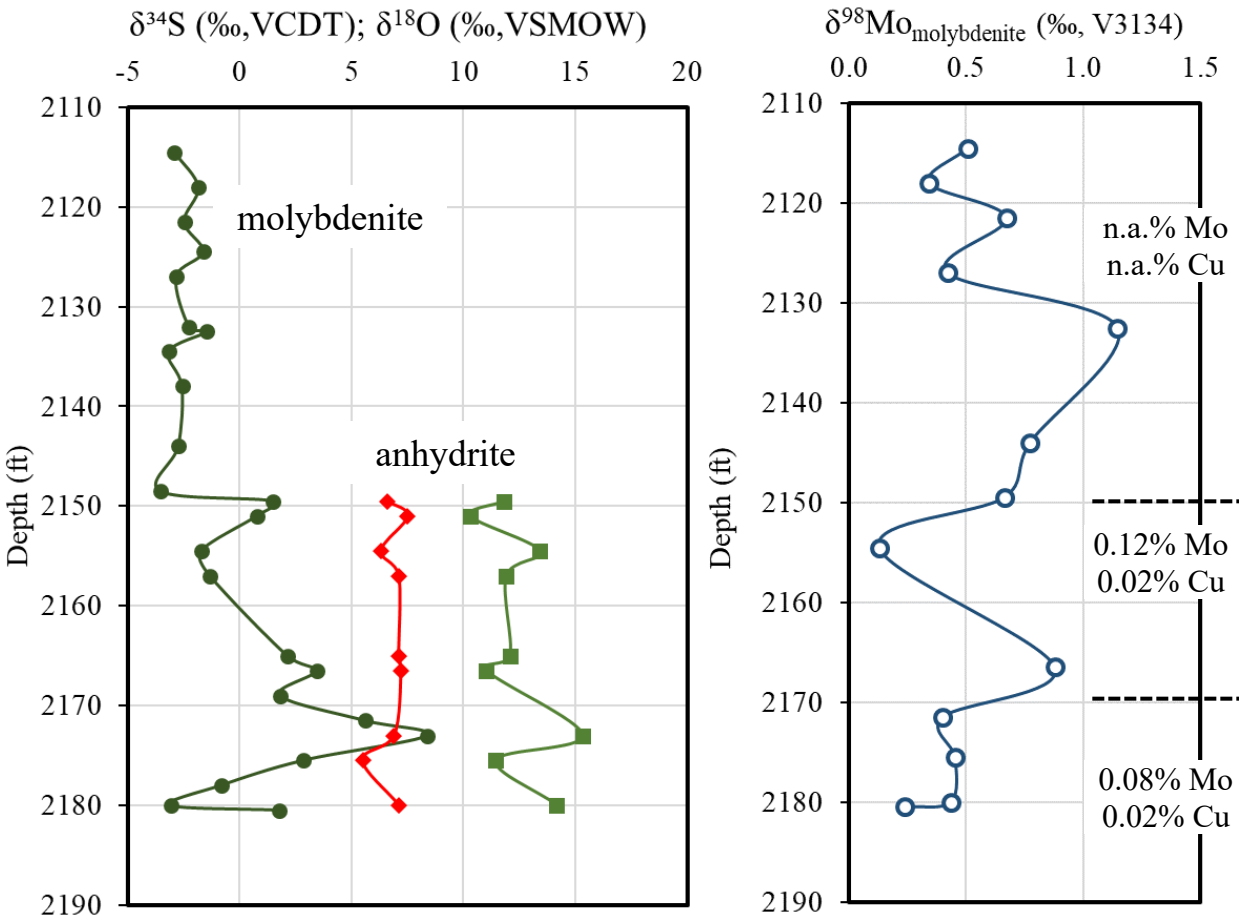

Figure 15: Mo, S and O isotope composition results: core D2406.

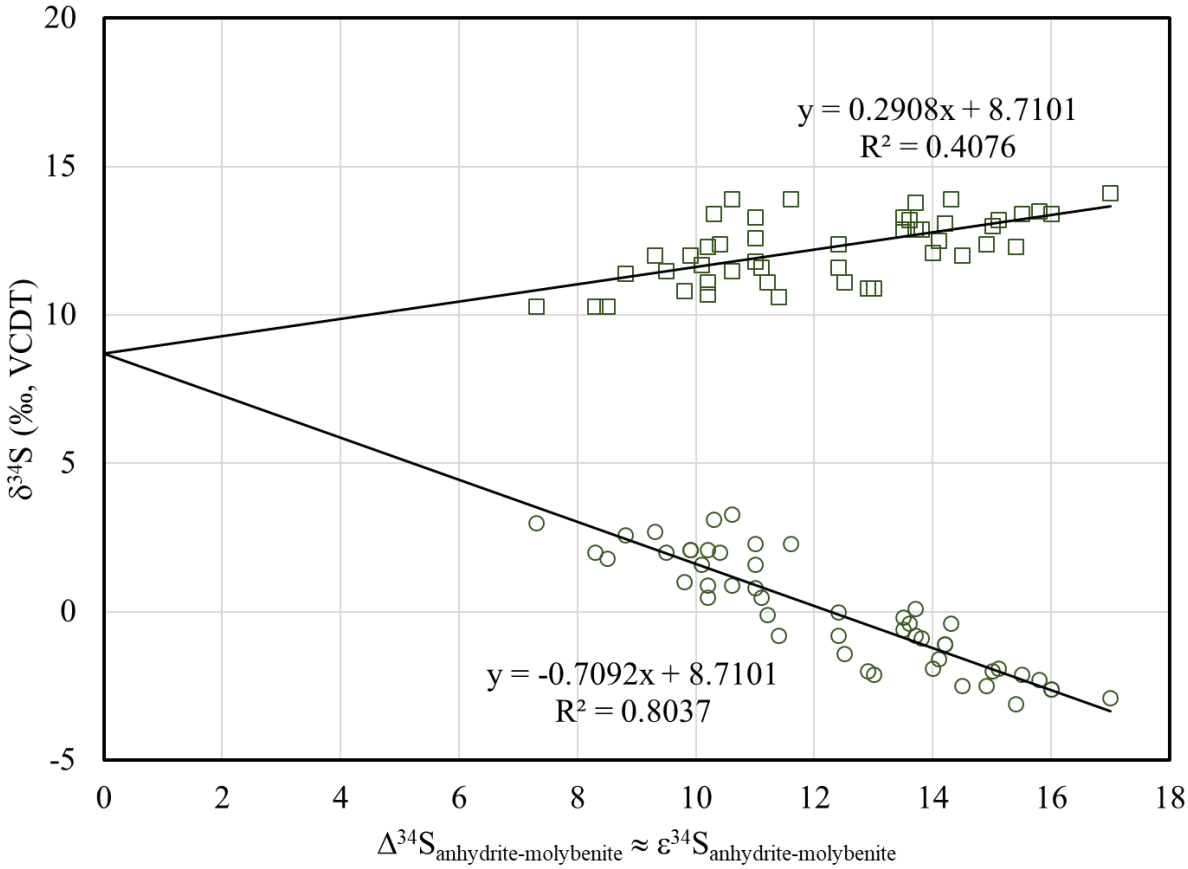

Figure 16: Sulfur – sulfur isotope plot with randomly generated data.
This exercise demonstrates the risk of drawing conclusions from such a plot. Randomly generated set of numbers can be shown to be correlated.

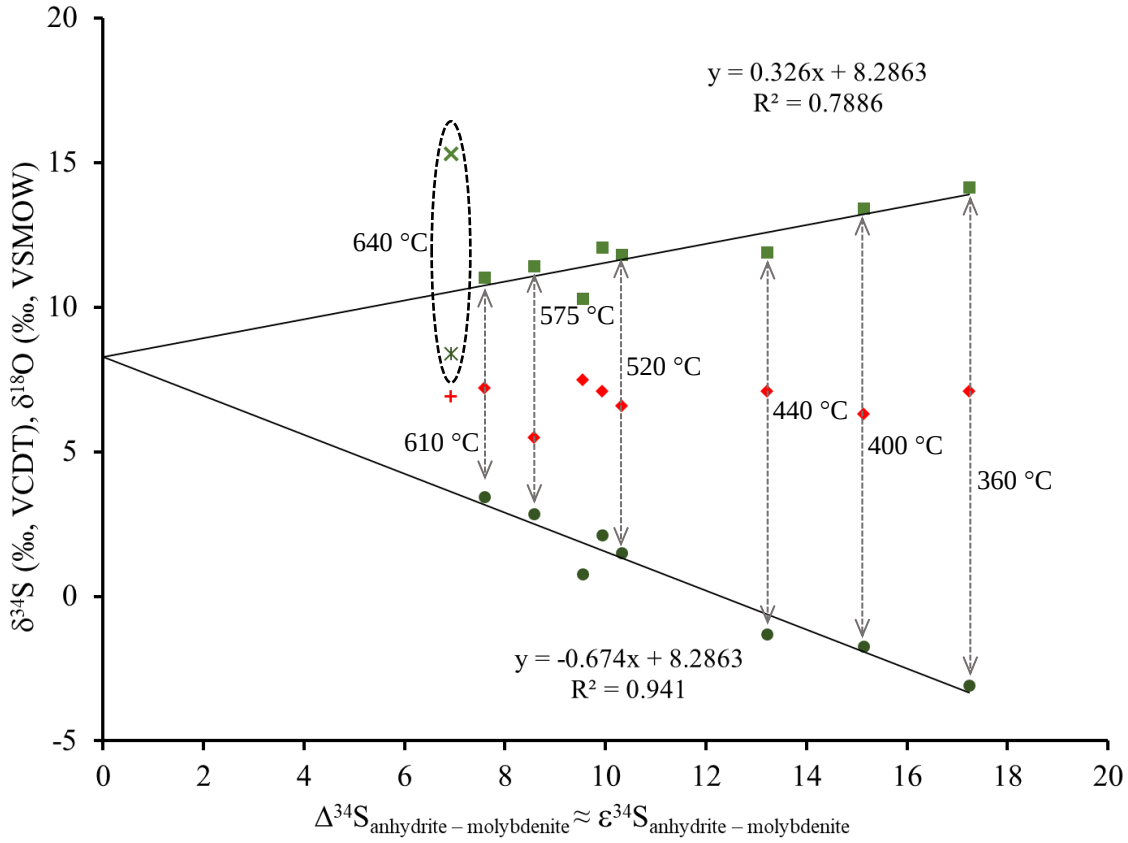

Figure 17: Sulfur – sulfur isotope plot with real data.
Showing a strong equilibrium correlation between anhydrite and molybdenite. Also of note is the consistently larger sulfate pool compared to the sulfide 67% - 33%. Supporting sulfur dioxide disproportionation, which results in 75:25 stoichiometry of sulfate and sulfide.

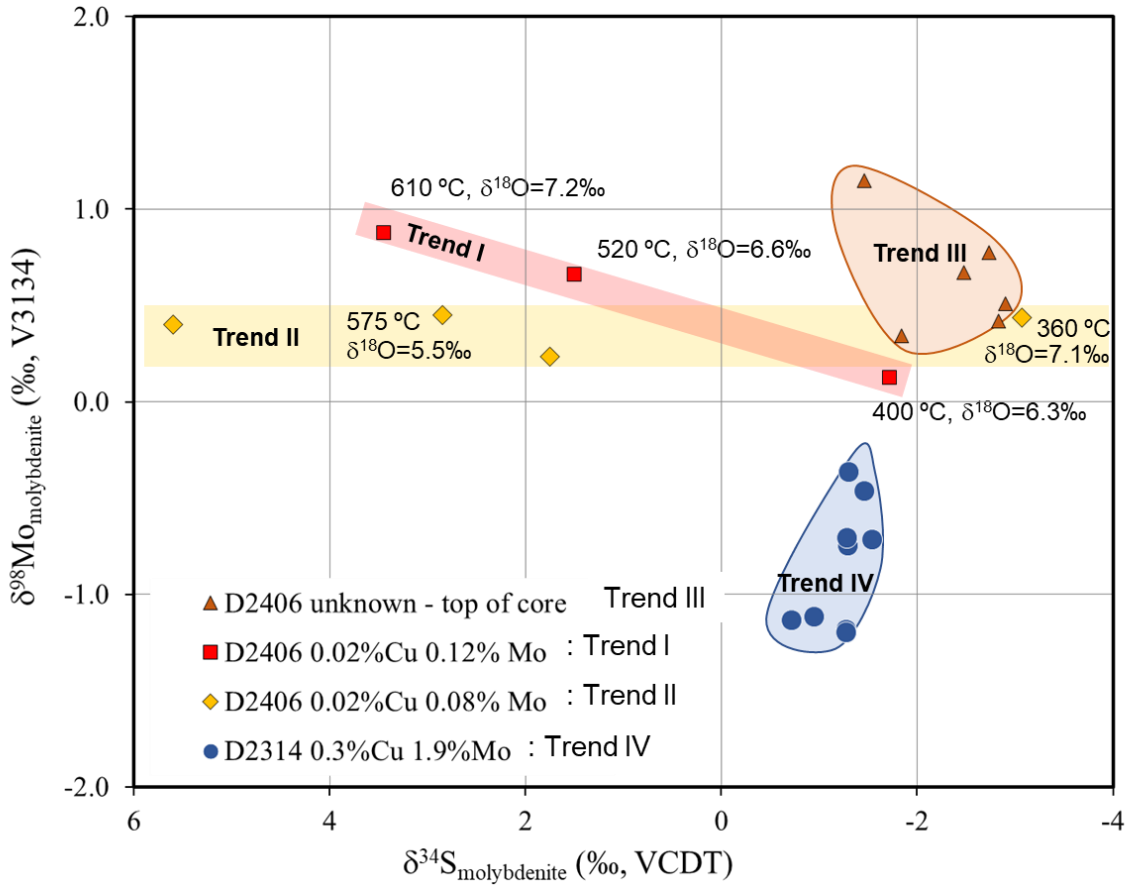

Figure 18: S – Mo Isotope Results - Main study data compilation with interpreted trends.

Trend 1 - molybdenum and sulfur get lighter together with decreasing temperature.
An equilibrium process controlled by SO_2 disproportionation in the presence of Ca^+.

Trend 2 – molybdenum doesn't change, while sulfur gets lighter
An equilibrium prosses controlled by SO_2 disproportionation in the presence of Ca^+.
No change of the Mo isotopes suggests a large pool or rapid consumption.

Trend 3 – a cluster of heavy molybdenum and light sulfur
An Equilibrium process, SO_2 disproportionation no longer dependent on the availability of Ca^+
mineralization taps into the remaining heavy Mo pool and light S pool.

Trend 4 – a cluster of light molybdenum and light sulfur.
A likely Rayleigh trend, Mo sourced from the fluids and not vapor.

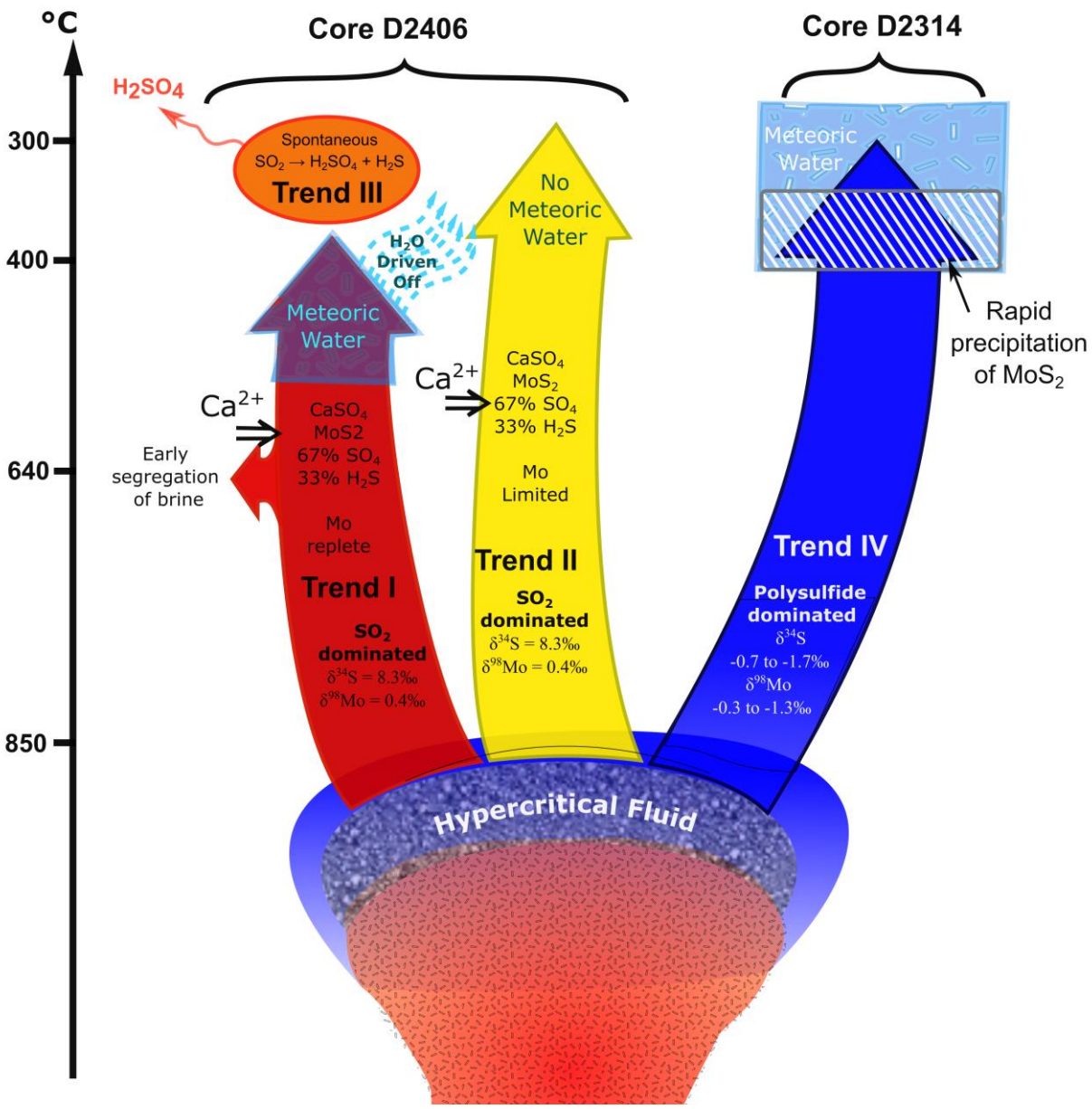

Figure 19: Synthesis of reactions and evolution of the Santa Rita deposit.

References Cited

Ahmad, S.N., and Rose, A.W., 1980, Fluid inclusions in porphyry and skarn ore at Santa Rita, New Mexico: Economic Geology, v. 75, p. 229–250.

Anbar, A.D., Knab, K.A., and Barling, J., 2001, Precise Determination of Mass-Dependent Variations in the Isotopic Composition of Molybdenum Using MC-ICPMS: Analytical Chemistry, v. 73, p. 1425–1431.

Arnold, G.L., Anbar, A.D., Barling, J., and Lyons, T.W., 2004, Molybdenum isotope evidence for widespread anoxia in mid-proterozoic oceans: Science, v. 304, p. 87–90.

Barling, J., Arnold, G.L., and Anbar, A.D., 2001, Natural mass-dependent variations in the isotopic composition of molybdenum: Earth and Planetary Science Letters, v. 193, p. 447–457.

Breillat, N., Guerrot, C., Marcoux, E., and Négrel, Ph., 2016, A new global database of δ98Mo in molybdenites: A literature review and new data: Journal of Geochemical Exploration, v. 161, p. 1–15.

Brookins, D.G., 1988, Eh-pH diagrams for geochemistry: Germany, Springer, 176 p., http://inis.iaea.org/search/search.aspx?orig_q=RN:20029173.

Burgisser, A., Alletti, M., and Scaillet, B., 2015, Simulating the behavior of volatiles belonging to the C–O–H–S system in silicate melts under magmatic conditions with the software D-Compress: Computers & Geosciences, v. 79, p. 1–14.

Burgisser, A., and Scaillet, B., 2007, Redox evolution of a degassing magma rising to the surface: Nature, v. 445, p. 194.

Cooke, D.R., Hollings, P., Wilkinson, J.J., and Tosdal, R.M., 2014a, Geochemistry of Porphyry Deposits, *in* Treatise on Geochemistry, Elsevier, p. 357–381.

Drever, J.I., 1997, The geochemistry of natural waters: Surface and groundwater environments: Prentice Hall, 436 p.

Driesner, T., and Heinrich, C.A., 2007, The system H2O–NaCl. Part I: Correlation formulae for phase relations in temperature–pressure–composition space from 0 to 1000 C, 0 to 5000 bar, and 0 to 1 XNaCl: Geochimica et Cosmochimica Acta, v. 71, p. 4880–4901.

Faure, G., 1986, Principles of isotope geology. Second edition:, https://www.osti.gov/scitech/biblio/5648561 (accessed July 2017).

Fekete, S., Weis, P., Driesner, T., Bouvier, A.-S., Baumgartner, L., and Heinrich, C.A., 2016, Contrasting hydrological processes of meteoric water incursion during magmatic–hydrothermal ore deposition: An oxygen isotope study by ion microprobe: Earth and Planetary Science Letters, v. 451, p. 263–271.

Field, C.W., and Gustafson, L.B., 1976, Sulfur isotopes in the porphyry copper deposit at El Salvador, Chile: Economic Geology, v. 71, p. 1533–1548.

Gallagher, V., Feely, M., Högelsberger, H., Jenkin, G.R.T., and Fallick, A.E., 1992, Geological, fluid inclusion and stable isotope studies of Mo mineralization, Galway Granite, Ireland: Mineralium Deposita, v. 27, p. 314–325.

Giggenbach, W., 1992, Magma degassing and mineral deposition in hydrothermal systems along convergent plate boundaries.: Econ. Geol., v. 87, p. 1927–1944.

Goldberg, T., Gordon, G., Izon, G., Archer, C., Pearce, C.R., McManus, J., Anbar, A.D., and Rehkämper, M., 2013, Resolution of inter-laboratory discrepancies in Mo isotope data: an intercalibration: Journal of Analytical Atomic Spectrometry, v. 28, p. 724–735.

Greber, N.D., Hofmann, B.A., Voegelin, A.R., Villa, I.M., and Nägler, T.F., 2011, Mo isotope composition in Mo-rich high- and low-T hydrothermal systems from the Swiss Alps: Geochimica et Cosmochimica Acta, v. 75, p. 6600–6609.

Greber, N.D., Pettke, T., and Nägler, T.F., 2014a, Magmatic–hydrothermal molybdenum isotope fractionation and its relevance to the igneous crustal signature: Lithos, v. 190–191, p. 104–110.

Greber, N.D., Siebert, C., Nägler, T.F., and Pettke, T., 2012, δ98/95Mo values and Molybdenum Concentration Data for NIST SRM 610, 612 and 3134: Towards a Common Protocol for Reporting Mo Data: Geostandards and Geoanalytical Research, v. 36, p. 291–300.

Gustafson, L.B., and Hunt, J.P., 1975, The porphyry copper deposit at El Salvador, Chile: Economic Geology, v. 70, p. 857–912.

Hannah, J.L., Stein, H.J., Wieser, M.E., de Laeter, J.R., and Varner, M.D., 2007, Molybdenum isotope variations in molybdenite: Vapor transport and Rayleigh fractionation of Mo: Geology, v. 35, p. 703–706.

Hellingwerf, R.H., Baker, J.H., and Raaphorst, J.G.V., 1987, Sulphur isotope data of Proterozoic molybdenites from western Bergslagen, Sweden: Geologiska Föreningen i Stockholm Förhandlingar, v. 109, p. 33–38.

Hemley, J.J., and Jones, W., 1964, Chemical aspects of hydrothermal alteration with emphasis on hydrogen metasomatism: Economic Geology, v. 59, p. 538–569.

Hoefs, J., 2008, Stable Isotope Geochemistry: Springer-Verlag Berlin Heidelberg, https://www.springer.com/us/book/9783642089602.

Holland, H.D., 1965, Some applications of thermochemical data to problems of ore deposits;[Part] 2, Mineral assemblages and the composition of ore forming fluids: Economic Geology, v. 60, p. 1101–1166.

Huang, H.-H., 2016, The Eh-pH Diagram and Its Advances: Metals, v. 6, p. 23.

Kendall, B., Dahl, T.W., and Anbar, A.D., 2017, The stable isotope geochemistry of molybdenum: Reviews in Mineralogy and Geochemistry, v. 82, p. 683–732.

Kessel, R., Schmidt, M.W., Ulmer, P., and Pettke, T., 2005, Trace element signature of subduction-zone fluids, melts and supercritical liquids at 120–180 km depth: Nature, v. 437, p. 724.

Klemm, L.M., Pettke, T., and Heinrich, C.A., 2008, Fluid and source magma evolution of the Questa porphyry Mo deposit, New Mexico, USA: Mineralium Deposita, v. 43, p. 533.

Kokh, M.A., Lopez, M., Gisquet, P., Lanzanova, A., Candaudap, F., Besson, P., and Pokrovski, G.S., 2016, Combined effect of carbon dioxide and sulfur on vapor–liquid partitioning of metals in hydrothermal systems: Geochimica et Cosmochimica Acta, v. 187, p. 311–333.

Kouzmanov, K., and Pokrovski, G.S., 2012, Hydrothermal controls on metal distribution in porphyry Cu (-Mo-Au) systems:

Landtwing, M.R., Pettke, T., Halter, W.E., Heinrich, C.A., Redmond, P.B., Einaudi, M.T., and Kunze, K., 2005, Copper deposition during quartz dissolution by cooling magmatic–hydrothermal fluids: the Bingham porphyry: Earth and Planetary Science Letters, v. 235, p. 229–243.

Lang, J.R., Guan, Y., and Eastoe, C.J., 1989, Stable isotope studies of sulfates and sulfides in the Mineral Park porphyry Cu-Mo system, Arizona: Economic Geology, v. 84, p. 650–662.

Li, Y., McCoy-West, A.J., Zhang, S., Selby, D., Burton, K.W., and Horan, K., 2019, Controlling Mechanisms for Molybdenum Isotope Fractionation in Porphyry Deposits: The Qulong Example: Economic Geology, v. 114, p. 981–992.

Louvel, M., Bordage, A., Tripoli, B., Testemale, D., Hazemann, J.-L., and Mavrogenes, J., 2017, Effect of S on the aqueous and gaseous transport of Cu in porphyry and epithermal systems: Constraints from in situ XAS measurements up to 600°C and 300bars: Chemical Geology, v. 466, p. 500–511.

Malinovsky, D., Hammarlund, D., Ilyashuk, B., Martinsson, O., and Gelting, J., 2007, Variations in the isotopic composition of molybdenum in freshwater lake systems: Chemical Geology, v. 236, p. 181–198.

Mathur, R., Brantley, S., Anbar, A., Munizaga, F., Maksaev, V., Newberry, R., Vervoort, J., and Hart, G., 2010, Variation of Mo isotopes from molybdenite in high-temperature hydrothermal ore deposits: Mineralium Deposita, v. 45, p. 43–50.

Mavrogenes, J., and Blundy, J., 2017, Crustal sequestration of magmatic sulfur dioxide: Geology, v. 45, p. 211–214.

McKenzie, W.F., and Truesdell, A., 1977, Geothermal reservoir temperatures estimated from the oxygen isotope compositions of dissolved sulfate and water from hot springs and shallow drillholes: Geothermics, v. 5, p. 51–61.

Metrich, N., and Mandeville, C.W., 2010, Sulfur in Magmas: Elements, v. 6, p. 81–86, doi:10.2113/gselements.6.2.81.

Moretti, R., and Papale, P., 2004, On the oxidation state and volatile behavior in multicomponent gas–melt equilibria: Chemical Geology, v. 213, p. 265–280.

Naegler, T.F., Neubert, N., Boettcher, M.E., Dellwig, O., and Schnetger, B., 2011, Molybdenum isotope fractionation in pelagic euxinia: Evidence from the modern Black and Baltic Seas: Chemical Geology, v. 289, p. 1–11.

Neely, R.A., Gislason, S.R., Ólafsson, M., McCoy-West, A.J., Pearce, C.R., and Burton, K.W., 2018, Molybdenum isotope behaviour in groundwaters and terrestrial hydrothermal systems, Iceland: Earth and Planetary Science Letters, v. 486, p. 108–118.

Ohmoto, H., and Lasaga, A.C., 1982, Kinetics of reactions between aqueous sulfates and sulfides in hydrothermal systems: Geochimica et Cosmochimica Acta, v. 46, p. 1727–1745.

Pokrovski, G.S., Borisova, A.Yu., and Harrichoury, J.-C., 2008, The effect of sulfur on vapor–liquid fractionation of metals in hydrothermal systems: Earth and Planetary Science Letters, v. 266, p. 345–362.

Poulson Brucker, R.L., McManus, J., Severmann, S., and Berelson, W.M., 2009, Molybdenum behavior during early diagenesis: Insights from Mo isotopes: Geochem. Geophys. Geosyst., v. 10, p. Q06010.

Preece, R.K., 1979, Paragenesis, geochemistry, and temperature of formation of alteration assemblages at the Sierrita Deposit, Pima County, Arizona [M.S. Thesis]: University of Arizona, 106 p.

Preece, R.K., and Beane, R.E., 1982, Contrasting evolutions of hydrothermal alteration in quartz monzonite and quartz diorite wall rocks at the Sierrita porphyry copper deposit, Arizona: Economic Geology, v. 77, p. 1621–1641.

Raith, J.G., and Stein, H.J., 2000, Re–Os dating and sulfur isotope composition of molybdenite from tungsten deposits in western Namaqualand, South Africa: implications for ore genesis and the timing of metamorphism: Mineralium Deposita, v. 35, p. 741–753.

Reed, M.H., 1997, Hydrothermal alteration and its relationship to ore fluid composition: Geochemistry of hydrothermal ore deposits, v. 3, p. 303–365.

Rouxel, O., Shanks III, W.C., Bach, W., and Edwards, K.J., 2008, Integrated Fe- and S-isotope study of seafloor hydrothermal vents at East Pacific Rise 9–10°N: Chemical Geology, v. 252, p. 214–227.

Sakai, H., 1968, Isotopic properties of sulfur compounds in hydrothermal processes: Geochemical Journal, v. 2, p. 29–49.

Seo, J.H., Guillong, M., and Heinrich, C.A., 2009, The role of sulfur in the formation of magmatic–hydrothermal copper–gold deposits: Earth and Planetary Science Letters, v. 282, p. 323–328.

Seward, T.M., Williams-Jones, A.E., and Migdisov, A.A., 2014, The Chemistry of Metal Transport and Deposition by Ore-Forming Hydrothermal Fluids, *in* Treatise on Geochemistry, Elsevier, p. 29–57.

Shafiei, B., Shamanian, G., Mathur, R., and Mirnejad, H., 2014, Mo isotope fractionation during hydrothermal evolution of porphyry Cu systems: Mineralium Deposita, v. 50, p. 281–291.

Siebert, C., Nagler, T.F., von Blanckenburg, F., and Kramers, J.D., 2003, Molybdenum isotope records as a potential new proxy for paleoceanography: Earth and PlanetaryScience Letters, v. 211, p. 159–171.

Sinclair, W.D., 2007, Porphyry deposits, *in* Mineral Deposits of Canada: A Synthesis of Major Deposit-Types, District Metallogeny, the Evolution of Geological Provinces, and Exploration Methods, Geological Association of Canada, Mineral Deposits Division, Special Publication, v. 5, p. 223–243.

Smedley, P.L., and Kinniburgh, D.G., 2017, Molybdenum in natural waters: A review of occurrence, distributions and controls: Applied Geochemistry, v. 84, p. 387–432.

Stavast, W.J.A., Butler, R.F., Seedorff, E., Barton, M.D., and Ferguson, C.A., 2008, Tertiary Tilting and Dismemberment of the Laramide Arc and Related Hydrothermal Systems, Sierrita Mountains, Arizona: Economic Geology, v. 103, p. 629–636.

Stein, H.J., and Hannah, J.L., 1985, Movement and origin of ore fluids in Climax-type systems: Geology, v. 13, p. 469–474.

Sun, W. et al., 2013, The link between reduced porphyry copper deposits and oxidized magmas: Geochimica et Cosmochimica Acta, v. 103, p. 263–275.

Tossell, J.A., 2005, Calculating the partitioning of the isotopes of Mo between oxidic and sulfidic species in aqueous solution: Geochimica et Cosmochimica Acta, v. 69, p. 2981–2993.

Ulrich, T., and Mavrogenes, J., 2008, An experimental study of the solubility of molybdenum in H2O and KCl–H2O solutions from 500 °C to 800 °C, and 150 to 300 MPa: Geochimica et Cosmochimica Acta, v. 72, p. 2316–2330.

Vesper, D., Roy, M., and Rhoads, C., 2008, Selenium distribution and mode of occurrence in the Kanawha Formation, southern West Virginia, USA: International Journal of Coal Geology, v. 73, p. 237–249.

Wang, D., 2012, Redox chemistry of molybdenum in natural waters and its involvement in biological evolution: Frontiers in Microbiology, v. 3, doi:10.3389/fmicb.2012.00427.

West, R., and Aiken, D., 1982, Geology of the Sierrita-Esperanza deposit, Pima mining district, Pima county, Arizona, *in* Titley, S.R. ed., Advances in Geology of the Porphyry Copper Deposits, Southwestern North America, p. 433–465.

Westra, G., and Keith, S.B., 1981, Classification and Genesis of Stockwork Molybdenum Deposit: Economic Geology, v. 76, p. 844–873.

Williams-Jones, A.E., and Heinrich, C.A., 2005, 100th Anniversary Special Paper: Vapor Transport of Metals and the Formation of Magmatic-Hydrothermal Ore Deposits: Economic Geology, v. 100, p. 1287–1312.

Xu, D.R., Wu, C.J., Hu, G.C., Chen, M.L., Fu, Y.R., Wang, Z.L., Chen, H.Y., and Hollings, P., 2016, Late Mesozoic molybdenum mineralization on Hainan Island, South China: Geochemistry, geochronology and geodynamic setting: Ore Geology Reviews, v. 72, Part 1, p. 402–433.

Yao, J., Mathur, R., Sun, W., Song, W., Chen, H., Mutti, L., Xiang, X., and Luo, X., 2016, Fractionation of Cu and Mo isotopes caused by vapor-liquid partitioning, evidence from the Dahutang W-Cu-Mo ore field: Geochemistry, Geophysics, Geosystems, v. 17, p. 1725–1739.

Zajacz, Z., Candela, P.A., and Piccoli, P.M., 2017, The partitioning of Cu, Au and Mo between liquid and vapor at magmatic temperatures and its implications for the genesis of magmatic-hydrothermal ore deposits: Geochimica et Cosmochimica Acta, v. 207, p. 81–101, doi:10.1016/j.gca.2017.03.015.

Zajacz, Z., Candela, P.A., Piccoli, P.M., Sanchez-Valle, C., and Wälle, M., 2013, Solubility and partitioning behavior of Au, Cu, Ag and reduced S in magmas: Geochimica et Cosmochimica Acta, v. 112, p. 288–304.

Zhang, L., Audétat, A., and Dolejš, D., 2012, Solubility of molybdenite (MoS2) in aqueous fluids at 600–800 °C, 200 MPa: A synthetic fluid inclusion study: Geochimica et Cosmochimica Acta, v. 77, p. 175–185.

Appendix A. Examples of Molybdenum-Sulfur Isotope Systematics

Below follows a derivation demonstrating that for Rayleigh fractionation with any chosen fractionation (ε) 63% of the data fall between the initial isotope composition of Mo and the isotope composition of initial Mo+ε.

Equation for Rayleigh isotope fractionation:

$$\delta^{98}\mathrm{Mo}_{\mathrm{residual}}\left(f(t)\right)=\delta^{98}\mathrm{Mo}_{\mathrm{initial}}+\varepsilon\cdot\ln\left(f(t)\right)$$

with:

$\delta^{98}\mathrm{Mo}_{\mathrm{residual}}\left(f(t)\right)$: Mo isotope composition of residual Mo at time t

$f(t)$: fraction of residual Mo at time t

ε: isotope enrichement factor

Question: at what $f(t_x)$ does $\delta^{98}\mathrm{Mo}_{\mathrm{MoS_2}}\left(f(t_x)\right)$ become equal to $\delta^{98}\mathrm{Mo}_{\mathrm{initial}}$?

$$\delta^{98}\mathrm{Mo}_{\mathrm{MoS_2}}\left(f(t)\right)=\delta^{98}\mathrm{Mo}_{\mathrm{residual}}\left(f(t)\right)+\varepsilon$$

$$\Rightarrow\delta^{98}\mathrm{Mo}_{\mathrm{initial}}=\delta^{98}\mathrm{Mo}_{\mathrm{MoS_2}}\left(f(t_x)\right)=\delta^{98}\mathrm{Mo}_{\mathrm{residual}}\left(f(t_x)\right)+\varepsilon=\delta^{98}\mathrm{Mo}_{\mathrm{initial}}+\varepsilon\cdot\ln\left(f(t_x)\right)+\varepsilon$$

$$\Rightarrow\delta^{98}\mathrm{Mo}_{\mathrm{initial}}=\delta^{98}\mathrm{Mo}_{\mathrm{initial}}+\varepsilon\cdot\ln\left(f(t_x)\right)+\varepsilon$$

$$\Rightarrow-\varepsilon=\varepsilon\cdot\ln\left(f(t_x)\right)$$

$$\Rightarrow f(t_x)=e^{-1}\approx0.368\approx37\%$$

Sulfur isotope scenarios

Here we present a suite of scenarios for the deposition of MoS_2 that result in distinct Mo-S isotope relationships. For the Mo isotope fractionation associated with these scenarios we always employed the Rayleigh fractionation presented in Fig. 3. For model calculations, a temperature drop from 430 °C to 360 °C was simulated using S isotope fractionations based on Sakai (1968) and Ohmoto and Rye (1979).

The first scenario is the case where there is a very large pool of SO_2, and relatively small pools of sulfate and sulfide, and S isotope equilibration is very rapid. In such a case, the isotope signatures of the various S phases will depend on the S isotope composition of SO_2 (for simplicity assumed to be 0‰) and on the temperature-dependent isotope fractionations (Fig. A1). As temperature drops, the isotope offset between sulfide and sulfate becomes larger. Since sulfide concentrations are kept low (effective titration to form MoS_2) the oxidized S pool will always dominate, i.e. barely change its isotope composition.

Result of scenario 1: As the Mo isotope composition of MoS_2 becomes heavy, the S isotope composition becomes light. This relationship would appear to be non-linear, as Mo increases in an exponential Rayleigh fractionation pattern, whereas the S isotope trend to lighter values is quasi-linear (Fig. 4). The isotope composition of coexisting sulfate (e.g. as anhydrite) would increase.

The second scenario is a case with an overall small pool of sulfur dioxide which is disproportionated into sulfide and sulfate, while rapid S isotope equilibrium exchange takes place (Fig. A2a).

In the second scenario, the overall oxidized S pool becomes isotopically heavier as isotopically light MoS_2 is removed (Fig. 6B, $SO_2 + SO_4^{2-}$). However, because of the rapid isotope exchange between sulfate and sulfur dioxide, and the growing sulfate pool (Fig. A2), all individual S species become isotopically lighter (Fig. A2b).

Result of scenario 2: As the Mo isotope composition of MoS_2 becomes heavy, the corresponding S isotope composition becomes rapidly light (Fig. 4). The isotope composition of coexisting sulfate (e.g. as anhydrite) decreases.

The third scenario considers reduction of SO_2 from a small overall SO_2 pool to sulfide instead of SO_2 disproportionation, with immediate quantitative sequestration of the formed sulfide into MoS_2. For the S isotope fractionation during sulfate reduction, we use the temperature dependent equilibrium isotope fractionation between bisulfide (HS^-) and SO_2. The removal of isotopically light sulfide leads to an enrichment in ^{34}S in the residual SO_2, which is also captured as a trend to heavier $\delta^{34}S$ of MoS_2, analogous to a Rayleigh distillation-type isotope fractionation (Fig. A3).

Result of scenario 3: Both Mo and S isotope composition of MoS_2 become heavy, displaying Rayleigh distillation isotope fractionation trends (Fig. 4).

In the fourth scenario, we consider an initial formation of a bisulfide (HS^-) pool that is not further replenished, for example as the result of quantitative reduction of sulfate and SO_2 to sulfide, or phase separation from residual SO_2 due to boiling at a transition to lower pressure. We model

to evolution of the isotope composition of MoS_2 and HS^- during the sequestration of the sulfide into the mineral as temperature drops (Fig. A4).

Result of scenario 4: As the Mo isotope composition of MoS_2 becomes heavy the S isotope composition becomes light (Fig. 4). Both isotope trends follow Rayleigh fractionation patterns.

This suite of scenarios is by no means complete, and the actual conditions in ore deposits, such as the size and speciation of the S inventory and temperature range in which MoS_2 forms may differ from the parameters chosen to calculate the Mo-S isotope relationships. Nevertheless, it clearly demonstrates the enormous potential of using these coupled isotope systems to gain unprecedented insight into the formation of this mineral, and by extension, on the genesis of porphyry Cu-Mo deposits in general (Fig. 4). Finally, it is possible that we might observe non-systematic relationships between variations in the Mo and S isotope composition of MoS_2. Such patterns could indicate that there are several pulses of Mo-bearing fluids with different starting Mo signatures, which react with sulfide at the site of MoS_2 precipitation.

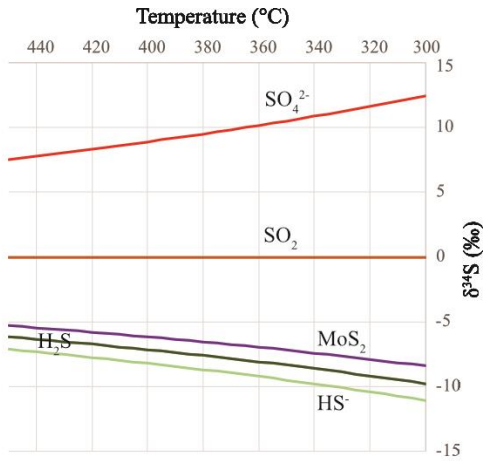

Figure A1. Equilibrium S isotope fractionation with a very large pool of SO_2 ($\delta^{34}S_{SO2}$ = 0‰) as a function of temperature. Calculations based on Sakai (1968) and Ohmoto and Rye (1979).

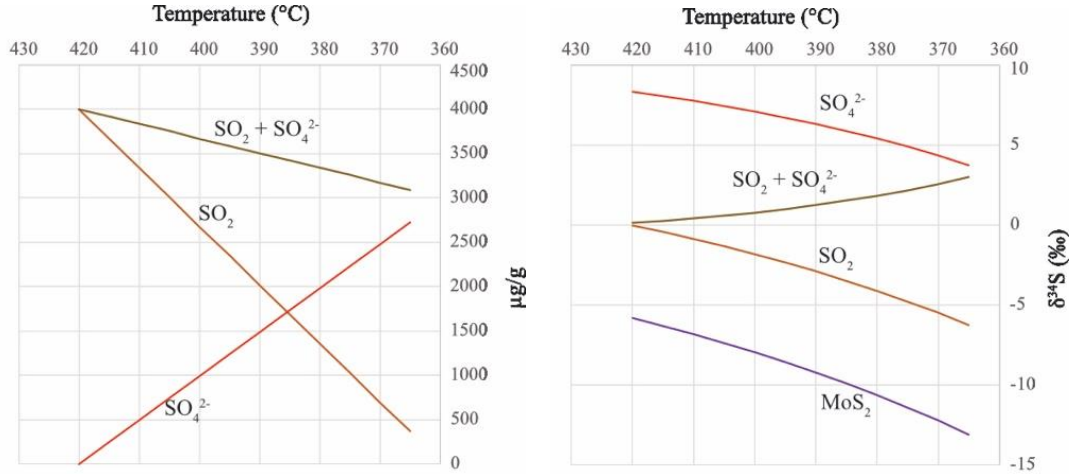

Figure A2a, A2b. Equilibrium S isotope fractionation with a small pool of SO_2 ($\delta^{34}S_{SO2}$ = 0‰) as a function of temperature, model calculations based on S mass balances for SO_2 disproportionation and temperature dependent S isotope fractionations (Sakai, 1968; Ohmoto & Rye, 1979).

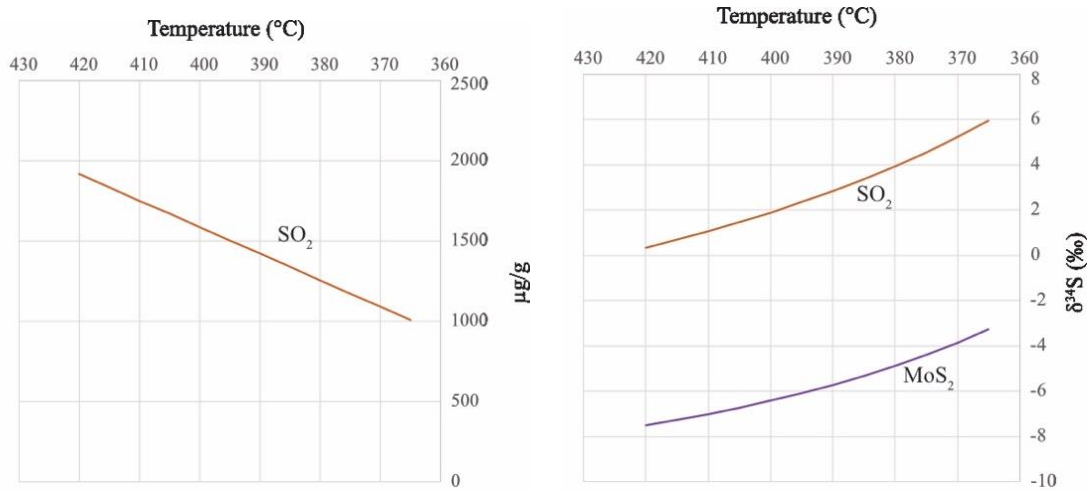

Figure A3a, A3b. Reduction of a small pool of SO_2 ($\delta^{34}S_{SO2}$ = 0‰) to sulfide, followed by immediate quantitative sequestration of sulfide as MoS_2.

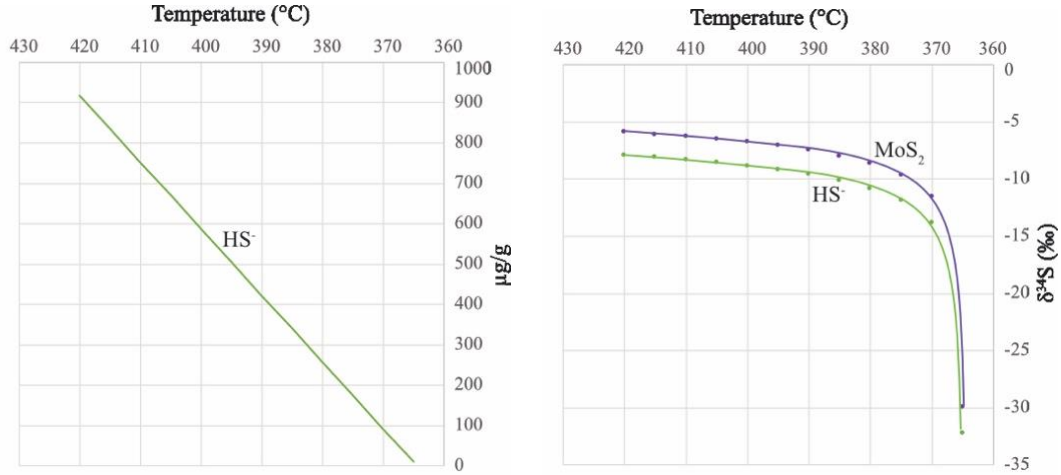

Figure A4a, A4b. Transformation of a small pool of sulfide (initial $\delta^{34}S_{HS-}$ = -7‰) into MoS_2.

Appendix B. Sample Catalog

Sample	Box	Depth (ft)	MoS_2 present?	FeS_2 present?
D2414 – 1	59	515	Vein hosted	Finely disseminated in veins
D2414 – 2	59	520	Vein hosted	Disseminated in veins
D2414 – 3	59	522	Vein hosted	Disseminated in rock and veins
D2414 - 4	60	525	Vein hosted	Not visible
D2414 - 5	60	527	Vein hosted	Disseminated in vein
D2414 - 6	60	528	Vein hosted	Disseminated in vein
D2414 – 7	60	530.5	Vein hosted, Paint	Disseminated in vein
D2414 – 8	60	531.5	Vein hosted	Isolated enclaves along vein
D2414 – 9	61	535	Disseminated along vein	Disseminated along vein
D2414 – 10	61	538.5	Vein hosted, Paint	Disseminated in rock and veins
D2414 – 11	61	539.5	Disseminated along vein	Finely disseminated in vein
D2414 – 12	61	540.5	Disseminated in veins	Not visible
D2414 – 13	61	543.5	Isolated along vein	Isolated along vein
D2414 – 14	62	544	Disseminated in veins	Disseminated in rock and veins
D2414 – 15	62	547	Disseminated in vein	Disseminated in rock and vein
D2414 – 16	62	548	Vein hosted	Not visible
D2414 – 17	62	550	Vein hosted	Disseminated in rock
D2414 – 18	62	552	Disseminated in rock and vein	Disseminated in rock
D2414 – 19	63	558	Disseminated along vein	Disseminated along vein
D2414 – 20	63	561	Disseminated in rock and vein	Disseminated in rock and vein
D2414 – 21	64	562	Vein hosted	Not visible
D2414 – 22	64	564.5	Disseminated along vein	Not visible
D2414 – 23	64	567	Disseminated in vein	Not visible
D2414 – 24	64	570	Vein hosted, Paint	Not visible
D2414 – 25	65	575	Vein hosted, Paint	Not visible
D2414 – 26	65	578	Vein hosted	Disseminated in rock

Sample	Box	Depth (ft)	MoS_2 present?	FeS_2 present?
D2414 – 27	65	579	Vein hosted	Disseminated in rock
D2406 – 28	247	2114.5	Vein hosted	Disseminated in rock
D2406 – 29	247	2118	Isolated in matrix	Disseminated in rock and matrix
D2406 – 30	247	2121.5	Matrix and vein hosted	Disseminated in rock and matrix
D2406 – 31	248	2124.5	Disseminated in vein	Disseminated and vugg hosted
D2406 – 32	248	2127	Disseminated in vein	Large grains, disseminated in rock
D2406 – 33	248	2132	Disseminated in clasts and matrix	Disseminated in calsts and matrix
D2406 – 34	248	2132.5	Matrix hosted, Paint, disseminated in clasts	Disseminated in clasts, and martix
D2406 – 35	249B	2134.5	Matrix hosted	Disseminated in matrix
D2406 – 36	249B	2138	Matrix hosted	Disseminated in matrix, finely disseminated in clasts
D2406 – 37	249B	2144.5	Matrix hosted	Disseminated in matrix
D2406 – 38	249B	2148.5	Matrix hosted, Paint	Disseminated in marix
D2406 – 39	249B	2149.5	Matrix hosted	Matrix hosted
D2406 – 40	249B	2151	Matrix hosted	Matrix hosted
D2406 – 41	249	2154.5	Matrix hosted	Martix hosted
D2406 – 42	250	2157	Matrix hosted	Matrix hosted
D2406- 43	250	2166.5	Matrix hosted	Matrix hosted
D2406 – 44	251	2166.5	Matrix hosted	Matrix hosted
D2406 – 45	251	2169	Matrix hosted, Paint	Matrix hosted
D2406 – 46	251	2171.5	Matrix hosted, Paint	Matrix hosted
D2406 – 47	251	2173	Matrix hosted, Paint	Disseminated in matrix
D2406 – 46	251	2171.5	Matrix hosted, Paint	Disseminated in matrix
D2406 – 47	251	2173	Matrix hosted	Matrix hosted
D2406 – 48	252	2175.5	Disseminated in Matrix	Matrix hosted
D2406 – 49	252	2178	Matrix hosted, Paint	Disseminated in matrix
D2406 – 50	252	2180	Matrix hosted, Paint	Disseminated in matrix
D2406 – 51	252	2180.5	Matrix hosted, Paint	Matrix hosted

Sample	Box	Depth (ft)	MoS_2 present?	FeS_2 present?
D1878B–52	95	1556.5	Vein Hosted	Not visible
D1878B-53	96bkw	1565	Disseminated in veins	Disseminated in veins
D1878B-54	96bkw	1567	Disseminated in vein	Disseminated in vein
D1878B-55	96bkw	1576	Disseminated in veins	Not visible
D1878B-56	96bkw	1578	Vein hosted	Not visible
D2314 – 57	150	1346	Matrix hosted	Disseminated matrix and clasts
D2314 – 58	150	1348	Matrix hosted	Matrix hosted and disseminated in clasts
D2314 – 59	150	1350	Matrix hosted	Matrix hosted and disseminated clasts
D2314 – 60	150	1350	Matrix hosted	Matrix hosted
D2314 – 61	150	1352	Matrix hosted	Disseminated matrix
D2314 – 62	153	1375	Disseminated veins	Disseminated
D2314 – 63	153	1377	Vein hosted	Disseminated matrix and clasts
D2314 – 64	153	1377.5	Matrix hosted, Paint	Disseminated matrix and clasts
D2314 – 65	153	1379	Matrix hosted, Paint	Disseminated matrix
D2199 – 66	102	910	Vein hosted, Paint	Disseminated vein and rock
D2199 – 67	102	914	Disseminated	Disseminated
D2199 – 68	102	915	Vein hosted and disseminated in rock	Disseminated in rock
D2199 – 69	102	916.5	Vein hosted	Not visible
D2199 – 70	102	918	Vein hosted, Paint	Disseminated in vein
D2199 – 71	102	918	Vein hosted, Paint	Disseminated in vein
D2199 – 72	103	919	Vein hosted, Paint	Disseminated in vein and rock
D2199 – 73	103	919.5	Vein hosted	Disseminated vein
D2199 – 74	103	921	Disseminated	Disseminated
D2199 – 75	103	922	Vein hosted, Paint	Not visible
D2199 – 76	103	924	Disseminated	Disseminated in rock
D2199 – 77	103	925	Disseminated in veins	Disseminated in rock
D2199 – 78	103	926.5	Disseminated in veins	w/ vuggy quartz

Box Number	Sample D2414 - 1
59	Altered Qtz monzonite, broken along veinlet face. Mineralization dominated by quartz, molybdenite, and sericite. Very few pyrite.
Sample Depth (ft)	
515	

Box Number	Sample D2414 - 2
59	Altered Qtz monzonite, gray green, plagioclase altered to white and grey-green clays. Broken along veinlet face. Vein mineralization shows quartz, molybdenite, sericite, pyrites, and clays.
Sample Depth (ft)	
520	

Box Number	Sample D2414 - 3
59	Less altered quartz monzonite cross cut by veinlets, some plagioclase altered to chlorite near veins. Some disseminated pyrites near veins. Veins filled with quartz, molybdenite and sericite, some pyrites.
Sample Depth (ft)	
522	

Box Number	Sample D2414 - 4
60	Altered and slightly altered quartz monzonite clasts cut by quartz and molybdenite vein with clays. No slicken textures, or visible pyrites.
Sample Depth (ft)	
525	

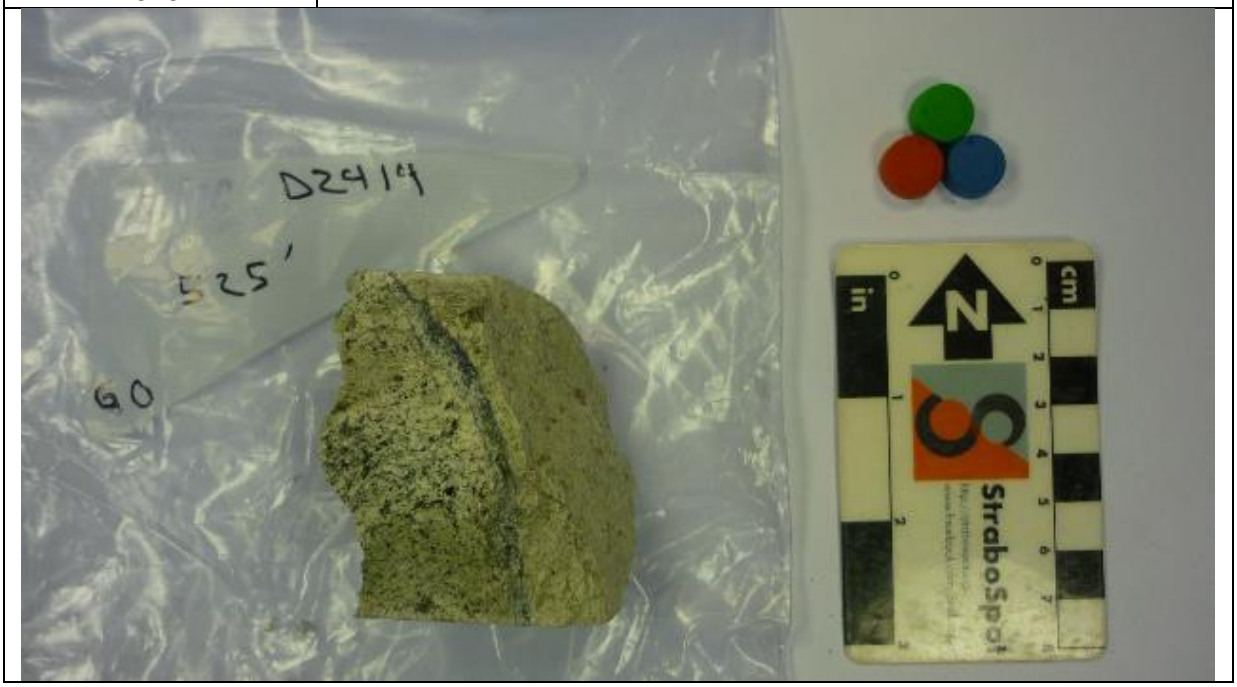

Box Number	Sample Number - 5
60	Altered quartz monzonite, plagioclase altered to yellowish white clays, disseminated pyrites, quarts persisting. Two fracture surfaces show quartz sericite and molybdenite with dispersed pyrites.
Sample Depth (ft)	
527	

Box Number	Sample D2414 - 6
60	Altered quartz monzonite, plagioclase altered to clays, quartz and micas persisting. Molybdenite hosing veins not well defined in sample but associated with quartz and sericite, and some disseminated pyrites.
Sample Depth (ft)	
528	

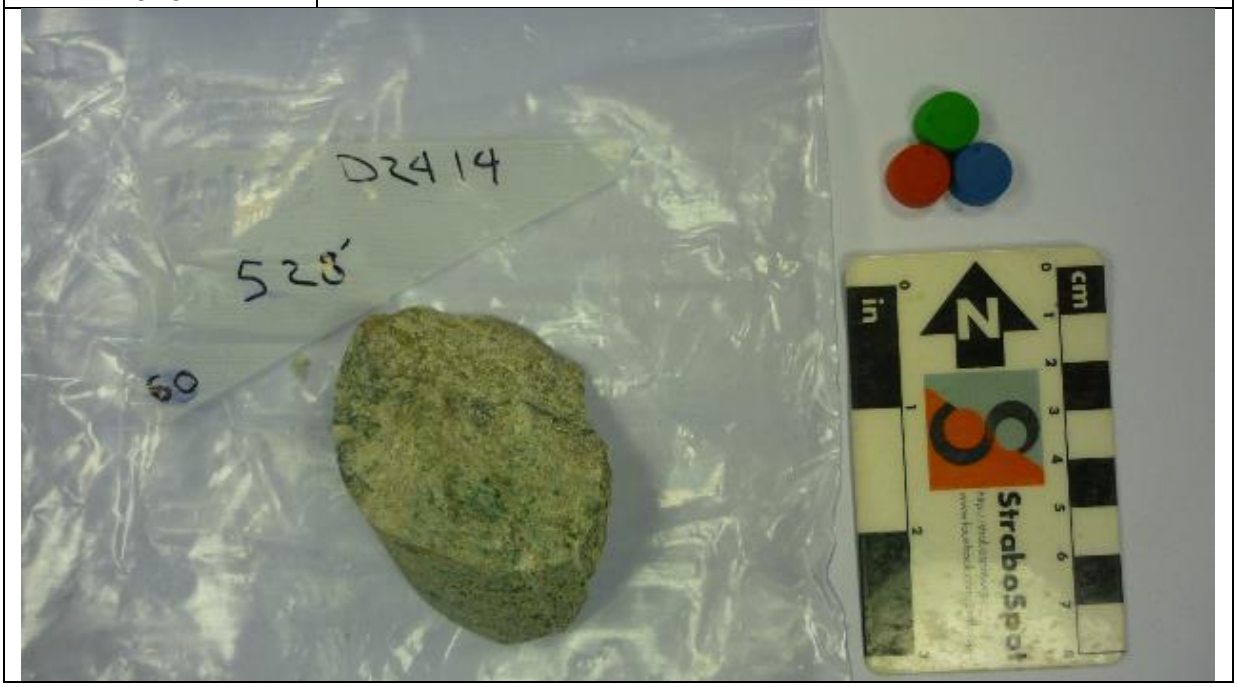

Box Number	Sample D2414 - 7
60	Fractured quartz monzonite, some alteration to grey green clays. Prominent fracture surface showing quartz and molybdenite and slicken textures with some pyrites
Sample Depth (ft)	
530.5	

Box Number	Sample D2414 - 8
60	Altered quartz monzonite, feldspars to soft white clays, biotite and quartz persisting. Mineralization along fractures as veins of quartz molybdenite and sericite. Some enclaves of pyrite visible.
Sample Depth (ft)	
531.5	

Box Number	Sample D2414 - 9
61	Slightly altered quartz monzonite, very little molybdenite, quartz and pyrite show along fracture surfaces.
Sample Depth (ft)	
335	

Box Number	Sample D2414 - 10
61	Quartz rich matrix hosting disseminated pyrites in nucleation clusters. Mo shows on one corner of sample as paint with fine grained soft white mineral/s (gypsum, anhydrite, clays)
Sample Depth (ft)	
538.5	

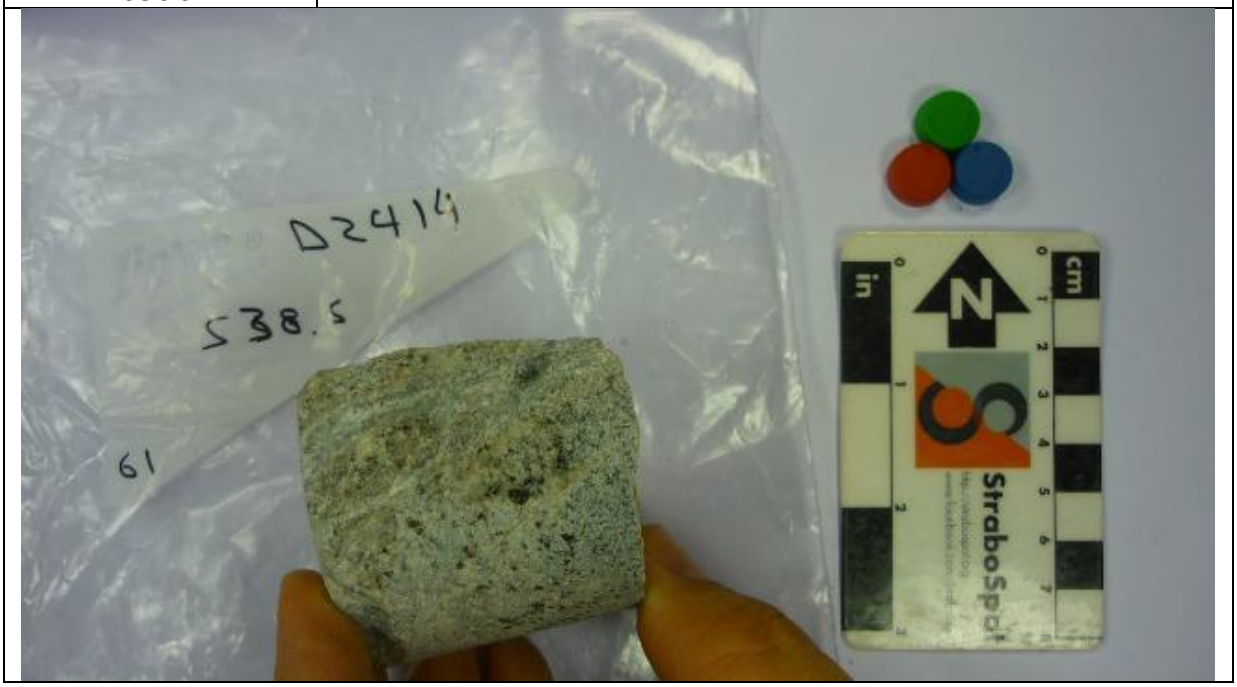

Box Number	Sample D2414 - 11
61	Altered quartz Monzonite showing numerous fractures, filled with quartz and molybdenite. Pyrite and fine-grained gypsum or sericite visible.
Sample Depth (ft)	
539.5	

Box Number	Sample D2414 - 12
61	Altered quartz Monzonite, crumbles easily. Persistent quartz rich veins show traces of molybdenite.
Sample Depth (ft)	
540.5	

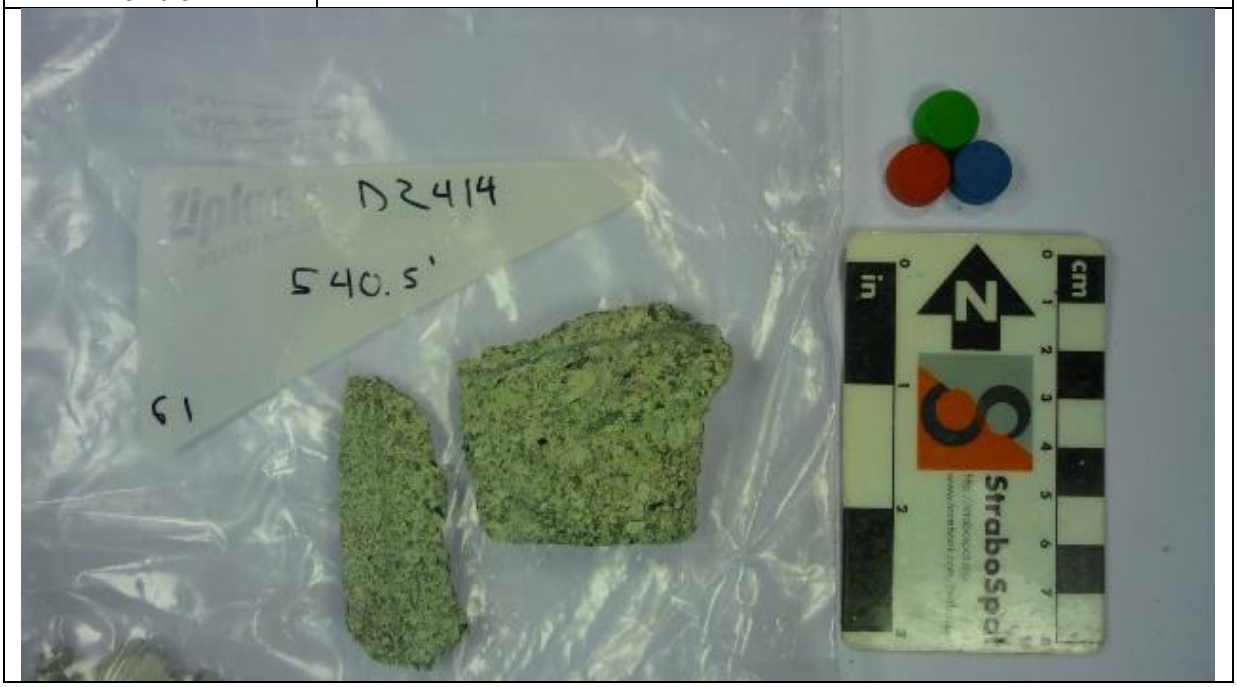

Box Number	Sample D2414 - 13
61	Altered and silicified body. Enclaves of pyrite, chalcopyrite and molybdenite along fractures.
Sample Depth (ft)	
543.5	

Box Number	Sample D2414 - 14
62	Altered Qtz Monz, hornblende + Altered feldspars + Qtz, some pyrite. Cross-cut by mineralized vein, Mos_2 + Qtz
Sample Depth (ft)	
544	

Box Number	Sample D2414 - 15
62	Altered Qtz Monz, hornblende + Altered feldspars + Qtz, some pyrite along vein halo. Cross-cut by mineralized vein, MoS_2 + Qtz
Sample Depth (ft)	
547	

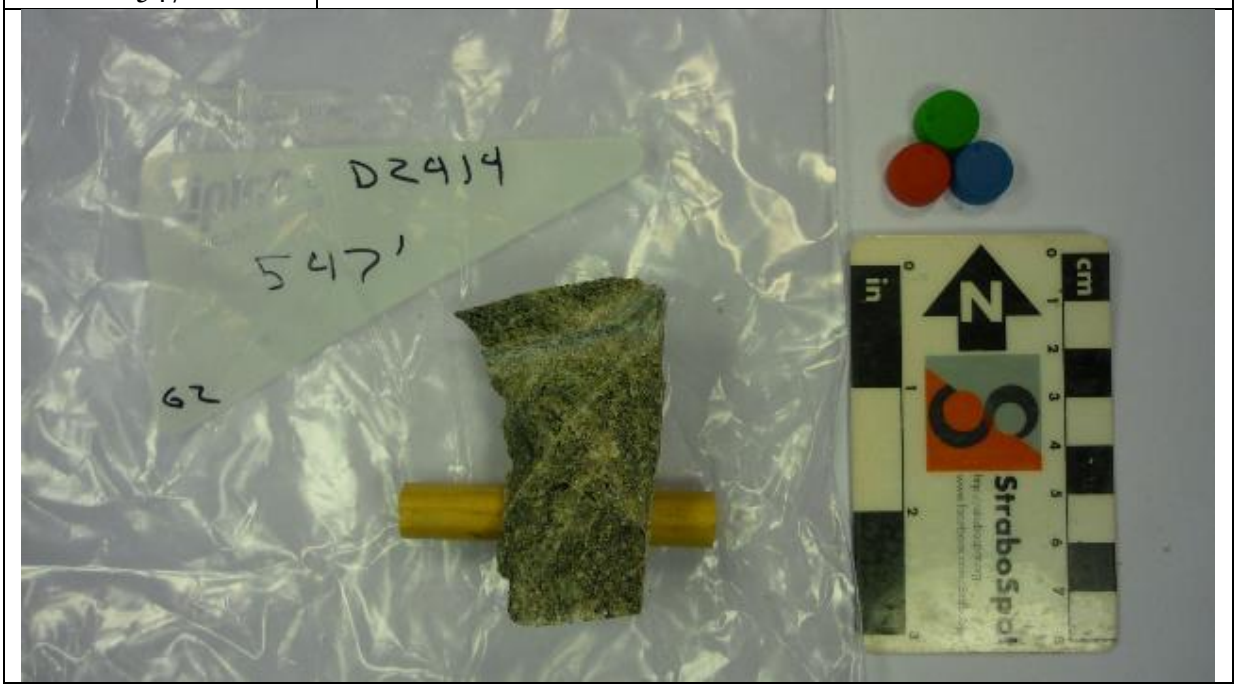

Box Number	Sample D2414 - 16
62	sample is mostly Qtz + MoS2 vein, hosted in altered Qtz Monz
Sample Depth (ft)	
548	

Box Number	Sample D2414 - 17
62	Altered Qtz Monz hosting linear pyrite features cut by Qtz + MoS_2 vein
Sample Depth (ft)	
550	

Box Number	Sample D2414 - 18
62	Altered Qtz Monz hosting disseminated pyrite + Chalco + MoS_2 fracture surface shows MoS_2 + Qtz + sericite
Sample Depth (ft)	
552	

Box Number	Sample D2414 - 19
63	Altered Qtz Monz, feldspars altered to greenish clays, fracture surfaces show Qtz + MoS_2 + some pyrite. Clays and sericite on all surfaces
Sample Depth (ft)	
558	

Box Number	Sample D2414 - 20
63	Altered Qtz Monz, feldspars (altered to Chlorite + Clays) + biotite + hornblende, disseminated pyrites. MoS_2 in vein with Anhy + Qtz and some Chalco
Sample Depth (ft)	
561	

Box Number	Sample D2414 - 21
64	Altered Qtz Monz, Qtz rich vein halo cut by later MoS2 rich vein with Anhy + sericite
Sample Depth (ft)	
562	

Box Number	Sample D2414 - 22
64	Altered Qtz Monz, silicification halo around veins, clay alteration outside of halo.
Sample Depth (ft)	
564.5	

Box Number	Sample D2414 - 23
64	Altered Qtz Monz - Qtz + chlorite + clays. MoS_2 in Qtz rich veins surrounding silicified fault gauge.
Sample Depth (ft)	
567	

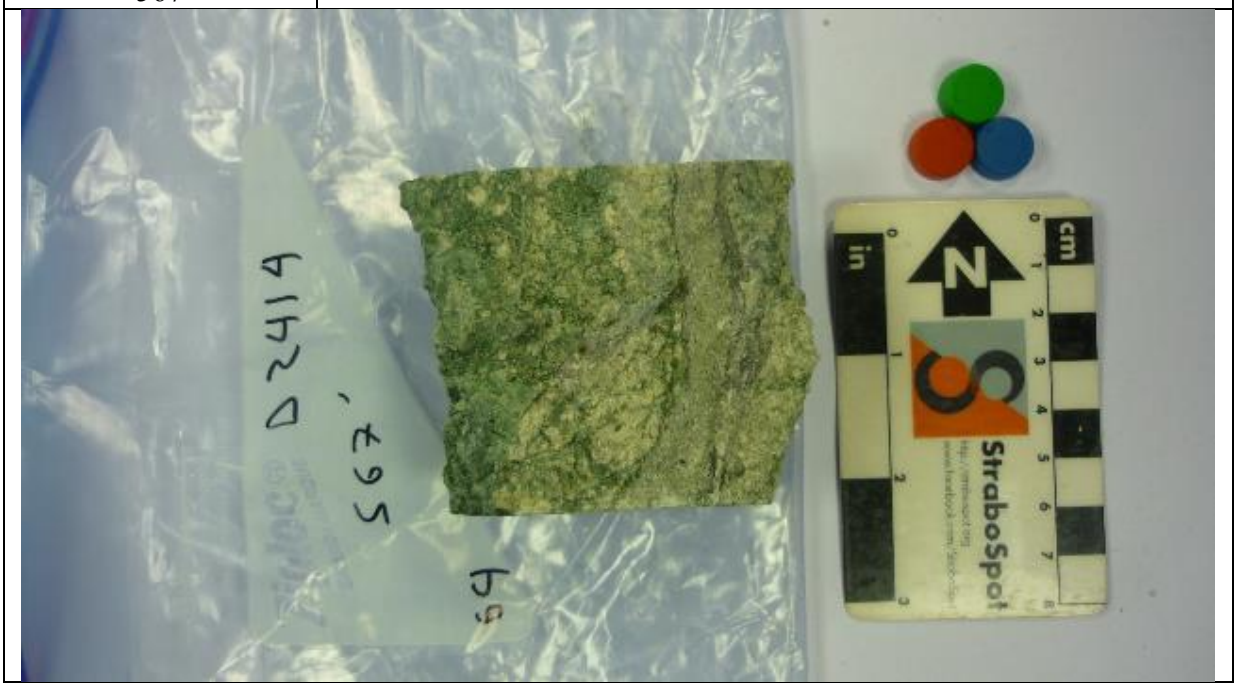

Box Number	Sample D2414 – 24
64	Chip of alteration surface, Clays and chlorite. MoS_2 paint along fracture surface
Sample Depth (ft)	
570	

Box Number	**Sample D2414 – 25**
65	Vein Chip, MoS_2 paint on clays + Fault gauge. Paint parallels fabric evident in matrix/host rock
Sample Depth (ft)	
575	

Box Number	**Sample D2414 – 26**
65	Altered Qtz Monz, feldspars altered to clays, biotite and Qtz persist. Hosts disseminated Chaco. MoS_2 in veins with Qtz + Anhy
Sample Depth (ft)	
578	

Box Number	**Sample D2414 - 27**
65	Altered Qtz Monz, clay rich, hosting disseminated Chalco. MoS_2 In Qtz rich veins
Sample Depth (ft)	
579	

Box Number	**Sample 2406 - 28**
247	Quartz rich matrix hosting disseminated pyrites in nucleation clusters. Mo shows on one corner of sample as paint with fine grained soft white mineral/s (gypsum, anhydrite, clays)
Sample Depth (ft)	
2114.5	

Box Number	Sample 2406 – 29
247	Quartz rich matrix some disseminated pyrites. Sample cross-cut by quartz rich veinlets, voids hosting pyrites and MoS_2. Matrix shows conchoidal fractures supporting silicification in alteration.
Sample Depth (ft)	
2118	

Box Number	Sample 2406 – 30
247	Quartz rich matrix, possible altered Qtz monzonite. Disseminated pyrites through-out. MoS_2 on one fracture surface with slickens and smearing.
Sample Depth (ft)	
2121.5	

Box Number	Sample 2406 - 31
248	Approximately 1/2 of intact core ~2in in length. Quartz rich matrix cross cut buy fractures some showing quartz mineralization with halos small vugs filled w/ Qtz + Py, larger hosting clear crystalline quartz.
Sample Depth (ft)	
2124.5	

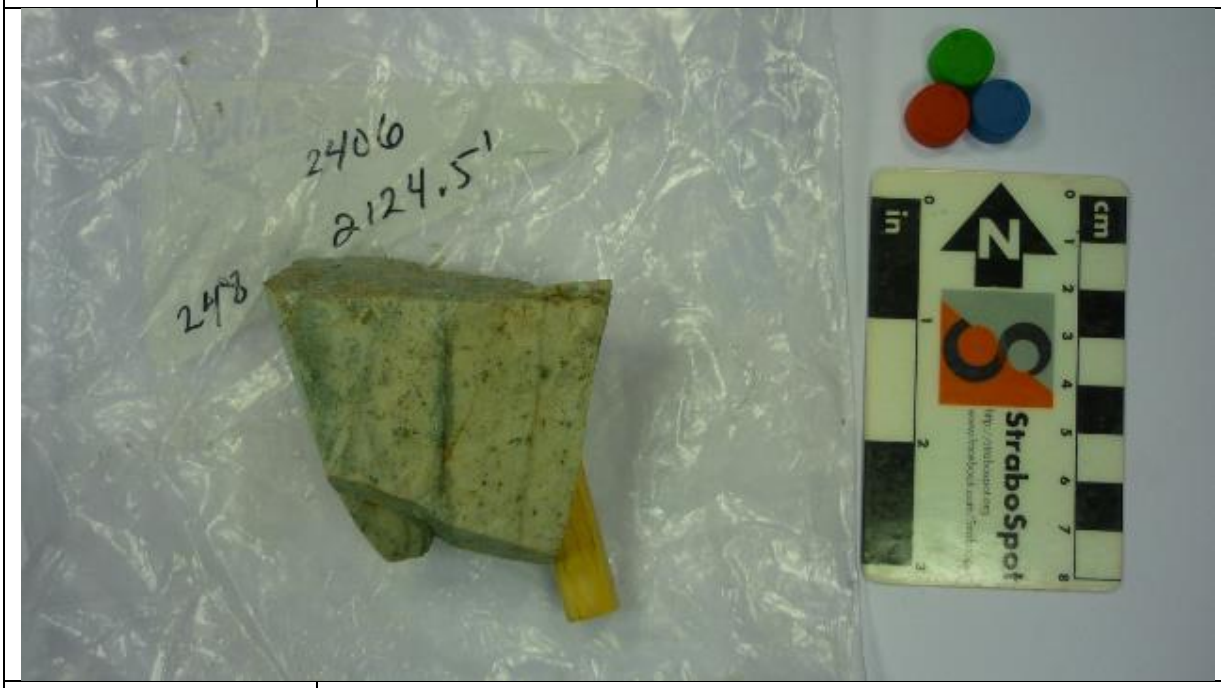

Box Number	Sample 2406 - 32
248	Quartz rich matrix -post Qtz monzonite - disseminated pyrites prominent, mm - sub-mm scale grains. MoS_2 along quartz veinlets.
Sample Depth (ft)	
2127	

Box Number	Sample 2406 - 33
248	Quartz rich matrix, cross-cut by mineralized fractures. Some (~10%) mineralization disseminated in matrix, FeS_2 + MoS_2. Most MoS_2 along veinlets. Visible mineralization, MoS_2, FeS_2, CuFeS + sericite
Sample Depth (ft)	
2132	

Box Number	Sample 2406 - 34
248	Quartz rich matrix with disseminated FeS_2, CuFeS, MoS_2. Cross-cut by mineralized fractures w/slicken textures. Mineralization of Qtz + MoS_2 + sericite + pyrite. MoS_2 mineralization along fracture surfaces and veinlets
Sample Depth (ft)	
2132.5	

Box Number	Sample 2406 - 35
248 B	Breccia, clast supported. Clasts of quartz monzonite, in filled with clays, sericite, MoS_2, and Qtz. Some visible grains of pyrite
Sample Depth (ft)	
2134.5	

Box Number	Sample 2406 - 36
249 B	Highly brecciated. Clast supported Qtz Monz in-filled with MoS_2, Qtz, sericite + pyrite Very little noticeable dissemination in clasts, MoS_2 coating surfaces with isolated grains of FeS_2
Sample Depth (ft)	
2138	

Box Number	Sample 2406 - 37
249 B	Small Brecciated Clasts (~1mm) of Qtz Monz, in-filled with noticeably more clays and sericite. MoS_2 is surfaces and as clasts in breccia. "smears" of Py, Chalco, in MoS_2
Sample Depth (ft)	
2144.5	

Box Number	Sample 2406 - 38
249 B	Breccia, small clasts of Qtz Monz, MoS_2 "paint" covering 2 prominent surfaces. $CuFeS + FeS_2$ in small isolated grains in paint surfaces Vugs show larger Qtz grains
Sample Depth (ft)	
2148.5	

Box Number	Sample 2406 - 39
249	Breccia, Qtz Monz clast supported, in-filled with MoS_2 + $CaSO_4$ + sericite. Anhydrite is in large grains and lilac in color. MoS_2 surrounds Anhy and also as inclusions w/in Anhy. Py + Chalco in small grains between anhydrites
Sample Depth (ft)	
2149.5	

Box Number	Sample 2406 - 40
249	Breccia, quartz rich, angular and highly fractured. Fracture surfaces show slickens. MoS_2, Py + Anhy appear co-genetic. Also visible is gypsum, likely post mineralization with few orange calcite
Sample Depth (ft)	
2151	

Box Number	Sample 2406 - 41
249	Highly fractured Qtz Monz breccia, void space and fractures mineralized w/ MoS_2 Anhy, FeS_2 and Chalco. Secondary gypsum vein cuts MoS_2 and Anhy mineralization
Sample Depth (ft)	
2154.5	

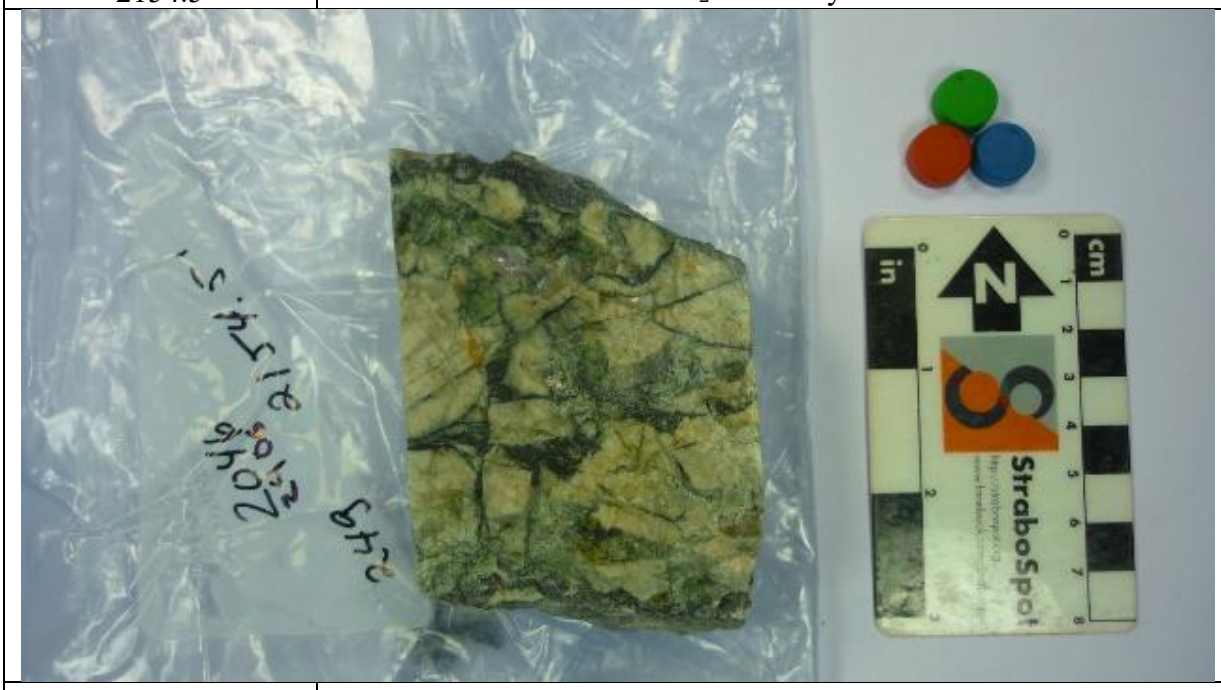

Box Number	Sample 2406 - 42
250	Quartz Monz breccia, clast supported, void space filled w/ MoS_2 Anhy, Py, and Chalco
Sample Depth (ft)	
2157	

Box Number	Sample 2406 - 43
250	Clast supported Qtz Monz breccia, increased silicification. Voids filled with MoS_2 and FeS_2, Anhy, and Chalco with sericite
Sample Depth (ft)	
2165	

Box Number	Sample 2406 - 44
251	Clast supported Qtz Monz breccia, increased silicification. Voids and fractures filled with MoS_2 +Anhy + Py + Chalco + sericite. Pyrite visible as inclusions in anhydrite. MoS_2 preferential to quartz rich surfaces, some flakes w/in anhydrite.
Sample Depth (ft)	
2166.5	

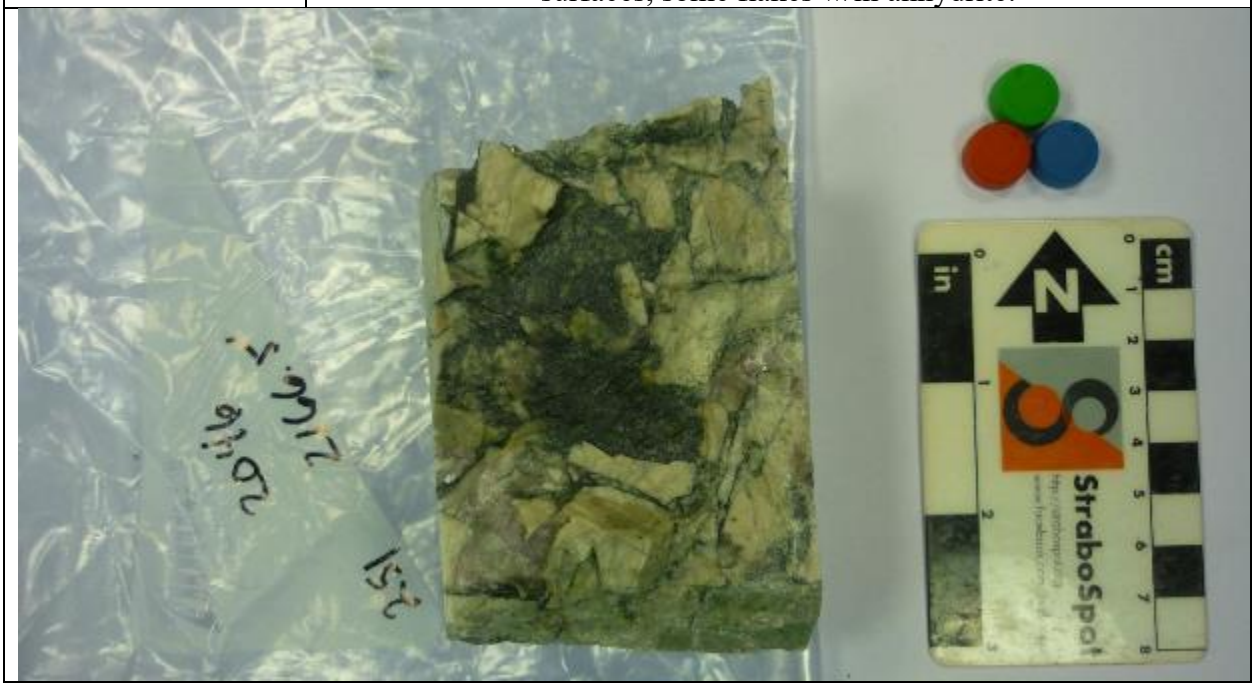

Box Number	Sample 2406 - 45
251	Clast supported Qtz Monz breccia, silicification. Clasts are highly fractured and spaces filled w/ Mo + Anhy + Chalco + Py + sericite & Gypsum. MoS_2 preferentially paints on clasts with small grains of Py + Chalco. Anhydrite fills larger voids
Sample Depth (ft)	
2169	

Box Number	Sample 2406 - 46
251	Clast supported Qtz Monz breccia. Mo + Anhy + Chalco + Py (gyp) + sericite. Gypsum is along veins/fractures that cut dominant mineralization zones. MoS_2 preferentially Paint on clasts w/ some Py and Chalco. Pyrite seen w/in anhydrites
Sample Depth (ft)	
2171.5	

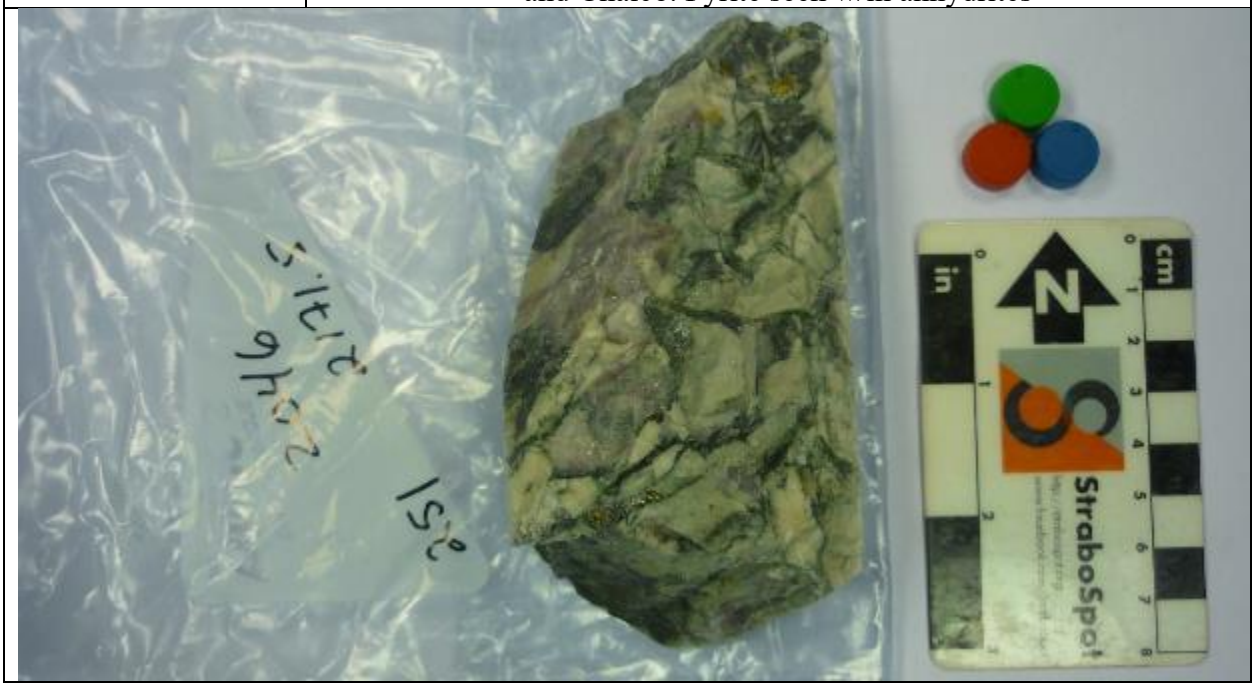

Box Number	Sample 2406 - 47
251	Clast supported Qtz Monz breccia, silicification. Fractures and voids filled w/ Mo + Anhy + Py + Chalco +sericite. Gypsum along later fractures. MoS_2 preferred paint on clasts, Anhy filling larger voids. Chalcopyrite after MoS_2 and pyrite along with anhydrite
Sample Depth (ft)	
2173	

Box Number	Sample 2406 - 46
251	Clast supported Qtz Monz breccia. Mo + Anhy + Chalco + Py (gyp) + sericite. Gypsum is along veins/fractures that cut dominant mineralization zones. MoS2 preferentially Paint on clasts w/ some Py and Chalco. Pyrite seen w/in anhydrites
Sample Depth (ft)	
2171.5	

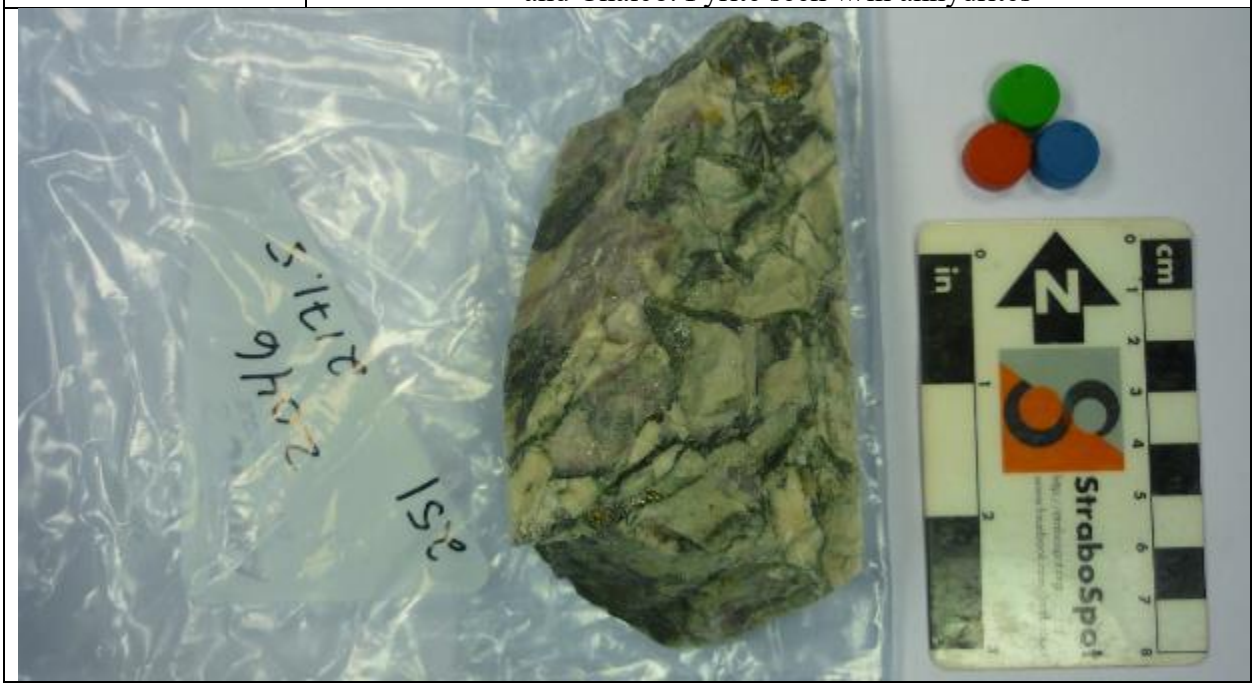

Box Number	Sample 2406 - 47
251	Clast supported Qtz Monz breccia, silicification. Fractures and voids filled w/ Mo + Anhy + Py + Chalco +sericite. Gypsum along later fractures. MoS_2 preferred paint on clasts, Anhy filling larger voids. Chalcopyrite after MoS_2 and pyrite along with anhydrite
Sample Depth (ft)	
2173	

Box Number	Sample 2406 - 48
252	Clast supported Qtz Monz breccia, Voids and Fractures mineralized w/ Mo + Py + Anhy. Mo less prominent to Pyrites. Chalco much less visible, only seen as small grains along Mo paint surfaces. Gyp only seen on cross cutting fractures
Sample Depth (ft)	
2175.5	

Box Number	Sample 2406 – 49
252	Clast supported Qtz Monz breccia. Voids and fractures filled with Mo + Py + Anhy + Chalco + Ser. Increasing Py, grains and number, filling larger voids. Mo as paint on surfaces. Anhy less prominent, paint visible in larger voids.
Sample Depth (ft)	
2178	

Box Number	Sample 2406 - 50
252	Clast supported Qtz Monz breccia, silicification zoned near fractures and voids. Fractures and voids mineralized with Mo + Anhy + Py + Chalco. Less mineralization overall, Mo prefers paint on clasts, Anhy + Py + Chalco preferring larger voids.
Sample Depth (ft)	
2180	

Box Number	Sample 2406 - 51
252	Clast Supported Qtz Monz breccia. MoS2 paint on clast Surfaces. Chalco with MoS_2. Anhy after Mo, Py after Anhy
Sample Depth (ft)	
2180.5	

Box Number	Sample 1878B - 52
95	Small granodiorite Mo as paint along fracture surface.
Sample Depth (ft)	
1556.5	

Box Number	Sample 1878B - 53
96 bkw	Granodiorite, quartz rich veinlets with dark inclusions. Sulfide mineralization/leaching parallels Qtz veins, chalcopyrite visible
Sample Depth (ft)	
1565	

Box Number	Sample 1878B - 54
96 bkw	Granodiorite, Qtz and Mo vein cross cut darker veins, and display alteration halos
Sample Depth (ft)	
1567	

Box Number	Sample 1878B - 55
98 bkw	Granodiorite, Qtz and Mo vein , cross cut by vuggy quartz vein orthoclase alteration visible along most of sample
Sample Depth (ft)	
1576	

Box Number	Sample 1878B - 56
98 bkw	Granodiorite, altered to orthoclase and clays. Mo along Qtz vein.
Sample Depth (ft)	
1578	

Box Number	Sample 2314 - 57
150	Grey-green clast supported breccia, with silicified clasts. Disseminated pyrites, fracture surfaces show MoS_2 + Qtz. Larger vugs support Chalco + Py + anhydrite
Sample Depth (ft)	
1346	

Box Number	Sample 2314 - 58
150	Breccia, silicified clasts. voids filled with MoS_2 + Py + Qtz + Chalco Clasts host disseminated Pyrite + Chalcopyrite
Sample Depth (ft)	
1348	

Box Number	Sample 2314 - 59
150	Clast supported breccia, voids filled with druzy Qtz + MoS_2 + Py + Chalco. Clasts host disseminated pyrites + Chalco. Quartz is fine-grained and appears interstitial with MoS_2. notable amounts of fine pyrites within MoS_2
Sample Depth (ft)	

Box Number	Sample 2314 - 60
150	Breccia clasts, coated with Qtz + FeS + MoS_2 + Chalco
Sample Depth (ft)	
1350	

Box Number	Sample 2314 - 61
150	Breccia clasts, coated with MoS_2 + Qtz and disseminated Chalco. Clasts appear to be silicified. In situ brecciation appears to have occurred more than once
Sample Depth (ft)	
1352	

Box Number	Sample 2314 - 62
153	Diorite, cross-cut with hornblende and hosting disseminated Chalco. thin veinlets w/MoS_2 + micas + hornblende
Sample Depth (ft)	
1375	

Box Number	Sample 2314 - 63
153	Clast supported breccia. Clasts silicified, hosting chalcopyrite. Voids filled with ~90% MoS_2, some Qtz + Py + Clays. Vug hosts larger pyrite grain with quartz
Sample Depth (ft)	
1377	

Box Number	Sample 2314 - 64
153	Breccia with larger clasts than previous, MoS_2 on surfaces + Qtz. Py + Chalco disseminated in clasts and in vugs.
Sample Depth (ft)	
1377.5	

Box Number	Sample 2314 - 65
153	Breccia, voids filled with MoS_2 + Qtz + Clays, some Py + Chalco in notable grains
Sample Depth (ft)	
1379	

Box Number	Sample 2199 - 66
102	Santa Rita stock, granodiorite altered to clays and persistent Qtz veins and grains. MoS_2 Paint and smears of Py. Mo + Py diffuse through rock
Sample Depth (ft)	
910	

Box Number	Sample 2199 - 67
102	Highly altered granodiorite, 'rotten" and crumbles easily. Clays + Qtz + mica persist disseminated Py + MoS_2
Sample Depth (ft)	
914	

Box Number	Sample 2199 - 68
102	Altered Granodiorite, Spars altered to yellow clays disseminated MoS_2 + Py. MoS_2 Paint along fracture surface.
Sample Depth (ft)	
915	

Box Number	Sample 2199 - 69
102	Altered granodiorite, feldspars to yellow clays, MoS_2 paint on fracture surfaces and quartz veining
Sample Depth (ft)	
916.5	

Box Number	Sample 2199 - 70
102	Altered Granodiorite, feldspars to yellow clays. Notably thicker MoS_2 vein with Py. Exhibits smearing and slickens along vein.
Sample Depth (ft)	
918	

Box Number	Sample 2199 - 71
102	Altered granodiorite, feldspars to yellow clays. Thicker MoS_2 + Py vein, with smearing, FeS is fine grained and fractured. Also includes 2 vein flakes, w/ Qtz and clays.
Sample Depth (ft)	
918	

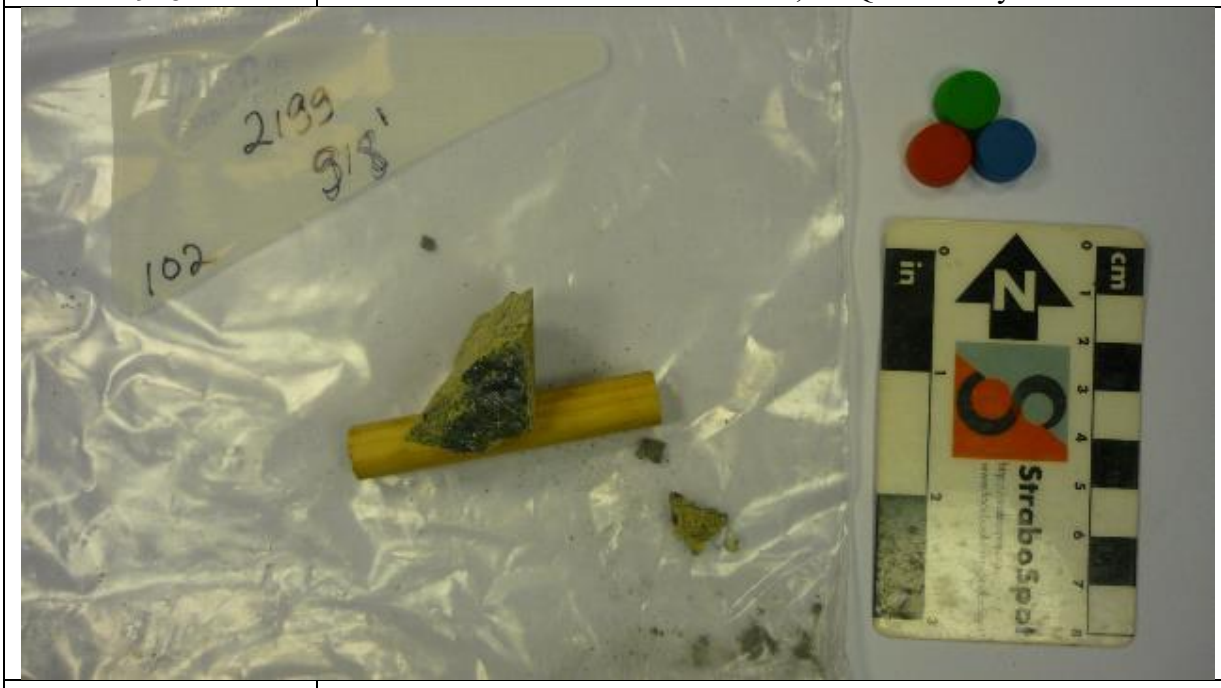

Box Number	Sample 2199 - 72
103	Altered granodiorite. MoS_2 Slicken face with nearly mirror polish, sericite noted with clays. MoS_2 + pyrrhotite in underlying vein. Apparent FeS replacing feldspars
Sample Depth (ft)	
919	

Box Number	Sample 2199 - 73
103	Altered granodiorite, MoS_2 in veins, with zoned silicification and small disseminated pyrites
Sample Depth (ft)	
919.5	

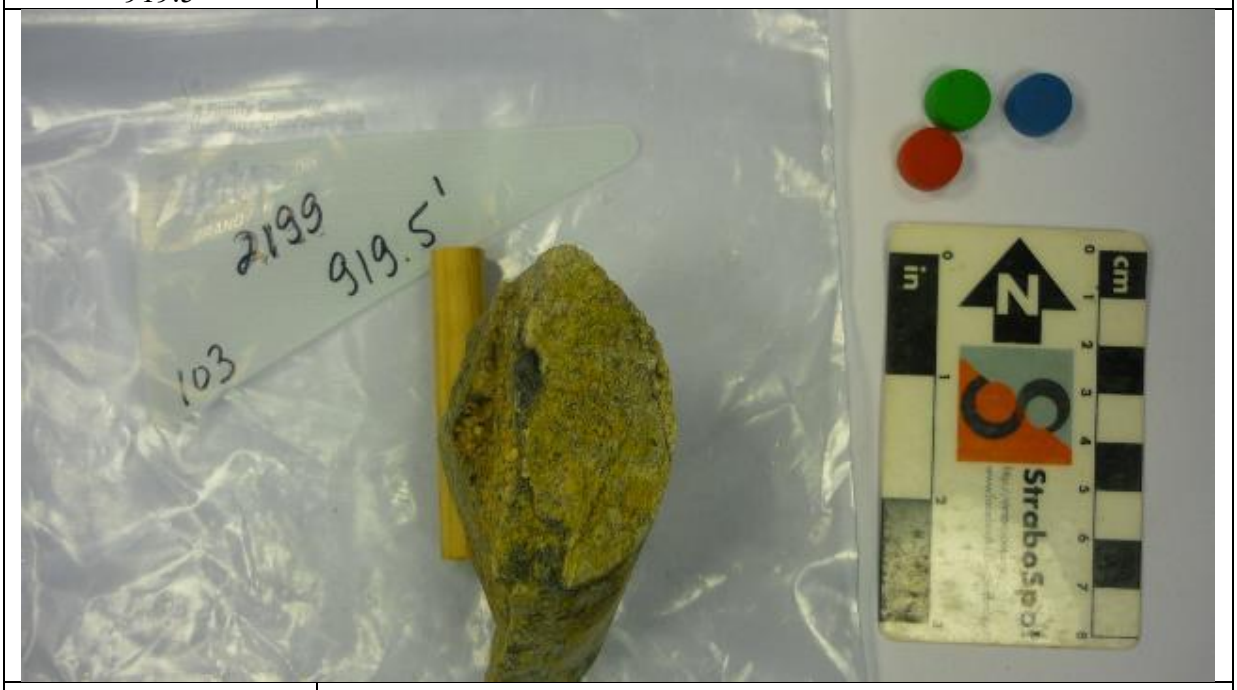

Box Number	Sample 2199 – 74
103	Altered and silicified granodiorite, smaller grains of pyrite. Very little MoS_2, sericite along fractures.
Sample Depth (ft)	
921	

Box Number	Sample 2199 - 75
103	Four small chips of altered granodiorite exhibiting MoS_2 Paint on fracture surface.
Sample Depth (ft)	
922	

Box Number	Sample 2199 - 76
103	Altered granodiorite more biotite disseminated pyrites, little MoS_2
Sample Depth (ft)	
924	

Box Number	Sample 2199 - 77
103	Altered and silicified granodiorite, MoS_2 + Qtz veins. Py disseminated in rock. Vuggy Qtz along veins
Sample Depth (ft)	
925	

Box Number	Sample 2199 - 78
103	Altered granodiorite, fractured and crosscut by Qtz Veins. Some thin veins with MoS_2. Qtz Vugs w/Py + pyrrhotite
Sample Depth (ft)	
926.5	

Vita

Joshua Roger Peterson was born in Salt Lake City, Utah. After graduating from Riverton High School, he studied for a Semester at Utah Valley State Collage, before beginning a journey through the US Army in early 2002. He graduated at the top his class as a Patriot Missile Systems Maintainer Operator training and continued his military service at Fort Bliss Texas. After four years, he transitioned into a Topographic Analyst position and program, graduating with distinction from the National Geospatial Intelligence Collage, as abasic topographic analyst, in November 2006. He served a year in Korea performing advanced analysis at Brigade and Corps levels, leading and mentoring 2-4 soldiers. Returning to Fort Bliss, he continued up to Army Level Analysis, culminating in an Honorable Discharge from duty in 2008.

He re-entered education completing his Associates in Science and Geology at El Paso Community College, receiving a STEM scholarship, which collected a multidisciplinary cohort of students to conduct research in a locally relevant topic, and was selected to join in the Border to Beltway program, a local geology exchange program between EPCC and Northern Virginia Community College. He continued on to pursue a Bachelor of Science in Geological Sciences at the University of Texas at El Paso, where he received the Alpha Gamma Epsilon scholarship for Excellence in Geology. In his final semester, he was awarded a summer research assistantship, under his current advisor that would lead into his Master's research project. During a pause between sample collection and isotope measurements he was offered a position at El Paso Water Utilities as a Geographic Information Specialist, which he took and continues to be employed in while finishing his thesis.

Josh plans to continue working at the El Paso Water Utilities and hopes to become more involved locally by teaching geology at the El Paso Community College.